Alma Mater Studiorum – Università di Bologna

DOTTORATO DI RICERCA IN

Automotive per una mobilità intelligente

Ciclo 35

Settore Concorsuale: 09/E2 - INGEGNERIA DELL'ENERGIA ELETTRICA

Settore Scientifico Disciplinare: ING-IND/32 - CONVERTITORI, MACCHINE E AZIONAMENTI ELETTRICI

HAIRPIN WINDINGS FOR HIGH RELIABILITY AND HIGH POWER DENSITY ELECTRICAL MACHINES

Presentata da: Marco Pastura

Coordinatore Dottorato

Nicolò Cavina

Supervisore

Davide Barater

Co-Supervisore

Giovanni Franceschini

Esame finale anno 2023

TABLE OF CONTENTS

LIST OF FIGURES

LIST OF TABLES

ABSTRACT

In the last years the increasing demand of higher torque and power densities has led to the adoption of hairpin windings (HWs) in electrical machines, mainly in those intended for automotive applications. However, this winding topology is quite sensitive to AC losses, hence one of their main challenges is represented by their reduction.

This work deals with different design aspects related to the enhancements of some performance figures of rotating electrical machines for traction applications, above all power density and reliability. First, the existing analytical formulations for the evaluation of active length AC losses for HWs are recalled. This model is initially used to carry out some analyses on the adoption of different materials than copper, such as aluminium. Then, a winding layout recently proposed in literature, namely segmented HW, is investigated, and the existing analytical formulation is extended, updated and validated through finite element (FE) simulations and experimental tests performed on motorettes. The main advantages and possible design issues are illustrated, as well as guidelines for the practical realization and connections of the conductors.

An additional possibility to increase torque and power density, as well as improving the reliability of the electrical drive, is the adoption of multi -phase windings. Therefore, the feasibility and the ensuing benefits of adopting a multi-three-phase HW is also investigated in this work. The analysis is carried out using the developed analytical and FE models, while a multi-three-phase HW prototype is planned to be built in the near future.

Besides investigating on multi-three-phase windings, the system reliability is pursued by modelling and estimating the voltage stress occurring both at the terminals and within windings during the device commutations of a voltage source inverter (VSI) piloting a variable speed drive (VSD). In the last years the spreading of wide-band-gap (WBG) devices has increased thanks to their capability to increase electric drives power density and efficiency, however their shorter rise times, compared to traditional Silicon-based devices, further increase the insulation voltage stress. Hence, through modelling, simulation and measurement of the voltage stress within a machine winding, this works also aims at providing solutions to increase the insulation life time. The study is performed on both “classic” random winding machines and on HWs.

1. INTRODUCTION

Nowadays, the need of reducing the global emissions is a well-known requirement in order to limit the global warming 0. Many resources are being invested to accomplish this important objective and transport electrification represents one of the necessary steps. Air transportation is seeing an important growth of more electric aircraft (MEA) research and adoption, which aims at increasing the number of electric components through the replacement of pneumatic, hydraulic and mechanical actuators with lighter and more efficient electric systems [2], [3]. On the other hand, long range air transportation is expected to proceed with traditional fuel engine propulsion systems for the upcoming years and it is not easily predictable when the technological gap for an electric propulsion will be closed.

The situation for on road transportation is different [4]-[7]. Hybrid electric vehicles (HEVs) and full battery electric vehicles (BEVs) have been already a reality for years. Their demand and production are constantly increasing, gradually replacing traditional internal combustion engines (ICEs). Hence, the main challenges for electric traction applications are different and related to increasing reliability, efficiency and autonomy of the system, decreasing costs, volumes and environmental impact, as well as improving the infrastructure that are necessary for a world large scale adoption. Of all the components of hybrid and electric powertrains, the electrical machine is a key player to achieve the above stringent requirements.

1.1 PROJECT DESCRIPTION

This PhD project is motivated by the need of pushing the boundaries for more efficient, reliable and power dense electric drives intended for transport applications, even though the majority of the findings can be extended to other applications also. The main focus is on the electrical machine and its winding. Referring to the efficiency, reliability and power density requirements, windings represent a bottleneck and a huge amount of present and past studies has been proposed aiming to improve these performance figures[2]-[6], [8], [9].

Torque and power density values of a rotating electrical machine are strictly related to the choice of the winding and of the current densities it can deliver. An important fraction of the total losses is always located in the conductors and their reduction is mandatory to keep the efficiency high and to limit the overall temperature increase. This is especially

true for HWs. In fact, while they permit maximizing the amount of copper within the machine' slots, they feature elevated losses at high frequency (HF) operation. These losses can be even exacerbated by the fast commutations typical of WBG devices, which can also cause a large electric stress on the insulation system of the machine windings. Therefore, the aim of this thesis is proposing a number of design recommendations and guidelines for achieving high efficiency, reliability and power density in electrical machines, all at the same time.

1.2 OBJECTIVES

The main objectives of this work are the following:

1) To provide a deeper understanding and analysis of HWs compared to the available literature. In much detail,
    a) to describe the state-of-the-art of such a technology, with a special focus on reviewing the methods for AC losses reduction;
    b) to analyse the reliability of the current analytical formulations for the evaluation of AC losses in conductors with a rectangular cross section, and the main sources of the discrepancy with more precise tools, such as FE simulations;
    c) to analyse the most influencing parameters, with a particular focus on the resistivity impact and on the possibility to adopt different materials than copper, such as aluminium, which has a lower cost, weight and environmental impact.
    d) to extend the analytical formulation also for different hairpin conductor topologies, such as segmented hairpins, and validating it both with a simulations and experimental results.
    e) to illustrate the main characteristics of segmented HWs and providing design guidelines for their practical realization.
2) To study the feasibility of multi-three-phase HWs, illustrating the main advantages and disadvantages, with the aim of further increasing torque and power density in electrical machines, in addition to the reliability.
3) To investigate on the voltage stress occurring in a machine winding in order to increase the winding insulation life time and the reliability of the system. In particular,

a) a numerical approach for the evaluation of the voltage stress in random winding machines is proposed and validated with experimental results. Some suggestions to increase the insulation life time are also provided;
b) the voltage stress analysis is then extended to HWs. Some simple guidelines for the realization of connection schemes which decrease the maximum peak voltage occurring between adjacent conductors are also illustrated.

1.3 OUTLINE

The thesis is organized such that the topics related to the main objectives are reported in the same logical order illustrated in the previous section. The work comprises then three main chapters (2, 3, 4) which follow the same objectives as above.

After a brief literature review on their main characteristics, Chapter 2 deals with the specific analysis on hairpin conductors, the impact of the main parameters, the classical analytical approach and its development for segmented hairpin conductors. The final part of the section deals with the analysis of segmented hairpins and their realization guidelines.

Chapter 3 starts with a general description on multi-phase machines. Then, the multi-three-phase concept is combined with the HW one, illustrating the main potentials for the automotive sector through both analytical and FE simulations. The second part of Chapter 3 comprises some optimizations and analyses of a double-three-phase machine for a future prototype realization. The last part of Chapter 3 studies the impact of the AC losses in the end winding.

As per the previous chapters, Chapter 4 starts with a brief literature review and then describes the proposed modelling approach for the voltage stress evaluation in classical random windings and HWs. For validation purposes, an experimental platform is set up using a machine stator suitably wound, showing excellent results.

Chapter 5 concludes the thesis and provide a resume of the activities.

2. THEORY AND ANALYSIS OF HAIRPIN WINDINGS

2.1 STATE OF THE ART

In the last years the research on how to increase torque and power density values of electrical machines, especially for traction application, has led to a major interest for hairpin conductors [8]-[9]. These are pre-formed conductors with a nearly rectangular cross section as shown in fig. 1.

Fig. 1. Example of hairpin conductor. It consists of two active parts/pins (i.e. two slot conductors). On the right there is the insertion side, while the portions on the left will form the welding side [14].

They present a higher slot fill factor than classical stranded round conductors, thus also a higher slot thermal conductivity is obtained. These characteristics allow to increase the electrical load without increasing the machine volume [10], [11], which usually represents a critical constraint for traction applications. In addition, differently from random windings with round conductors, the position of each conductor within the slots is always known and well defined, thus permitting a better modelling and evaluation of losses and temperature [12].

Hairpin conductors manufacturing can be quite laborious, but can be highly automated, thus fitting the large scale production requirements typical of the automotive sector [9], [13].

2.1.1 MANUFACTURING

The manufacturing process of HWs is discussed in details in [14]-[16] and it consists mainly in four phases: shaping, assembly, twisting and contacting, as shown in fig.2. First, the rectangular conductors are bent to achieve the hairpin shape (phase 1). Different hairpin shapes can be obtained and adopted depending also on the stator winding characteristics (winding pitch, slot per pole per phase, conductor numbers, etc.)

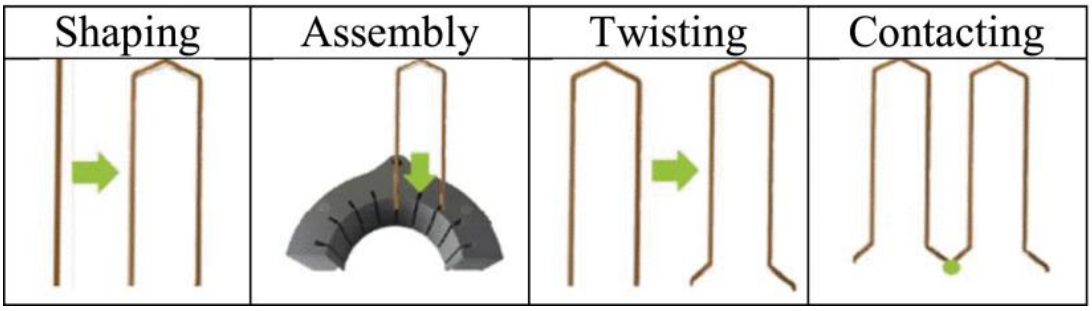

Fig. 2. HWs manufacturing main phases [14].

In order to have a uniform winding, the use of an automated process is mandatory. The second phase (insertion) is obtained introducing each hairpin in the corresponding slot. The complete pattern of HWs defined during the machine design is achieved with phase 3, where the free ends of the conductors are twisted, while during phase 4 they will be connected through welding or soldering. Contacting between two terminals of different hairpins is a crucial point since it involves the creation of contacting resistances, which should be kept as low as possible in order to limit the total winding Joule losses. In addition, their estimation and behaviour at the different loads, during the machine operation, is not easy to characterize. Another important aspect is the possibility to have a fast and automated contacting process, which is necessary to realize identical windings, with respect to the geometric and material properties tolerances. The contacting is usually realized through a welding process. Among them, laser welding is the most performing and promising [17]-[19]. The contacting resistance reaches values much lower than that considered as reference for hairpins, i.e., the hairpin active part resistance, as well as it can provide little damage to the materials. An important aspect it that, laser welding ensures a low cycle time. The main drawback is represented by the costs. For single prototyping processes, the suggested technique is instead manual soldering due to its low costs and the possibility to obtain a good result, however this process is not suitable at all for a mass production. As a general rule of thumb, in order to simplify the contacting process, it is recommended to keep the welding side as uniform as possible, thus only connections with the same pitch (full pitch) should be adopted on this side, while shorter and longer pitch connections can be adopted on the insertion side.

2.1.2 CONNECTIONS

As explained in the previous section, to realize a complete winding, the connection of the different hairpins is necessary, through soldering or welding. However, not all the

theoretically available connections are a viable solution in terms of winding losses. In fact, every conductor in a slot experiences a different impedance when subjected to a frequency dependent source. This is due to the different value of the flux density |B| in the slot along the radial direction. For this reason, when parallel paths are adopted, it is necessary that they have the same identical impedance to avoid current unbalances and additional losses, and this aspect can be accomplished only if the conductors are properly connected. More precisely, the uniformity of the impedance is accomplished through transpositions. When the number of slot per pole per phase q > 1 (or a short pitch is adopted), which is a common characteristic in traction applications, hairpins of different pitch should be adopted to perform the transpositions. In addition, much attention has to be paid to avoid mechanical interferences. Some important guidelines are discussed in [20]-[23] for the realization of proper transpositions and connections and can be summarized as follow (see also fig. 3):

1) Every path must fill equally all the slots per pole per phase independently on the occupied layers.
2) Every path should equally fill all the slot layers independently on the slot per pole per phase index.

There can be more than one way to realize a HW, but it is important that the aforementioned rules are satisfied. Some simple formulas are also available to determine the characteristics of winding, in particular for the calculation of the maximum number of possible parallel paths n_{pp} [21].

$$N_{sct} = LCM\left\{\frac{n_w pp}{2}, q\right\} \quad (1)$$

$$n_{pp} = \frac{ppqn_w}{N_{sct}} \quad (2)$$

N_{sct} is the minimum number of series connected turns, n_w the number of slot conductors, pp the number of pole pairs and q the number of slots per pole per phase. LCM stands for least common multiple. These formulas allow to know in advance the limits in terms of same impedance parallel paths that can be realized adopting transpositions. However, in some cases, some more strict rules are recommended. In short pitched windings, if a high saturation can occur, the above illustrated connections rules could not guarantee perfectly balanced impedances, thus they can be rewritten as follows [24]:

1) All the slots per pole per phase should be equally filled.
2) All the layers should be equally covered for each slot per pole per phase index.

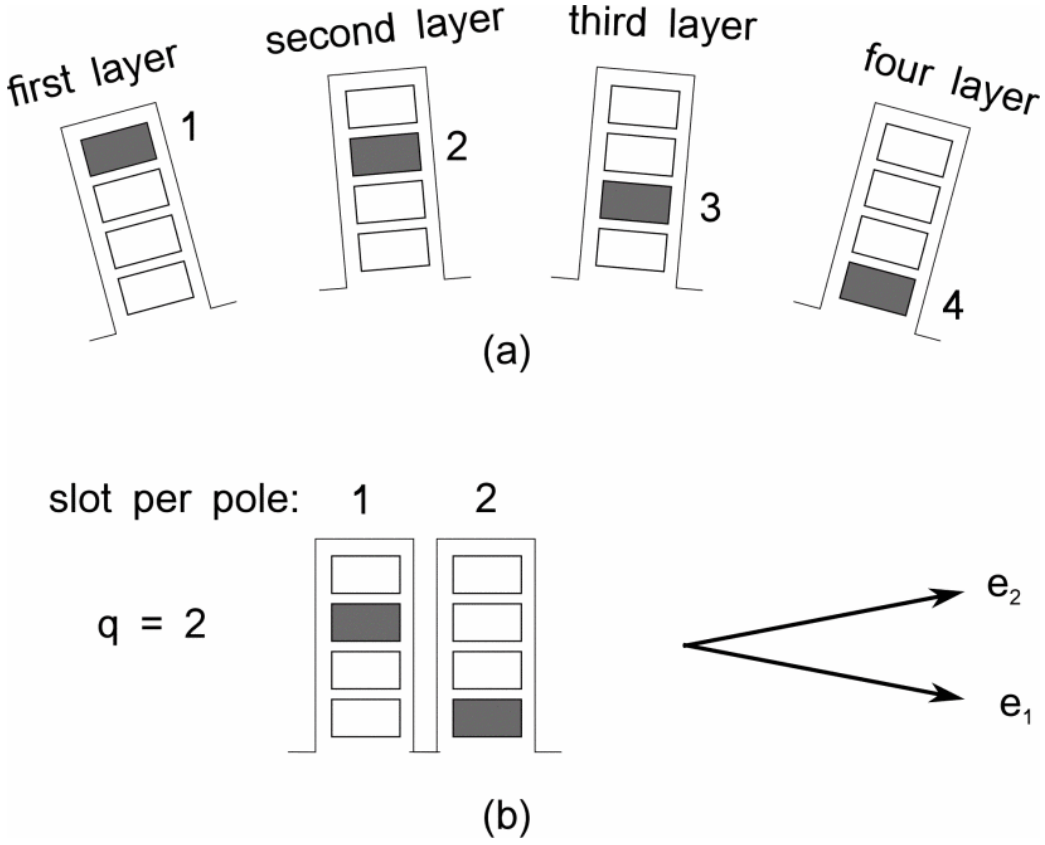

Fig. 3. Hairpin windings connection rules [21].

With these updated rules, the paths have the same identical impedances in all the operating conditions and for all the winding topologies at the cost of a more complex manufacturing. However, the initial rules are usually sufficient to achieve balanced winding. Due to the complexity and the mechanical constraint of this topology, hairpin conductors are usually adopted with a full pitch integer slot distributed winding (ISDW), even if short pitched connections are also possible. Other topologies are avoided or impossible to realize.

2.1.3 JOULE LOSSES

2.1.3.1 OVERVIEW

A reliable estimation of the Joule losses is important for every machine winding. Due to their relatively large cross section, hairpin conductors are quite sensitive to AC losses. In automotive applications the operating frequency can reach values even above 1 *kHz*, determining high AC losses due to skin and proximity effects. These phenomena make the current distribution within hairpins uneven and, additionally, each conductor within the same slot features its own distribution, with the worst scenarios occurring on the

closest conductors to the airgap. Hence, Joule losses are not evenly distributed inside the slot but are accentuated near the airgap where there is a larger influence of leakage fluxes as illustrated in fig. 4. For this reason, some research has been focused on how to specifically decrease losses in these more critical conductors. The common denominator is provided by a smaller radial dimension of one or more conductors near the air gap:

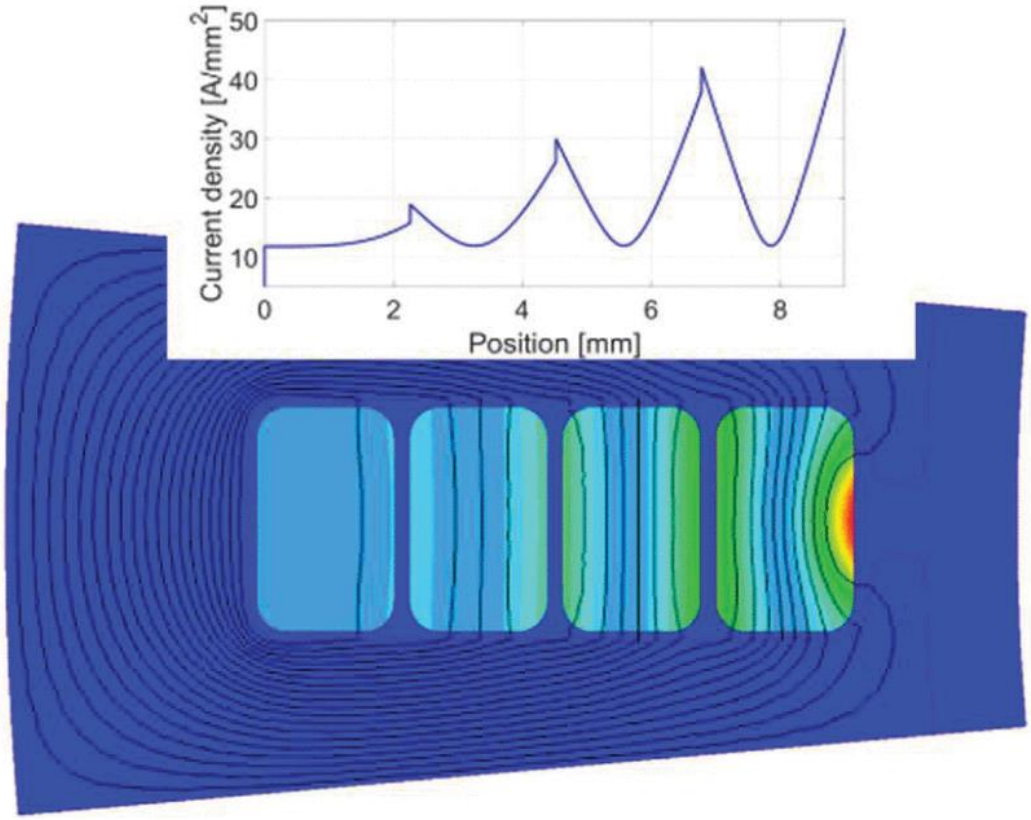

Fig. 4. Current displacement in a 2D model of a slot with 4 hairpin conductors.

1) increasing the number of conductors (and decreasing their size), whose effectiveness depends on the frequency range, usually with the introduction of some machine parallel paths [22], [23] to allow the machine operation within the voltage limits in all the frequency range. However, a higher number of conductors increases the manufacturing complexity and slightly decreases the fill factor.
2) Adopting new winding concepts, such as segmented [25], [26] (one or more conductors are split into two or more parallel sub-conductors) or asymmetric bar layouts [27] (some hairpins have a different cross section). However, also these solutions increase the manufacturing complexity.
3) Use a higher resistivity material for the conductors near the air gap, as proposed in [28]. Although the illustrated findings are of interest and promising, the results are provided only for two different frequencies and a single winding

configuration. In addition, the adoption of two different conducting materials can provide some challenges in terms of manufacturing.

However, to the author's knowledge, only solution 1) is commercially available, while the other proposed solutions have been only theoretically hypothesised or at a prototyping stage.

2.1.3.2 Classical Analytical Model

The estimation of AC losses in solid bar conductors is a topic which has been largely discussed in many studies [11], [22], [26], [29]-[31] , with a particular focus on the conductors located in the slot (i.e. the active part). These studies adopt the simplified models and hypotheses of [32], whose formulas are derived from [33]. The simplified model is illustrated in fig. 5 for $n_w = 1$.

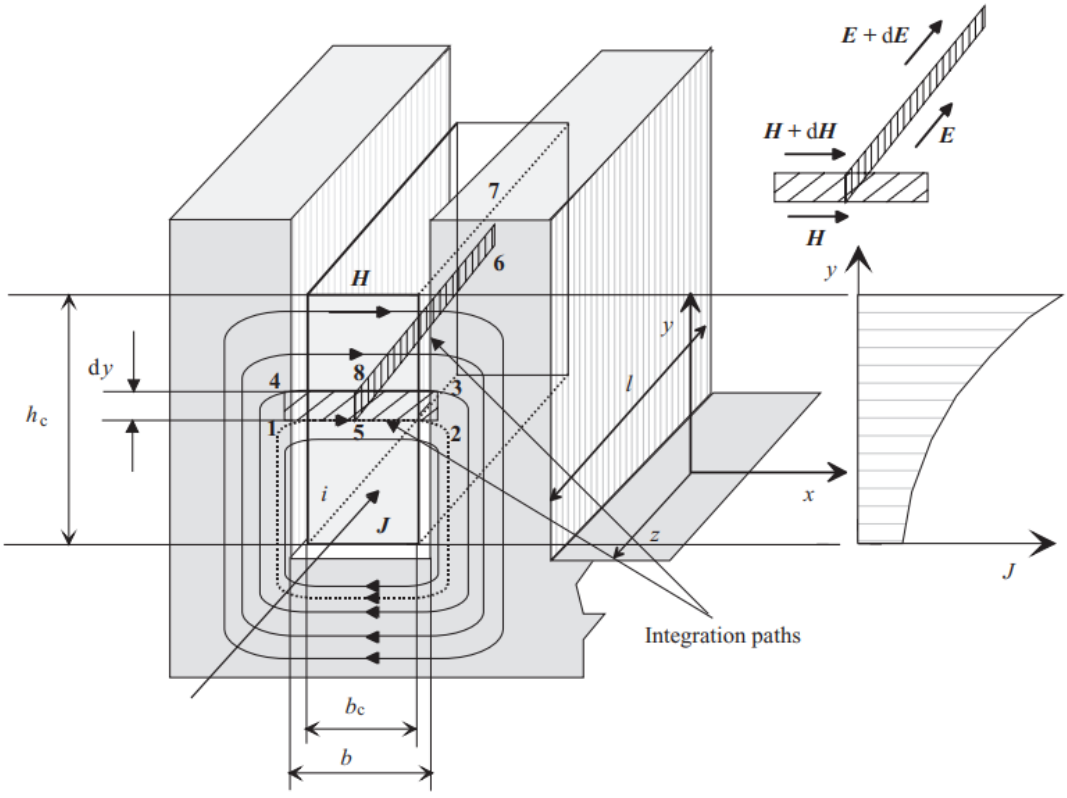

Fig. 5. Slot model for the estimation of the AC losses in a solid bar conductor.

At low-frequency operations, as well as at high-frequency operations of machines equipping stranded conductors, the winding resistance should be minimized to mitigate the Joule losses. To such purposes, copper is widely used as it presents a relatively low value of the resistivity. On the other hand, in HWs and at high-frequency operations, the current tends to become distributed within the conductor such that the current density is

largest near its surface. The current flows mainly at the "skin" of the conductor, between the outer surface and a level called the skin depth. This is defined in (3), where besides noticing that it depends on the frequency f and the permeability of the material μ, it can be also observed how the skin depth is proportional to the square root of the resistivity ρ. Therefore, its increase can have positive effects on the AC losses, contrarily to the low-frequency (or high-frequency with suitably stranded conductors) case.

$$\delta = \sqrt{\frac{\rho}{\pi f \mu}} \qquad (3)$$

Only the main formulas are reported here. Further details about how the formulas can be calculated and all the assumptions can be found in [32].

The analytical approach is based on a simple single slot model and the main hypotheses behind the following formulation are:

1) The slot is opened and with a rectangular shape.
2) The conductors are rectangular.
3) The ferromagnetic material is linear and with an infinite relative permeability (i.e. the magnetic field H is null in the core and saturation is neglected). H gradually increases going towards the slot opening (from y = 0 to y = h_c for the illustrated model) and has a not-null component only in the tangential direction. The flux density consequently has the same trend in the internal part of the slot (not considering the iron core).
4) The current density J and the magnetic field H are independent from the axial direction (z axis)

Regarding the formulation, the key parameter is provided by the ratio K_r between AC and DC losses (R_{ac}/R_{dc}). Once K_r is estimated, it becomes possible to calculate the AC losses, knowing the conductor dimensions, resistivity and the rms value of the flowing current, by simply applying (4). K_r can be calculated using (5), while the R_{ac}/R_{dc} ratio of the k_{th} slot conductor K_{rk} can be found through (6), starting to count from the slot bottom. In (5) and (6), Z_t is the number of conductors per slot, whereas $\varphi(\varepsilon)$ and $\psi(\varepsilon)$ are defined in (7) and (8) respectively, and are functions of the reduced conductor height ε. This is defined in (9), where h_c is the conductor radial dimension and α is as reported in (10), where b_c and b are the conductor and the slot widths, respectively. From (4) to (10) it can be observed that some parameters can have an important role in the determination of the Joule losses. The conductor radial dimension has to be carefully chosen since, it influences both the DC and AC resistance. A small value can contain the additional losses

due to skin and proximity effects, while a high value reduces the DC resistance, thus a trade-off, depending also on the other parameters has to be found. The frequency and resistivity are also important, as it can be seen in (10), however it appears that the radial dimension has a higher impact since the reduced conductor height is directly proportional to h_c, while the dependence on ρ and f is related to their square root. A small influence is instead provided by the tangential dimension of the conductors b_c, since it is divided by b, which is always slightly higher and, especially for larger slots, their ratio approaches 1. The conductor number Z_t can have also an important influence on the Joule losses, especially if (8) is not sufficiently small. However, for the typical frequency range of the automotive sector, (8) can be sufficiently limited with a proper selection of the conductor dimensions and its reduction has a higher impact on the overall losses with respect to Z_t, as it will be shown.

$$P_{AC} = K_r R_{dc} I^2 \tag{4}$$

$$K_r = \varphi(\varepsilon) + \frac{Z_t^2 - 1}{3}\psi(\varepsilon) \tag{5}$$

$$K_{rk} = \varphi(\varepsilon) + k(k-1)\psi(\epsilon) \tag{6}$$

$$\varphi(\varepsilon) = \varepsilon \frac{\sinh(2\varepsilon) + \sin(2\varepsilon)}{\cosh(2\varepsilon) - \cos(2\varepsilon)} \tag{7}$$

$$\psi(\varepsilon) = 2\varepsilon \frac{\sinh(\varepsilon) - \sin(\varepsilon)}{\cosh(\varepsilon) + \cos(\varepsilon)} \tag{8}$$

$$\varepsilon = \alpha \cdot h_c \tag{9}$$

$$\alpha = \sqrt{\pi f \mu_0 \frac{1}{\rho} \frac{b_c}{b}} \tag{10}$$

2.2 INVESTIGATION ON RESISTIVITY IMPACT

This section deals with the analysis of the impact of different values of resistivity on active winding Joule losses in HWs. The optimal resistivity values which minimize the losses are provided for 2 study cases, varying both number of conductors and supply frequency. The analysis is performed firstly through the classical analytical approach and then also through FE simulations. The reliability of the formulation is also discussed.

2.2.1 CASE STUDY

The analyses are performed on two different stator structures, which belong to two different permanent magnet (PM) assisted synchronous reluctance machines, respectively with 72 and 96 slots. Both the machines have semi-closed slots with the same rectangular

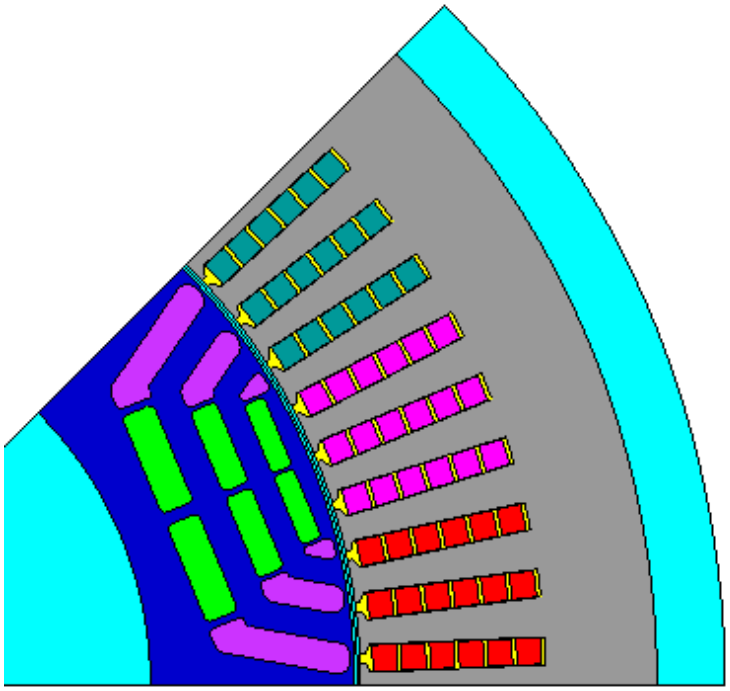

Fig. 6. One pole pitch model of the 72-slot machine, comprising six conductors per slot.

shape (i.e. with parallel sides), but characterized by different dimensions. As a consequence, also the conductors' dimensions are different, even when the same number of conductors per slot is considered, allowing to have a larger variety of results. Fig. 6 shows an angular sector corresponding to one pole pitch of the 72-slot machine, when the slots comprise 6 conductors. The 96-slot machine has the same structure, but smaller tangential and radial dimension slots, so a lower influence of skin and proximity effects is expected. On the other hand, the rotor structure is unchanged for both the considered cases. In the analytical formulation the influence of the rotor (and of magnets), the core saturation, the tooth shape and the number of slots are inherently neglected, while they are considered in the FE simulations, as it will be shown with more details in the next sections. In fact, the analytical approach is based on a single slot model, thus the main parameter which determines the upcoming findings are the conductor dimensions and their number, as well as their resistivity and the supply frequency. The analysis is performed varying these parameters as follows:

- the number of conductors per slot is varied from 2 to 10. Thus, their radial dimension is re-scaled according to their number, keeping the slot depth unchanged and such that they completely fill the slot;
- the slot depth is equal to 28.3 mm for the 72-slot model and 16.3 mm for the 96-slot one. Their tangential dimension b_c remains fixed, since also the slot width b

does not change for a specific case study. It has to be considered that the conductor width is strictly related to the slot width. In addition, as shown by (10), α depends on the square root of b_c/b, so significant variations of this ratio cannot occur;

- the slot width is b = 4.5 mm and b = 3.4 mm respectively for the 72-slot and 96-slot machine; the frequency range is set from 100 Hz to 1 kHz, which is also the operating frequency range of the investigated machines; the resistivity boundaries are chosen considering real materials, such that the provided results could have a practical validity. More precisely, the lower bound is provided by the copper resistivity at a temperature of ≈60 °C, while the upper bound is provided by the aluminium resistivity at ≈180 °C. The obtained results in this specific range can show clearly some important trends; the current is supposed to be purely sinusoidal, with a rms value which depends on the number of conductors per slot, such that the imposed magneto motive force (MMF) remains unchanged for each case study.

2.2.2 ANALYTICAL RESULTS

The analytical approach described in Section 2.1.3 is firstly adopted to estimate the optimal resistivity for each frequency value, which minimizes the losses for a specific geometry. The curves are calculated for each considered number of conductors. For each set of conductors and geometry, the active winding Joule losses have been calculated using (4), by varying ρ and f. From these results it is possible to extrapolate the optimal ρ for each frequency, thus the optimal ρ-f charts. Figures 7 and 8 show the ρ-f charts, respectively for the 72-slot and 96-slot models, taking into consideration the previously mentioned boundaries. With the exception of the case with n_w = 2, which is a rather unusual number of conductors per slot in HWs, the curves have the same shape for all the configurations. Below certain frequencies (a few hundreds of Hz for the 72-slot model), the optimal resistivity is provided by the lower limit, meaning that it is worth to adopt a lower resistivity material (copper) to minimize the winding Joule losses.

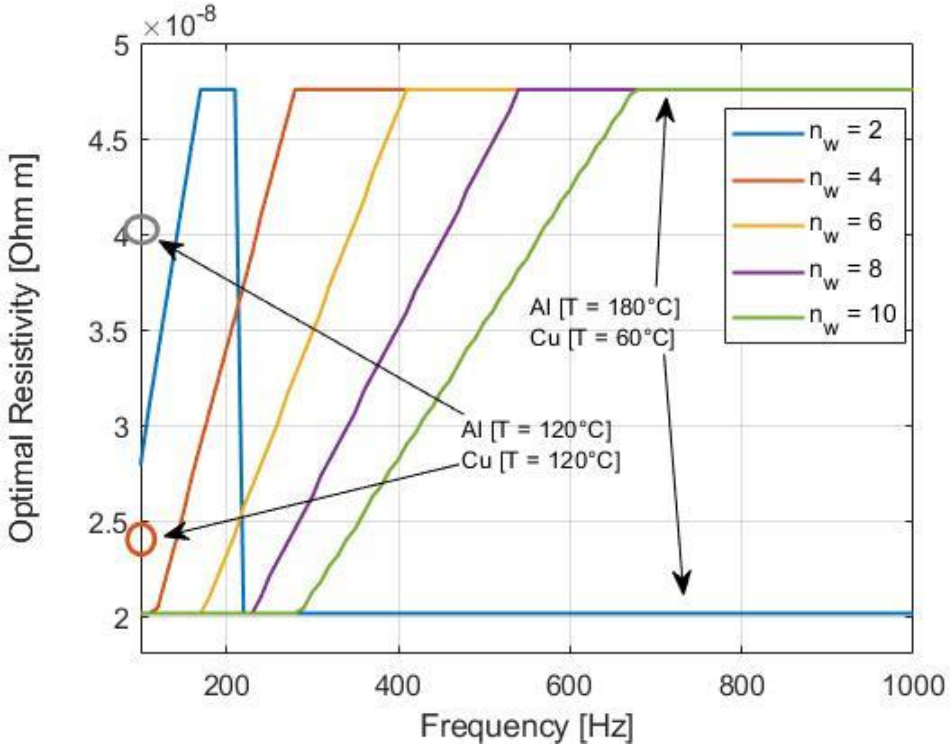

Fig. 7. 72-slot model optimal resistivity as a function of frequency. The number of slot conductors is n_w.

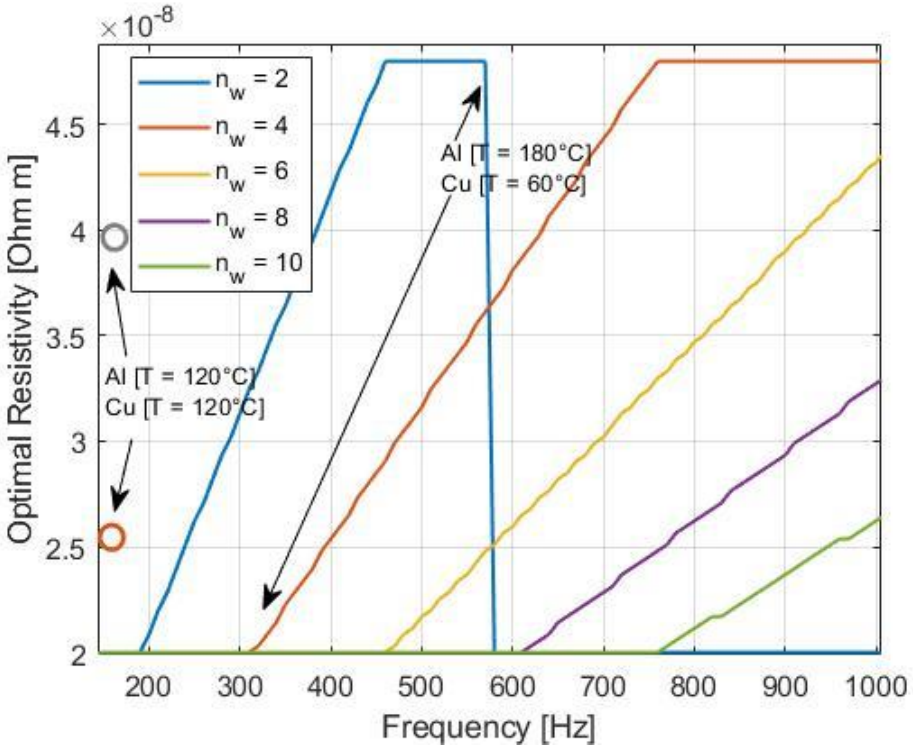

Fig. 8. 96-slot model optimal resistivity as a function of frequency. The number of slot conductors is n_w.

For higher frequency values, the optimum resistivity starts to increase, with the curves assuming the shape of a straight line until the upper boundary is met, meaning that higher

resistivity values would be preferable, but not feasible due to practical limits. It can be noticed that increasing the number of conductors per slot reduces the angular coefficient of the straight lines, as well as, the frequency value at which the optimal resistivity starts to increase is shifted towards higher values. This result is predictable since, with a higher n_w, the conductor dimensions are smaller, thus the impact of skin and proximity losses are decreased. This aspect is seen also when the curves obtained for the 72-slot model (fig. 7) are compared to those obtained for the 96-slot machine (fig. 8).

The 96-slot model can provide the same MMF of the 72-slot model, but it has smaller slots, thus smaller conductors, for a given n_w. Hence, the optimal resistivity straight line curves, are shifted to higher frequencies. Both Fig. 7 and Fig. 8 show also two representative values of resistivity, i.e. those assumed by copper and aluminum at the temperature of 120°C, respectively. These values can help in understanding when one material could be more suitable than the other, or when they can both provide similar results. Basing on the illustrated ρ-f charts, it can be noticed that the 72-slot machine, which features greater conductors, can achieve better results for a wide frequency range with the use of aluminum. On the other hand, for the 96-slot one, the copper would remain the best option for most of the configurations, thanks to presence of thinner conductors which inherently feature lower AC losses in the considered frequency range. In this case, the use of aluminum can be of interest only to reduce the maximum losses, provided at a frequency near the limit of 1 kHz. However, besides these electromagnetic analyses, it should be considered that the use of aluminum could be preferred to copper in some applications, thanks to its much lower cost and weight. In addition, it has to be considered that the hairpin conductor's radial dimension cannot be reduced below certain practical limits, thus aluminum could have an important potential for HF applications. However, for a typical automotive frequency range, it seems that copper conductors with a properly chosen radial dimension could provide better results in terms of pure losses.

2.2.3 Comparison Between Analytical and FE Results

This section provides a comparison between some of the analytical findings and the results obtained through FE simulations for some specific configurations, such that the accuracy of the analytical method can be observed and the main sources of error can be spotted. The FE analysis is performed using Flux 2D software. Fig.6 shows one of the simulated models, which corresponds to the PM-assisted synchronous reluctance machine with 72 slots. Since the simulations are carried out considering the 2D aspects only,

border and end windings effects are neglected here. In addition, the current angle has been kept fixed for all the cases. The main parameters considered in the FE analyses are the same of the analytical one, i.e. the same frequency and resistivity ranges are investigated. The conductor dimensions, for a fixed n_w, are also the same as well as the slot width and machine active length. The optimal ρ-f charts have been calculated following the same procedure. Figures 9-11 show the comparison between analytical and FE results for some specific cases, i.e. 1) 72 slot stator with n_w=6, 2) 72 slot stator with n_w=8 and 3) 96 slot stator with n_w = 6. All the other combinations are not provided as the comparison leads to same results and conclusions. It can be noticed that the trends of the curves are all confirmed with a fair precision. The main difference is provided by the slightly lower angular coefficient and shift towards higher frequencies provided by the FE curves, which means that the analytical formulation may tend to overestimate the AC losses, thus the need of a higher resistivity for a given frequency.

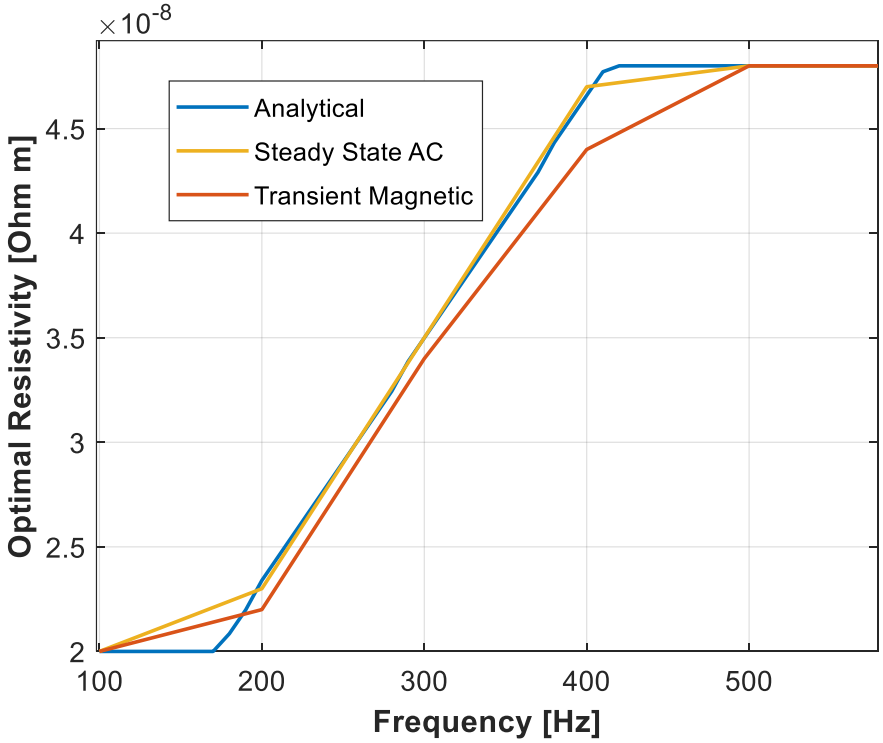

Fig. 9. Optimal ρ-f curves for the 72-slot model with six conductors per slot.

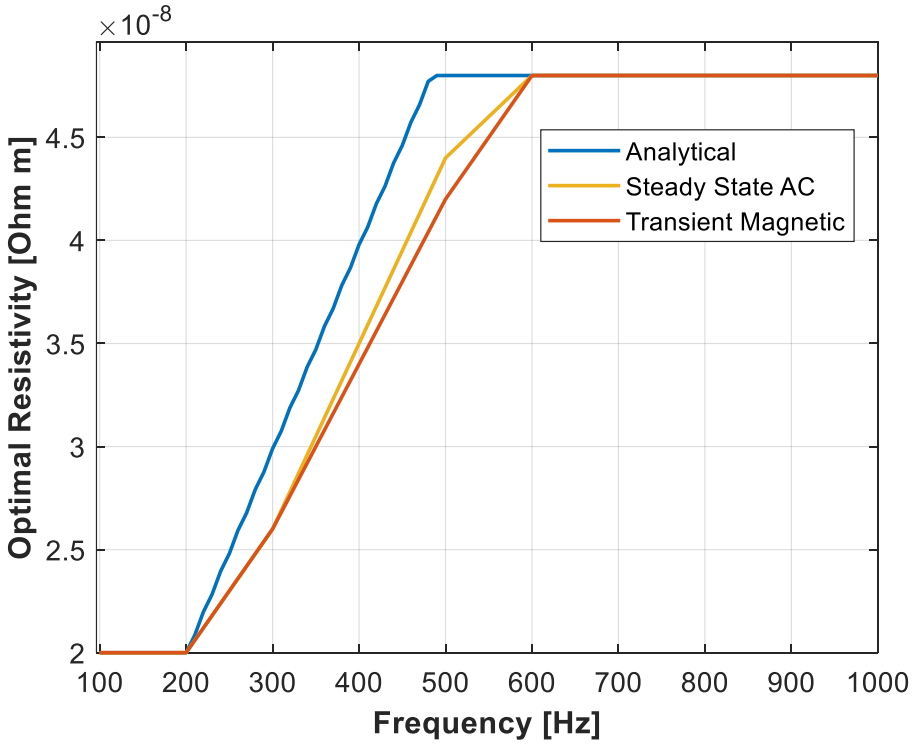

Fig. 10. Optimal ρ-f curves for the 72-slot model with eight conductors per slot

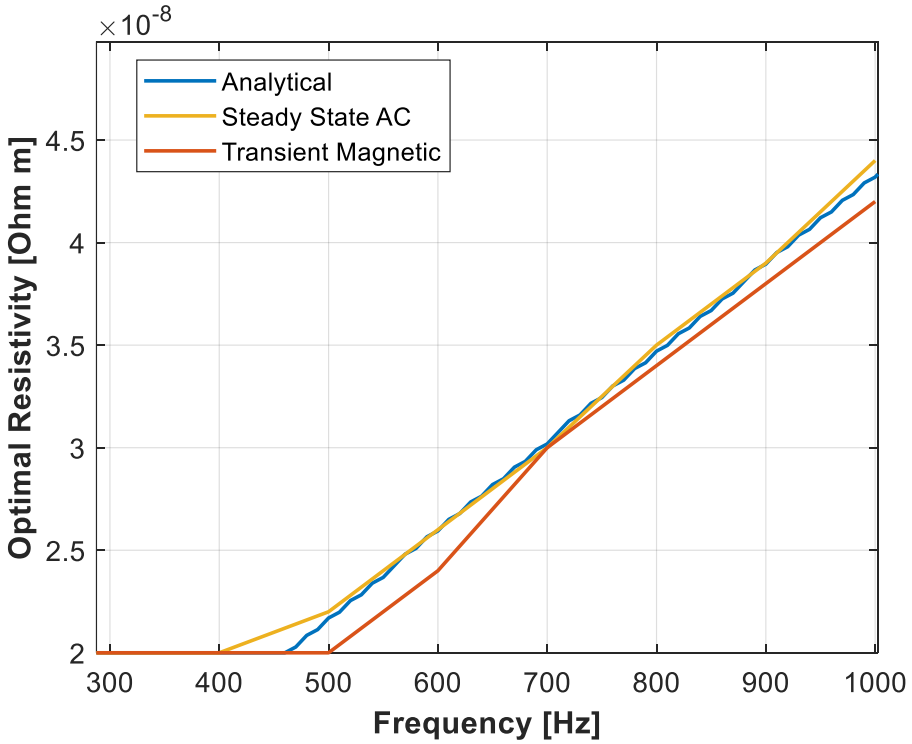

Fig. 11. Optimal ρ-f curves for the 96-slot model with six conductors per slot.

However, the difference is not so remarkable, thus the analytical results can be deemed to be rather accurate for this type of studies. Some more considerations can be done observing the figures, where an additional different type of FE solver is used to sport the

main source of error. The yellow line curve is obtained with the "steady state AC" (SSAC) FE simulation method. The SSAC assumes all the quantities as sinusoidal and, unlike the transient magnetic solver, can estimate only their average value, as in the analytical formulation. In addition, the SSAC curve is obtained simulating the stator only, as in the analytical case. It can be seen that the SSAC ρ-f curve is very similar to the analytical one for fig. 9 and fig. 11, while there is a smaller discrepancy, with respect to the transient method, for fig. 10. The SSAC FE simulations consider the different tooth shape and the core saturation, however fig. 9 and fig. 11 show that they can provide a low impact on the optimal resistivity and the frequency shift is nearly null with respect to the analytical one. On the other hand, the very similar results provide an additional validation of the analytical formulation. Thus, the comparison with the transient magnetic results, based on the whole 2D machine model, indicates that the rotor can represent the main source of discrepancy between analytical approaches and simulations. Improving the analytical model, taking into consideration only different tooth shape or the local saturation, but neglecting the rotor presence, could not provide significant benefits. For the sake of completeness, this section illustrates the quantitative impact on Joule losses given by different resistivity values, such that it is possible to provide stronger conclusions on the possible benefits and drawbacks of using a different material than copper. A comparison between analytical and transient magnetic FE simulations is performed. Figures 12-14 show the active winding Joule losses charts, as a function of frequency, for the same cases considered in the previous sub-section. Although the main trends are confirmed, the analytical formulation tends to overestimate the Joule losses for the 72-slot models, while there is a small underestimation for the 96-slot one. The reason behind this difference is attributable to the effect of the rotor presence and, more precisely, of the saturation and of the rotor internal PMs. On one hand, compared to the rotor-less analytical case, higher losses could be expected due to the magnetic field provided by the magnets as well as the influence of the rotor on the flux lines and the spatial harmonics. However, the core saturation (increased also by the rotor presence) has the effect of decreasing the ferromagnetic material relative permeability in the operating conditions and, consequently, the AC losses.

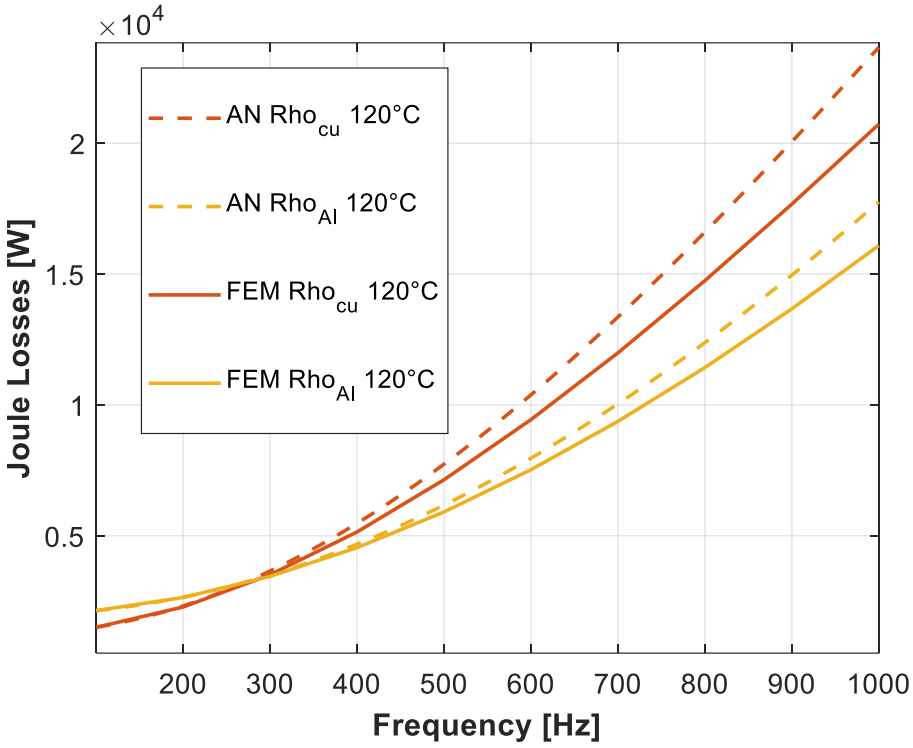

Fig. 12. 72-slot model with six conductors per slot: active Joule losses as a function of frequency - dotted lines: analytical results; solid lines: transient magnetic FE results.

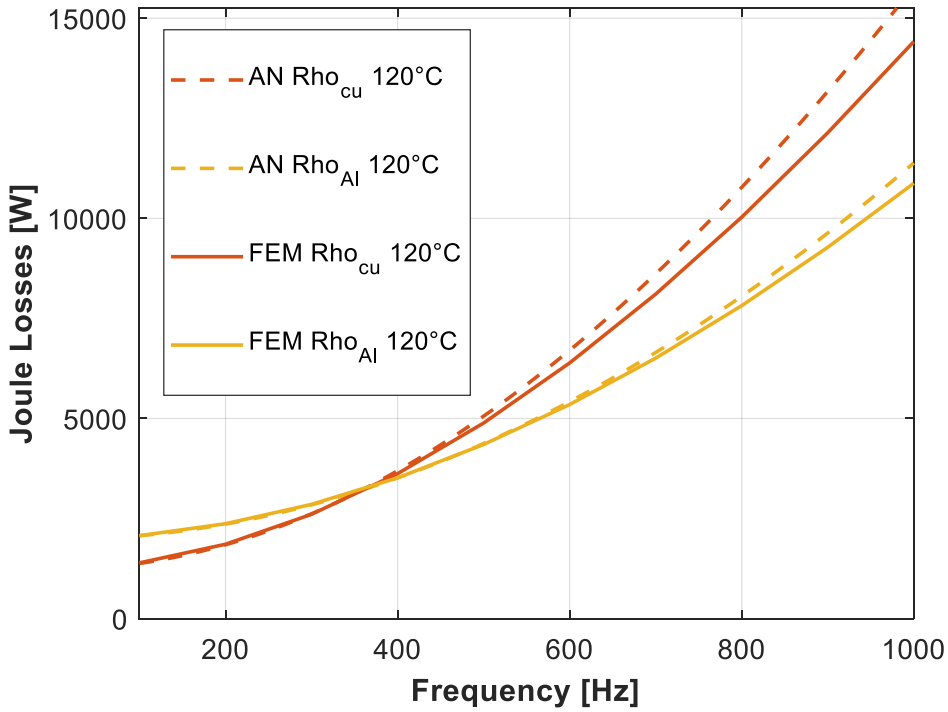

Fig. 13. 72-slot model with eight conductors per slot. active Joule losses as a function of frequency - dotted lines: analytical results; solid lines: transient magnetic FE results.

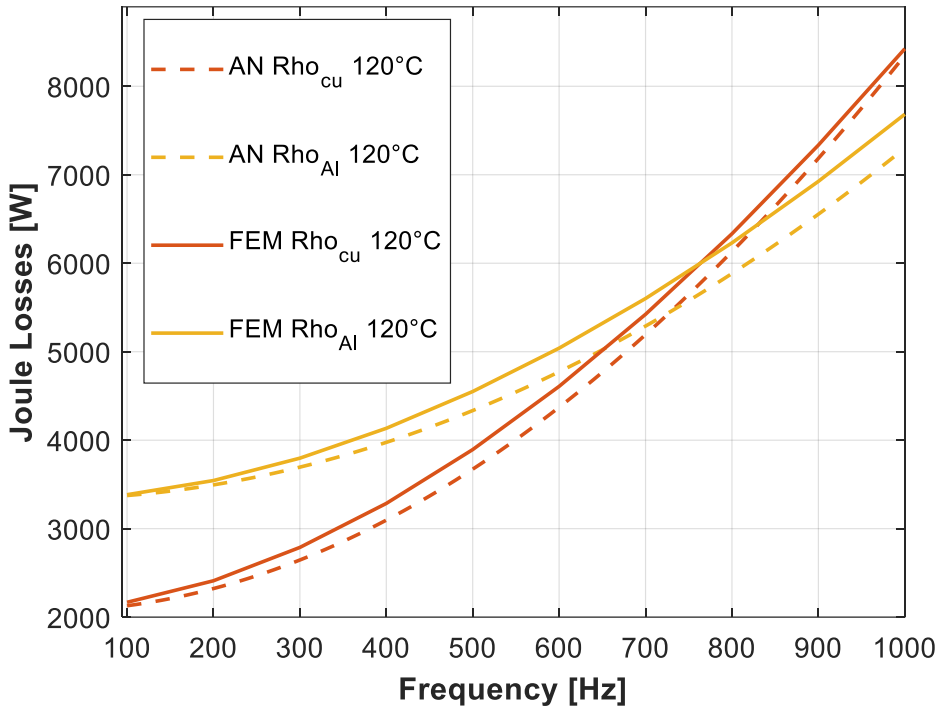

Fig. 14. 96-slot model with six conductors per slot. active Joule losses as a function of frequency - dotted lines: analytical results; solid lines: transient magnetic FE results.

Thus, two counterbalancing actions are acting on the AC losses, resulting in a small under- or over-estimation. A final important consideration should be done on this aspect. The PMs of the analyzed machines have only the aim of enhancing the output torque, thus their action on the magnetic field, hence on Joule losses, is not predominant. However, for a different machine topology, such as in surface-mounted PM machines, the differences between analytical and FE method could be more significant, thus further studies would be required.

Two representative resistivity values have been chosen for the loss comparison. Higher values of resistivity have the effect of flattening the curves, increasing the low frequency losses and decreasing the impact of higher frequencies. It is more evident now that the 96-slot machine does not have particular benefits from the use of aluminum, which could provide lower active Joule losses only above 800 Hz.

This limit could be even pushed to higher values with thinner conductors. On the other hand, the 72-slot machine, having larger conductors, can reduce the active Joule losses for a wide range of frequencies thanks to the aluminum. Specifically, the 72-slot machine with eight conductors per slot made of aluminum can provide a comparable amount of losses compared to the 96-slot machine, thus it could be an interesting lower cost alternative.

2.2.4 Conclusion On The Impact Of Resistivity

This section presented an analysis on the impact of the resistivity on Joule losses in HWs. Two PM-assisted synchronous reluctance machines intended for automotive applications were considered as study cases.

An analytical model was developed to investigate on these aspects. It was shown that, depending on the number of conductors per slot and their dimensions, the aluminum can be beneficial for AC losses reduction. The aluminium can provide positive results from a few hundreds of Hertz for the 72-slot machines, since they have conductors with a greater radial dimension. The 96-slot machine, having smaller cross section conductors, can obtain benefits from aluminium going towards 1 kHz. However, since it is not possible from a practical point of view to reduce the radial dimension below certain thresholds, the aluminium benefits could become important at higher frequencies, representing an interesting solution for all the applications which operate for a significant amount of time above 1 kHz. For applications below 1 kHz, a proper choice of the conductor radial dimension can ensure lower Joule losses with copper.

The analytical findings were validated through FE simulations. The analytical formulation showed an acceptable accuracy in detecting the optimal resistivity which minimizes the AC Joule losses. The main source of discrepancy was attributed to the rotor presence in the models, which however does not have a significant effect in the machine topology analyzed in this paper. On the other hand, for different rotor structures, the error of the analytical model could become significant, thus further research would be needed.

2.3 Updated AC Losses Analytical Model and Design Guidelines for Segmented HWs

As previously stated, one of the available proposed solutions to decrease the AC losses in HWs is the adoption of segmented hairpins, as shown in [25], [26].

2.3.1 Background

Segmented hairpins represent an interesting technique to reduce AC losses. This new configuration comes from the “strand” concept typical of random windings, where the conductor is divided in several parallel-connected sub-conductors (strands). In hairpins, this method cannot be applied as flexibly as in random windings. The number of parallel-connected elements should be kept low to avoid unfeasible solutions or excessive

complications of the bending and welding processes [14], [16]-[18]. Fig. 15 provides a simple example which can help in a better understanding of the concept [25]. Both the illustrated solutions (conventional and proposed, i.e. segmented) are magnetically identical, since they provide the same number of equivalent slot conductors, which is 4. The segmented configuration has a total six layers, since the last two equivalent conductors have been divided into 2 sub-conductors each. Each sub-conductor carries half the current of the other conductors, thus the total slot MMF remains unchanged, as well as the theoretical flux linkage as for a conventional 4 conductor solution. Hence the main advantage of this solution is that it allows to decrease the winding AC losses keeping the overall machine parameters unchanged and without increasing the DC resistance of the equivalent conductors.

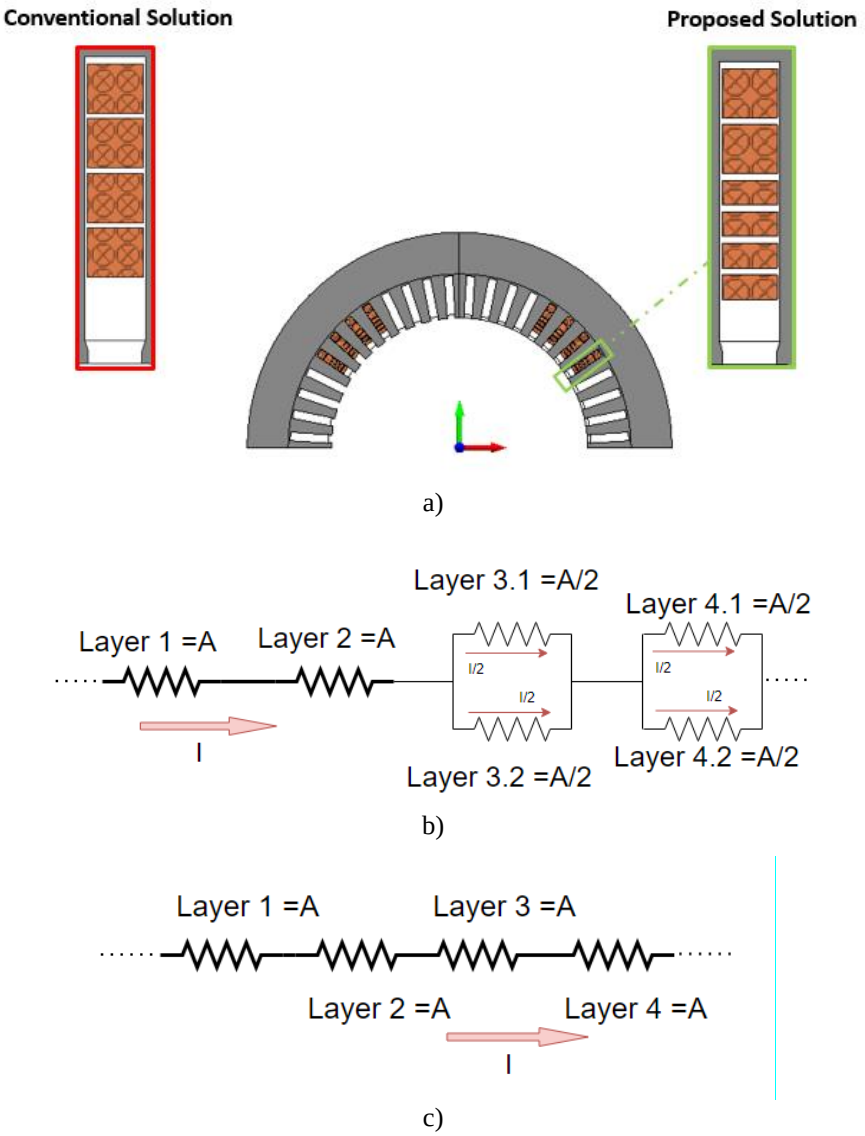

Fig. 15. Illustration of the segmented hairpin concept (proposed solution); (a) 2D FE model slot overview; (b) segmented circuital schematic; (c) conventional solution circuital schematic [25].

2.3.2 OBJECTIVE

While the potential of segmented HWs is very promising, a deeper analysis is necessary on this topic, as no guidelines for the practical realization have been presented in literature. The parallel connections should in fact be realized keeping a balanced winding. In [26] a valid analytical approach for the evaluation of the AC losses in segmented hairpin conductors is illustrated, however a compact and faster formulation which can provide the losses as in [32] for the classic layout is missing.

The objective of this section is to investigate different aspects of the segmented HW topology, addressing the aforementioned topics. First, basing on the consolidated analytical approaches, a simple and compact analytical formulation for the evaluation of frequency dependent Joule losses in segmented HW is derived. The correlation between the number of sub-conductors n_{sub} and the AC/DC loss ratio K_{rk} for each winding layer is underlined, as well as the main differences with other formulations. This analytical formulation is then validated through the comparison against experimental results. The validity of the analytical approach is enhanced through the comparison with FE simulations for different cases. In addition, the main advantages, disadvantages and possible errors in their dimensioning are underlined. The work is then concluded providing some simple guidelines for the practical realization of HWs with segmented conductors' connections and transpositions. Formulations for the calculation of the machine parallel paths and for the estimation of the number of welding spots are also finally provided.

2.3.3 DEVELOPED FORMULATION

The classical formulation for the evaluation of AC losses in HWs is valid only if all the conductors placed in a slot carry the same current (i.e. are series connected). Otherwise the formulation is no longer valid as shown in [26]. In fact, the distribution of |B| is changed and consequently also the K_{rk} of some conductors. In [33] Richter proposes a more general formula, shown in (11), which is based on the magneto-motive force (MMF) rather than the layer position. From (11), (6) is derived when all the conductors are series connected.

$$K_{rk} = \varphi(\varepsilon) + \frac{\theta_u(\theta_u + \theta_p)}{\theta_p^2}\psi(\epsilon) \qquad (11)$$

In (11), Θ_u is the MMF produced by the first k-1 layers, starting to count from the slot bottom. Θ_p is the MMF of the k layer, when all the other layers are ignored, i.e the current

flowing in the layer *k*. Considering that the current flowing in each conductor is I/n_{sub}, the MMF can be written as in (12) and (13). Starting to count from the slot bottom to the layer *k*-1, $n_{s,k-1}$ is the number of layers which are not divided into sub-conductors, while $n_{seg,k-1}$ is the total number of encountered sub-conductors counting the same way. Dividing (13) by the current *I*, (14) can be obtained. N_u is then the number of equivalent conductors from the first, to the layer *k*-1. Then, substituting (12) and (13) into (11), (15) is obtained.

$$\theta_p = {}^{I}/_{n_{sub}} \tag{12}$$

$$\theta_u = n_{s,k-1} I + n_{seg,k-1} {}^{I}/_{n_{sub}} \tag{13}$$

$$N_u = n_{s,k-1} + {}^{n_{seg,k-1}}/_{n_{sub}}. \tag{14}$$

$$K_{rk} = \varphi(\varepsilon) + N_u(N_u + {}^{1}/_{n_{sub}}) n_{sub}^2 \psi(\epsilon) \tag{15}$$

Fig.16 provides an example of a 2D slot model with segmented conductors on which the analytical formulation is based on.

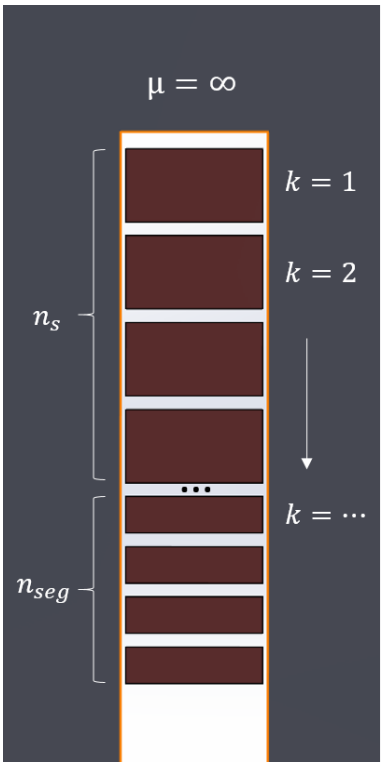

Fig. 16. Example of a 2D slot model with segmented conductors on which the analytical formulation is based on.

The non-split conductors are the thicker ones on the slot bottom side (k = 1, 2 …), represented by n_s, while the segmented ones (sub-conductors) are underlined with n_{seg}

and are those nearer to the slot opening. If no conductors were segmented (n_{sub} = 1), the same current *I* would flow in each layer and it can be easily verified that (12) equals (3). On the other hand, (12) illustrates one important aspect related to segmented conductors. While the first term $\varphi(\varepsilon)$ is equal for all the formulations and is linked to the skin effect, the second term of the equation is proportional to the second power of the number of sub-conductors which compose an equivalent conductor. Therefore, it is necessary that all the sub-conductors present a small radial dimension (around 1 mm is suggested) such that the adoption of this configuration is beneficial, as it will be shown also in section 2.3.5. In addition, it is recommended a value of n_{sub} = 2, as higher values would increase the manufacturing complexity and decrease the benefits of segmentation. With these measures, it is possible both to limit the AC/DC factor of each equivalent conductor and keep their DC resistance low thanks to the parallel connection of the sub-conductors.

2.3.4 Experimental Validation of the Proposed Analytical Formulation

The aim of this section is to provide a first validation of the analytical formulation illustrated in (15). The comparison is performed against experimental measurements of the total copper Joule losses carried out on a motorette with rectangular segmented bar conductors. The experimental results on the motorette are provided in [25], a work presented by some researchers and former researchers of the same department as the author of this thesis, where some measurements have been presented for the first time to prove the potentials of segmented hairpin conductors. However, the main aspects of the test procedure and the test rig are also illustrated in this section. The motorette is illustrated in Fig. 17, while the main data are shown in Table I. It has the first two conductors which are not split, while the remaining two are split into two sub-conductors (n_{sub} = 2), for a total of six layers and four equivalent conductors per slot. The test rig is instead illustrated in fig. 18. For the sake of consistency with the sinusoidal supply assumptions used in both analytical and FE evaluations, the signal feeding the motorettes is first produced by a SiC Voltage Pulse generator with 60 *kHz* switching frequency and, then, filtered by a low pass LC filter with a cut-off frequency at 2 *kHz* to obtain an output signal as close as possible to a pure sinusoidal waveform. The power loss is measured by a precision power analyzer (PPA 5530) and an oscilloscope is used to double check the losses value and the signal waveforms. All measurements are taken at the same

temperature ($20°C$) and the winding temperatures are monitored with a thermal camera during testing. Regarding the comparison, it should be underlined that (15) can estimate only the active losses, while the measurements clearly include also the end winding losses, which cannot be neglected, as well as the additional resistances provided by the welding spots.

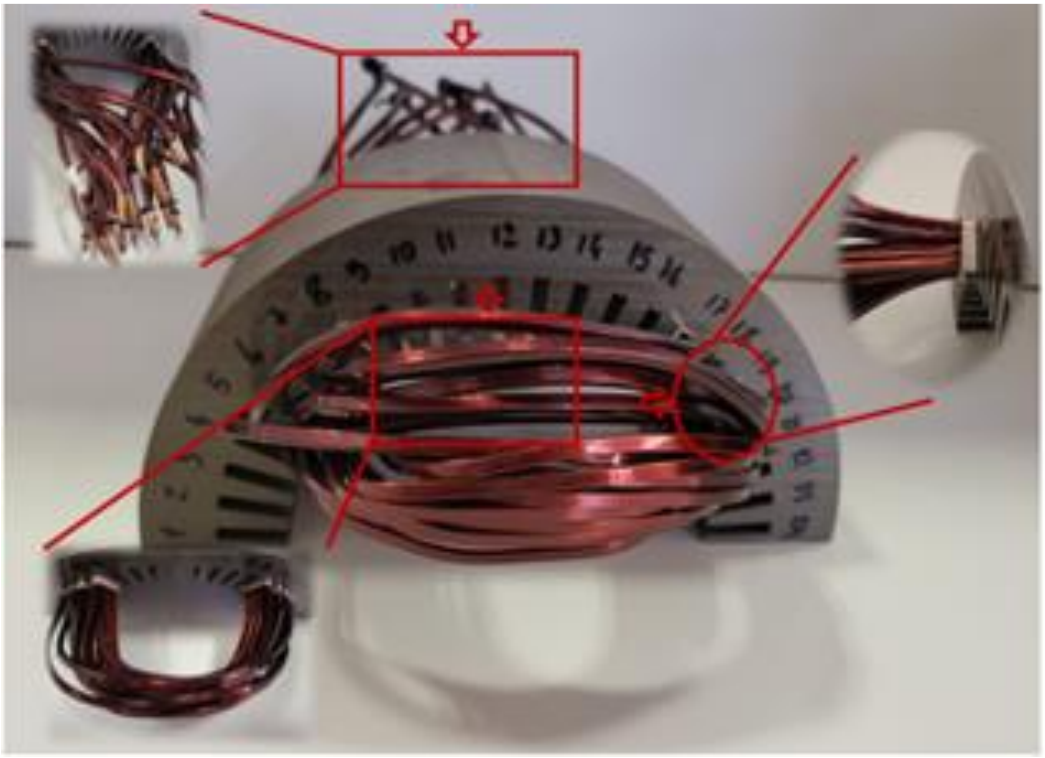

Fig. 17. Motorette for experimental measurements [25].

Hence, an estimation of the end winding losses is needed and can be performed via a FE analysis. The total (semi-) analytical losses $P_{3D,an}$ are computed as (16). $P_{2D,an}$ are the slot conductor Joule losses estimated with the proposed formula in (12), while $P_{ew,FE}$ are the end winding losses estimated with the FE simulations.

Table I. WINDING MOTORETTE'S DATA

Slots	8
Layers	6
Equivalent conductors	4
Sub-conductors	2
Conductor dimensions [mm]	4x3.5
Sub-conductor dimensions [mm]	4x1.75
End winding length (one conductor) [mm]	172
Slot width [mm]	4.4
Active length [mm]	92

$$P_{3D,an} = P_{2D,an} + P_{ew,FE}. \qquad (16)$$

$P_{3D,an}$ is then compared with the experimental results at the following frequencies: 1, 100, 200, 400, 800 and 1200 Hz. The procedure and the details of the end winding FE model are also treated in detail in [25], where the end winding losses have been calculated as well.

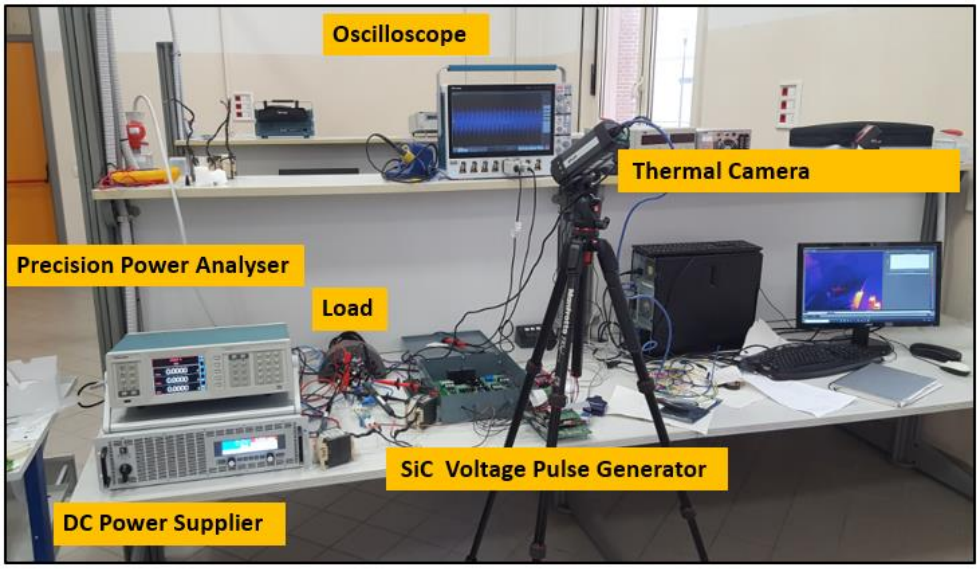

(a)

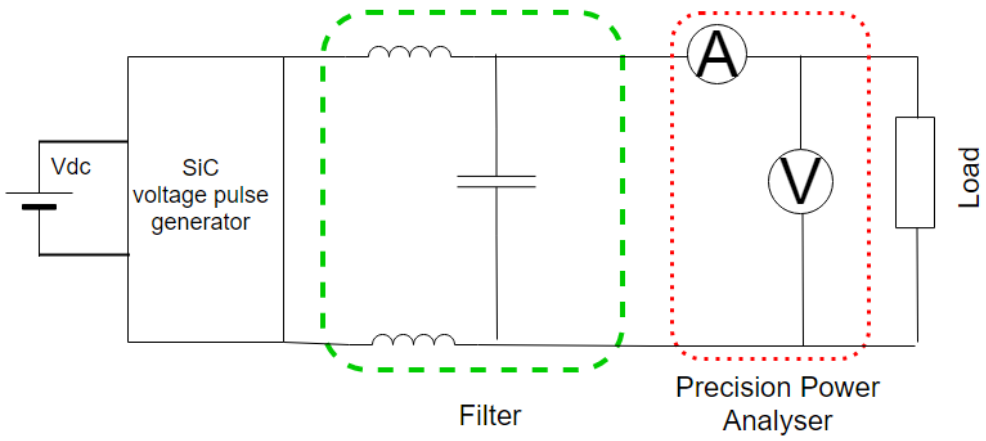

(b)

Fig. 18. Experimental test setup: (a) test setup. (b) Schematic overview.

However, the main steps are also reported here. First, the total winding resistance R_{3D} of the motorette is extracted with an RLC meter. Knowing the active length of the machine and the conductor geometrical parameters, which are reported in Table I, it is straightforward to compute the winding active length resistance R_{2D}. At this point the end winding resistance R_{ew}, including the contribution of the welding spots is simply provided

as $R_{ew}=R_{3D}-R_{2D}$. Then, from R_{ew}, the equivalent end winding length can be easily obtained. Its value is also reported in Table I. From the equivalent end winding length a simple equivalent end winding model has been built in and adopted for the estimation of $P_{ew,FE}$ from DC to 1.2 kHz. From the calculated losses, it is then straightforward to estimate K_r, by dividing the frequency dependent losses by the DC losses. The comparison between the AC/DC loss ratio obtained with (15) and the experimental measurements are reported in Fig. 19.

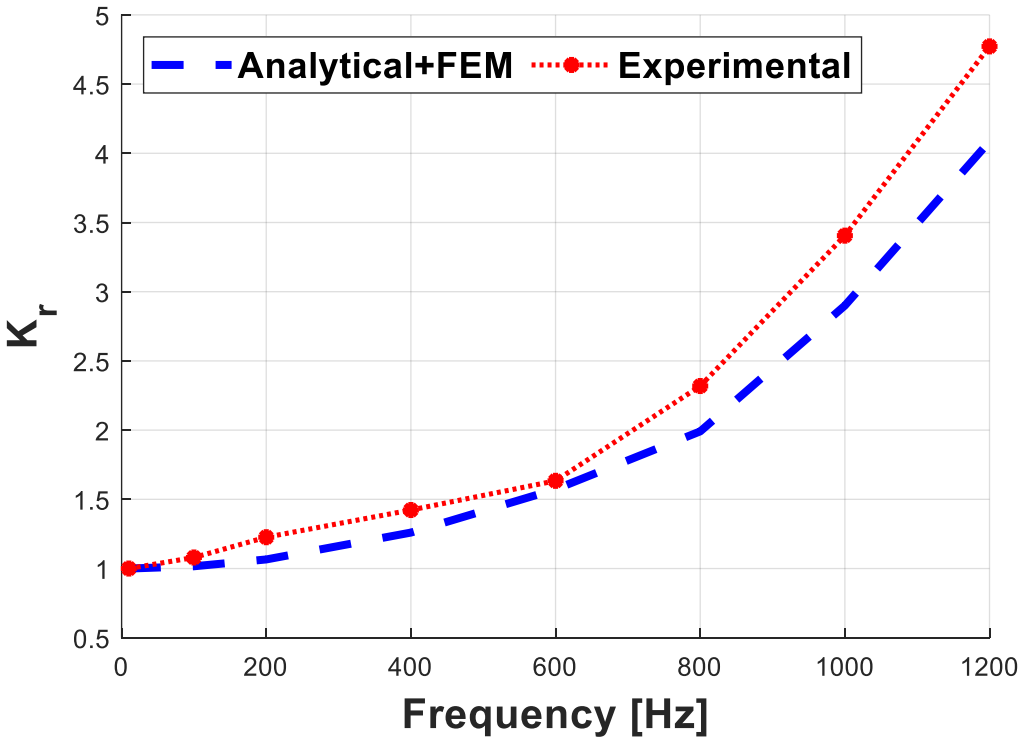

Fig. 19. Comparison of analytical and experimental K_r.

As expected, there are some discrepancies, but the analytical approach presents a good accuracy, indicating that the results should be similar to the one provided by the FE simulations. This aspect is better illustrated in section IV. Regarding the discrepancies between analytical and experimental results, the main sources of error can be identified as:

- The frequency dependent behaviour of the welding resistances, which is not known yet.
- The influence of border effects on the end winding losses. The simplified end winding model presented in [25] does not consider the influence of border effects in the end winding region. Although the main part of the motorette end windings

is relatively far from the stator core, the border effects can have some impact on the total losses.

- A minor impact can be also provided by the presence of current harmonics, even if the current has been suitably filtered, as well as possible differences between the real ambient conditions and those considered in the analyses, and/or between the considered copper resistivity and the realistic value.

2.3.5 FURTHER ANALYSES AND CONSIDERATIONS

This aim of this section is twofold, i.e. 1) to enhance the validity of (15), through the comparison of the active length winding Joule losses against 2D FE simulations from DC to 1.5 kHz for some stator models; 2) to provide further data regarding hairpin segmented conductors and discussing advantages and disadvantages for different cases.

The analysis is performed comparing a classical HW arrangement with six conductors per slot against three different HW configurations with segmented conductors (namely N5, N5v2, N6). N5 has six layers, but five equivalent slot conductors, in fact the last equivalent conductor results from two thinner sub-conductors. N6 has the last two equivalent conductors which are composed of four total sub-conductors (two per equivalent conductor), for a total of eight layers and six equivalent conductors. N5v2 is similar to N5, with the exception that the two sub-conductors are not thinner but present the same radial dimensions of the other layers, which is an example of design to avoid. In fact, since in (12) $\psi(\epsilon)$ is multiplied also by n_{sub}^2, it is necessary to select a sufficiently small radial dimension to contain it and the resulting K_{rk}. It is important to note that, in order to make a fair comparison, the same materials are adopted for all the cases, as well as the external and internal stator diameter dimensions, the active length, the conductor and the slot width are kept the same. The main data are reported in Table II. Fig. 20 provides a picture of one of the adopted 2D models for the simulations. A fine mesh is adopted such that the results can be sufficiently reliable, while the simulations are carried out with a time harmonic 2D solver imposing a sinusoidal current from 0 to 1.5 kHz and the same slot total MMF for all the models. The adopted software is Simcenter Magnet.

Table II. FE MODELS DATA

Topology				
	Classic	Seg N5	Seg N6	Seg N5v2
Slots	24	24	24	24
Layers	6	6	8	6
Equivalent conductors	6	5	6	5
Sub-conductors	1	2	2	2
Conductor dim (no seg) [mm]	4.5x2.2	4.5x2.2	4.5x2.2	4.5x2.2
Sub-conductor dim [mm]	-	4.5x1.1	4.5x1.1	4.5x2.2
Slot width [mm]	5.3	5.3	5.3	5.3
Slot height [mm]	15.4	13.2	15.9	15.4
Stator material	M270-35A			

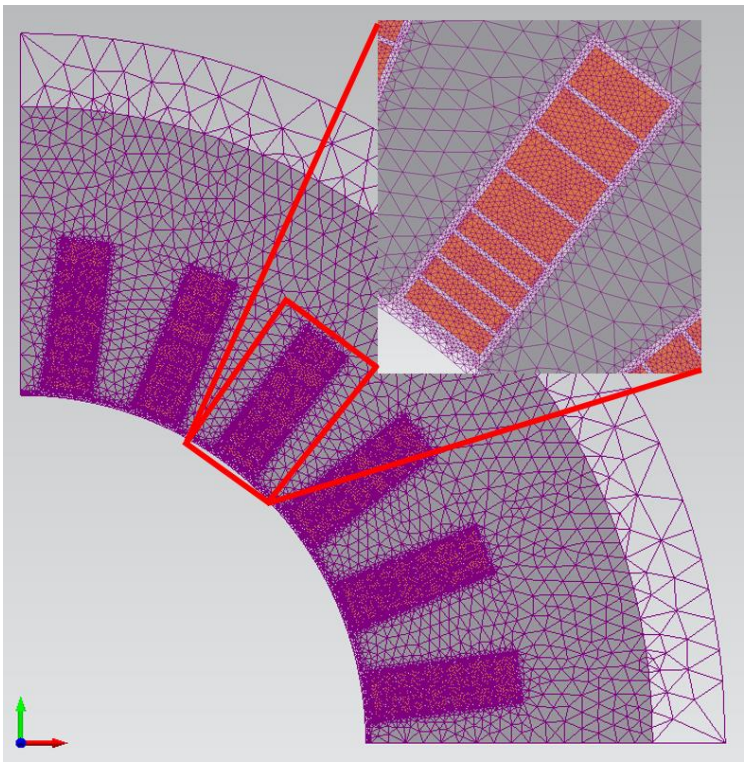

Fig. 20. 2D FE model of N6 configuration. The mesh is displayed.

The results of the comparison between the classical and the segmented configurations are shown in fig. 21, whereas fig. 22 provides a comparison in terms of K_{rk} for all the layers of N6. All the results are provided both by FE simulations and the losses obtained with the updated analytical formulation. The first important aspect is that there is an excellent match between analytical and FE results, for the classical and for all the segmented configurations, with an error which is below 1% for the whole frequency range. This match is also favoured by the fact that without the rotor influence no saturation occurs, while its presence would potentially introduce some errors, as underlined in section 2.2.3. However, these results prove the validity of (15), which is one of the main aims. The second aspect is that both N5 and N6 can provide an important reduction of the copper Joule losses.

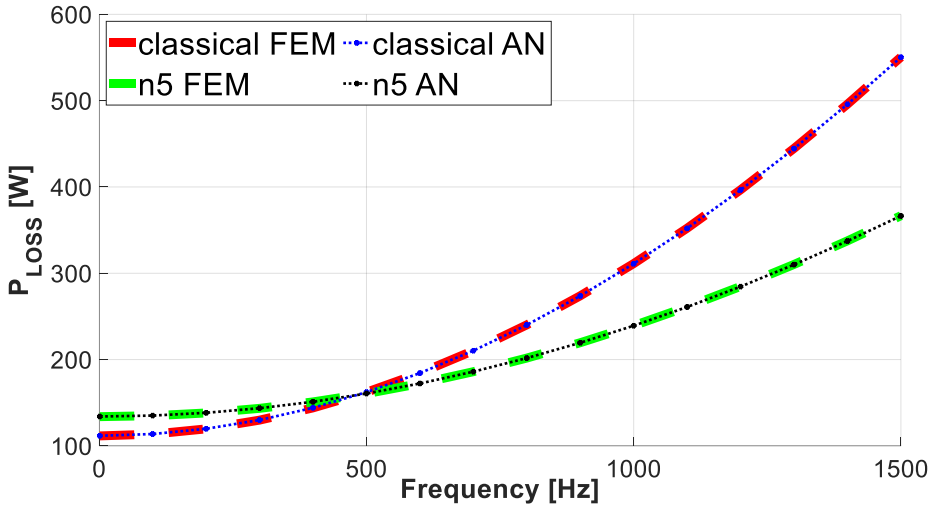

(a) Segmented N5 vs classical.

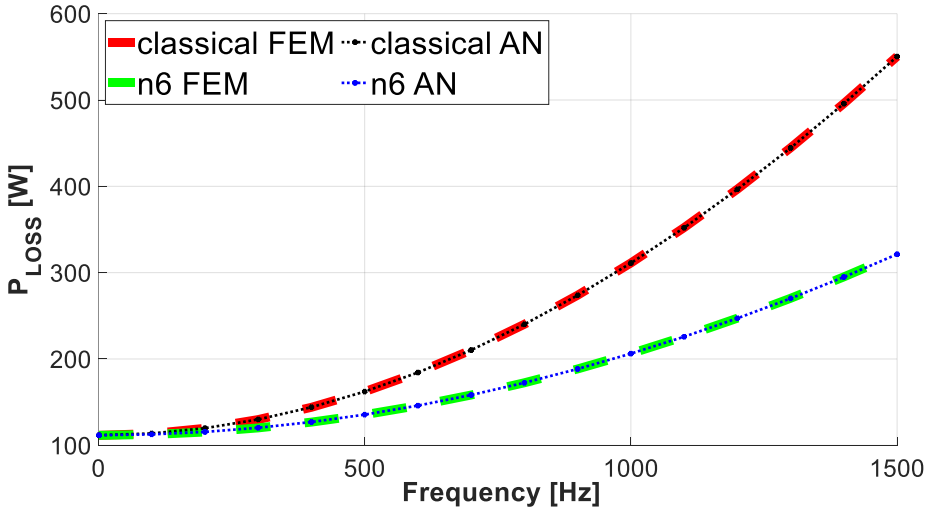

(b) Segmented N6 vs classical.

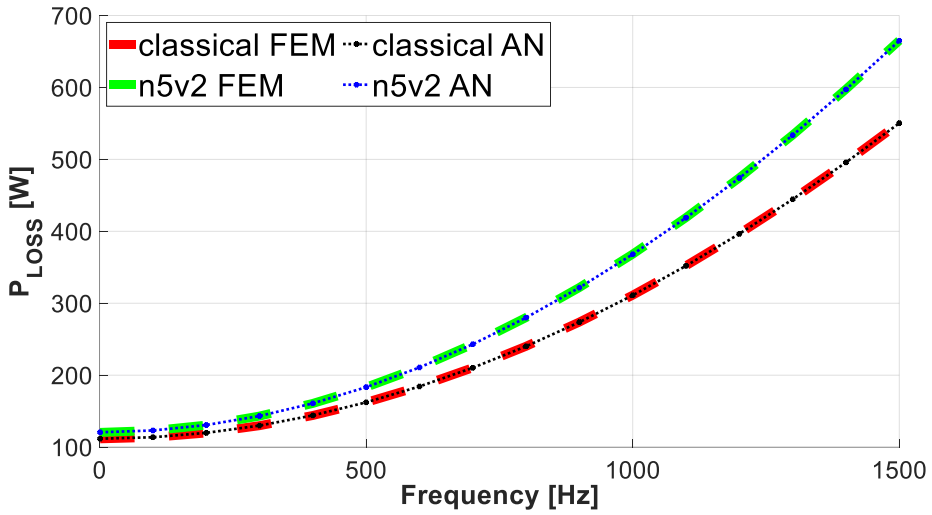

(c) Segmented N5v2 vs classical.

Fig. 21. Active length winding Joule losses.

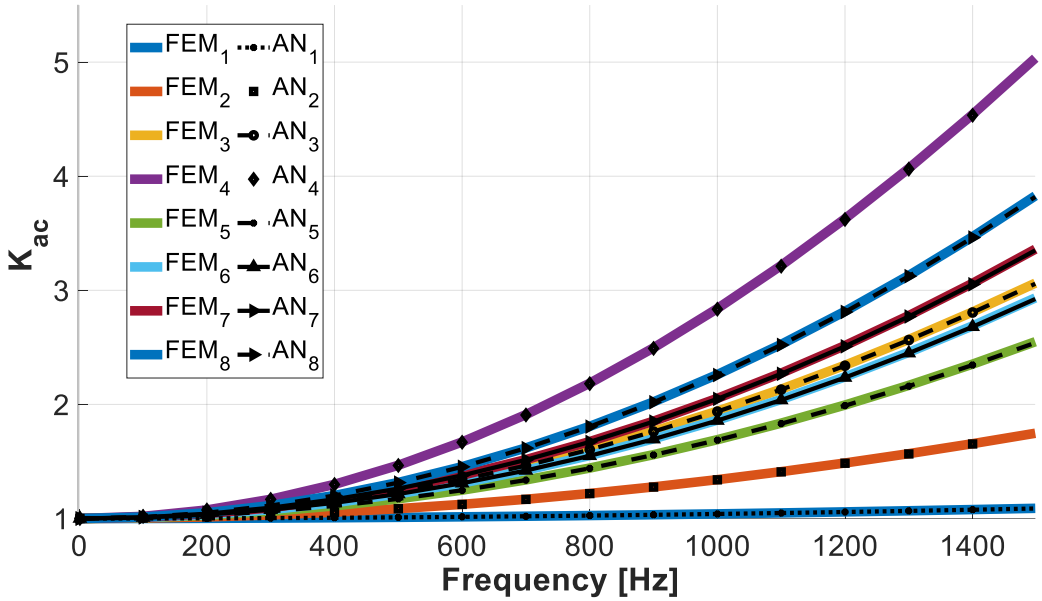

Fig. 22. AC/DC ratio K_{rk} of each layer for N6 configuration.

N5 has a lower copper content and a higher DC resistance. In addition, being the equivalent number of conductors lower, it needs a higher current to provide the same MMF, leading to higher DC losses. Despite these limitations, N5 has lower losses starting from 500 Hz and presents reduced losses at high frequencies compared to the classical configuration. Additionally, the lower number of equivalent conductors would allow for a slightly wider constant torque speed region compared to the other investigated configurations, if the same rotor was adopted. In fact, a lower number of equivalent conductors determines a lower induced voltage, when the same operating frequency is

adopted, thus the voltage limit is met to a higher speed. On the other hand, N6 has the same amount of copper and number of equivalent conductors as the classical configuration, thus the same DC losses and operating current. However, it can provide lower losses for the entire frequency range and an important improvement when approaching 1 kHz. Contrarily, N5v2 has higher losses for the entire frequency range compared to the classical HW. In fact, it needs a higher current, as well as N5, but cannot provide a reduction of losses for the higher frequencies. The reason is that the two sub-conductors are not sufficiently thin. Hence, a wrong selection of the sub-conductors' radial dimension can lead to much higher Joule losses and to the inefficiency of the adopted configuration.

2.3.6 WINDING REALIZATION GUIDELINES

In this section, an example of possible connections for the realization of a segmented HW is illustrated and some more general guidelines are provided. The adopted convention for the connections and transpositions is the same as in [20], which consists in keeping the welding side as uniform as possible. Hence, hairpins with different coil pitch are adopted on the insertion side. It is well known that a HW is made of a certain number of paths featuring all the same impedance to avoid current unbalances and additional Joule losses. Then, these can be series or parallel connected. Fig. 23 provides an example of a possible winding diagram for a three-phase, 4-pole machine, having the same configuration of the N6 model. Only one of the two resulting machine parallel paths is displayed. The proposed approach is the following. The machine winding is at first considered as divided in two parts, as if there were two distinct windings, an upper and a lower one, which will be series connected in the end to form the final machine winding. The upper part comprises those conductors with a current I (non-split), while the lower part by the sub-conductors where the current is $I/2$. For this example, n_{sub} = 2 for each equivalent conductor, hence four layers, determining two equivalent conductors, belonging to the lower part. To achieve this, it is necessary that every resulting machine parallel path is formed by the series connection of a single path of the upper winding (UW1) and the parallel connection of two paths of the lower winding, which, for the sake of clarity, will be called sub-paths (LW1.1 and LW1.2). In other words, to form an equivalent path of

the lower winding, at least two parallel sub-paths are needed which results in a limitation of the maximum number of achievable machine parallel paths N_{aa}.

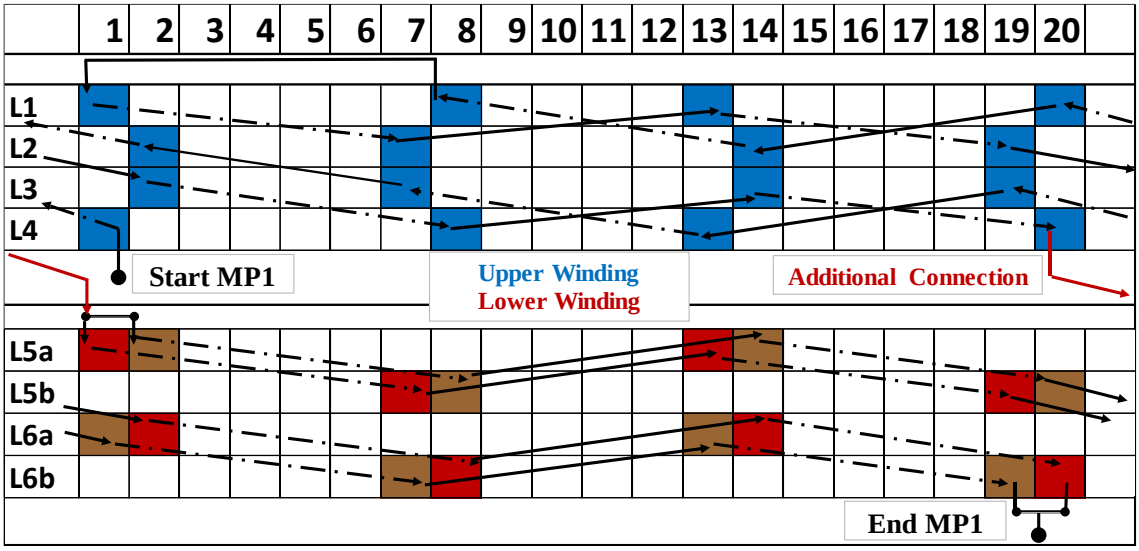

Fig. 23. Possible diagram connection for N6 configuration. The dotted lines refer to the welding side. One machine parallel path is displayed (MP1). UW1 (blue) is series connected to the parallel connection of LW1.1 (red) and LW1.2 (brown).

The number of sub-paths corresponds to the number of sub-conductors for each equivalent conductors n_{sub}. In this way the current coming from the upper winding is halved once it has reached the lower one. This concept is also summarized in fig. 24, where the upper path UW1 is series connected with the parallel connection of the sub-paths LW1.1 and LW.12. It must be noticed that with the proposed approach UW1 and UW2 (which comprises the remaining layers of the upper part) have the same impedance, as well as LW1.1, LW1.2, L2.1 and LW2.2 share the same impedance. Thus, the resulting machine paths (MP1 and MP2) have the same impedance as well, permitting to avoid potential current unbalances. Regarding the realization of the connections and transpositions of the two "distinct" windings, the already known rules illustrated in [20][21] can be adopted. The main difference is that these rules should be applied to the upper and lower windings separately, as shown in Fig. 23. At this point, the approach can be generalized for different numbers of layers and sub-conductors. According to [20], the maximum number of parallel paths N_{aa_u} for the upper winding is as in (17), where n_{L_u} is the number of the upper winding layers, pp the pole pairs, q the number of slots per pole per phase, N_{s_u} the minimum number of series connected turns. In (18), the expression for N_{s_u} is shown, where LMC is the least common multiple.

$$N_{aa\_u} = \frac{n_{L\_u} \cdot pp \cdot q}{N_{s\_u}} \qquad (17)$$

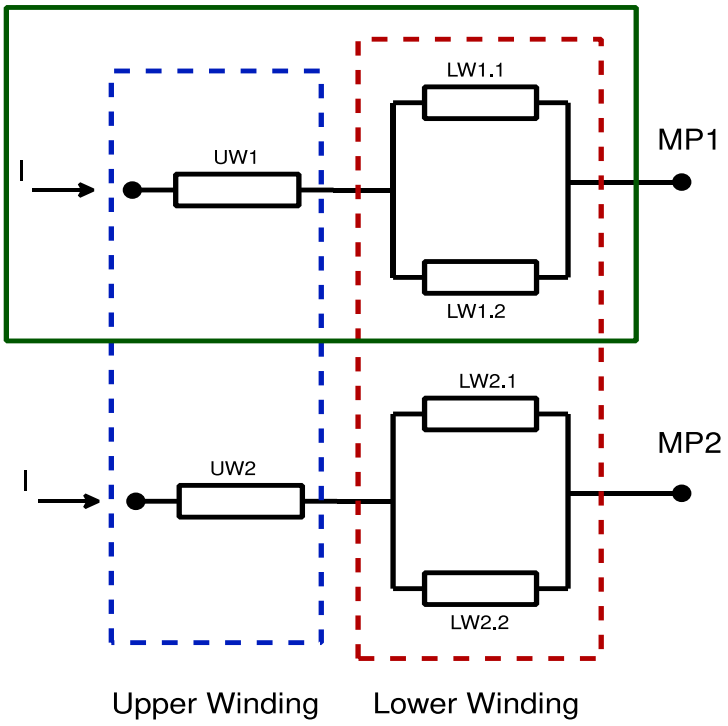

Fig. 24. Upper and lower winding connection scheme. The first machine parallel path (MP1), highlighted in green, is represented in fig. 23.

$$N_{s\_u} = LCM(\frac{ppn_{Lu}, q}{2}) \qquad (18)$$

For the lower winding, (19)-(21) can be written, where N_{aa_L} is the maximum number of parallel paths, N_{s_L} is the minimum number of series connected turns which can be calculated according to (18), n_{L_L} is the number of layers and n_{eq_L} is the number of equivalent slot conductors.

$$N_{aa\_L} = \frac{n_{L\_L} ppq}{N_{s\_L} n_{sub}} \qquad (19)$$

$$n_{eq\_L} = \frac{n_{L\_L}}{n_{sub}} \qquad (20)$$

$$n_{eq\_L}, N_{aa\_L} = integer. \qquad (21)$$

The condition expressed in (21) should be valid also when a lower number of parallel paths is chosen. Finally, the maximum number of achievable machine parallel paths for the entire winding N_{aa_seg}, which is usually equal to N_{aa_L}, is as in (22).

$$N_{aa\_seg} = GCD(N_{aa\_u}, N_{aa\_L}) \qquad (22)$$

2.3.7 WELDING SPOTS

During the simulations, the welding resistances are often overlooked as their estimation is a complex task. However, for a better estimation of the winding Joule losses, knowing the number of the welding spots and their average resistance value could be useful. In a segmented HW their number is expected to be slightly higher than in a conventional winding. The following formulations aim at estimating their number for both a conventional and a segmented HW adopting the connections topologies and rules described in [20]. The provided formulas could give a number which differs of a few units from a real machine, since the total number of welding spots can depend also on the number and type of adopted bus bars, which are not considered in this study. Considering only a resultant machine winding path, the number of welding spots depends on the number of hairpins N_{hp} and single pins (half hairpin). Since for each resulting path there should be one starting and one ending pin, and considering that one elementary hairpin occupies two slot layers, the total number of welding spots per path is $N_{ws} = N_{hp} + 1$, while the number of hairpins is given by (23), where p is the pole number, n_L the number of layers and N_a the machine parallel paths. At this point N_{ws} can be written as in (24).

$$N_{hp} = \left(\frac{pqn_L}{N_a} - 2\right)/2 \qquad (23)$$

$$N_{ws} = \frac{pqn_L}{2N_a} \qquad (24)$$

N_{ws} refers to one machine path only, thus, to obtain the total number of welding spots, it has to be multiplied by the number of parallel paths. Therefore, some additional welding spots should be considered for the connection of the starting and ending terminals of each path. When the bus bars are not considered, $N_a - 1$ additional welding spots are needed for each side, for a total of $2N_a - 2$. The total number of welding spots is then provided by (25).

$$N_{ws\_tot} = \frac{pqn_L}{2} + 2(N_a - 1) \qquad (25)$$

The same approach can be adopted for a segmented winding machine, with the only difference that two separate windings can be considered at first, which are then connected. As per the classical HW layout, the number of welding points is first estimated for a single machine parallel path. For both the upper and the lower windings, (24) can be adopted to estimate the number of welding spots for each path or sub-path, with the only difference that n_L is replaced respectively by the number of layers of the upper winding n_{Lu} and the number of layers n_{LL} of the lower winding. Since also the sub-paths' terminals of the

lower windings need to be welded and that their number is n_{sub} for each machine parallel path, the number of welding points for the lower winding is as reported in (26).

$$N_{ws\_L} = \frac{pqn_{LL}}{2N_a} + 2(n_{sub} - 1) \qquad (26)$$

N_{ws_L} is then summed to the number of welding points of the upper part and an additional welding should be considered for their connection, thus (27) is obtained, where N_{ws_seg} is the number of welding points for a single machine path (for example MP1, see fig. 23) of a segmented winding machine. To obtain the number of welding spots for the entire machine, (27) should be multiplied by N_a and then $2N_a - 2$ should be summed to it, as for (24). After a few simple steps, the total number $N_{ws\_seg\_tot}$ is obtained as in (28). The additional welding points of a segmented HW having $n_{sub} \geq 2$ and the same number of slots, poles and layers of a classical configuration, is provided by (29) subtracting (25) to (28).

$$N_{ws\_seg} = \frac{pqn_{Lu}}{2N_a} + \frac{pqn_{LL}}{2N_a} + 2(n_{sub} - 1) + 1 \qquad (27)$$

$$N_{ws\_seg\_tot} = \frac{pqn_{L}}{2} + N_a(2n_{sub} + 1) - 2 \qquad (28)$$

$$N_{ws\_add} = N_a(2n_{sub} - 1) \qquad (29)$$

Considering the above formulations, it is evident that increasing the number of parallel paths and the number of sub-conductors for each equivalent slot conductors leads to a higher number of welding points. However, if $n_{sub} = 2$ as suggested in the previous sections, the additional welding points are equal to $3N_a$. For example, for a winding having two machine parallel paths, this means six additional welding spots, which does not significantly affect the benefit achieved in terms of Joule losses reduction, as well as no further complications are added to the manufacturing process.

2.3.8 CONCLUSION

The analysis on the segmented hairpin topology was largely extended compared to the available literature, in which only some potentials of this unconventional winding layout were illustrated [25].

An analytical formulation updated for segmented HWs was developed. This model was first derived and then validated against FE simulations and experimental measurements carried out on a purposely-built motorette.

It was also shown that the segmented topology can provide significant reduction of the winding Joule losses both when the same number of layers or the same number of

equivalent conductors as the classical configuration are adopted. It was proven that a proper choice of the sub-conductor radial dimension is needed to guarantee a proper performance improvement, otherwise the segmented layout can lead to absent or negligible benefits. In particular, it is recommended to select a radial dimension close to 1 mm for copper conductors, which can guarantee significant Joule losses reductions up to 1.5 kHz.

The last part of this section aimed at providing guidelines and recommendations for the optimal design of this unconventional HW type, developing also a general estimation of the number of extra welding spots needed.

2.4 FINAL CONSIDERATIONS ON CHAPTER 2

Chapter 2 has addressed different aspects related to the theory, the state-of-the-art and the design of HWs. The classical theoretical model has been first presented and has proved to be sufficiently reliable for preliminary studies and feasibility analyses. Then, this analytical approach has been used to investigate on the possibility to adopt different materials than copper, showing interesting and promising results in terms of applicability of aluminium HWs. Finally, the analytical model has been updated to analyse the recent segmented HW, with practical recommendations and guidelines being also provided. The next chapter will address some other practical implementations of HWs, but with more specific boundaries and considering the traction sector as the main application. In particular, the possibility of implementing HWs in a multi-three-phase context will be detailed.

3. MULTI THREE-PHASE HAIRPIN WINDINGS

When the main aim is to increase torque density, efficiency and reliability of the system, the simultaneous adoption of technologies/configurations which can go in the same direction is a possibility which needs to be investigated. In this chapter, the adoption of HWs together with the multi-three-phase layout is investigated, as a means to further increase the torque density of the electrical machine, but also trying to improve other aspects of the electrical drive.

3.1 OVERVIEW ON MULTI-PHASE AND MULTI-THREE-PHASE MACHINES

Multi-phase machines can be an interesting alternative to conventional three-phase machines for many applications, while they can become mandatory for high power applications (in the order of MW), such us marine propulsion [35]-[37] or oil and gas industry extraction [38], where the use of three-phase VSIs is not possible due to the employment of large supplying currents. However, they can be used also in other fields, such as automotive and aerospace applications, where a high fault tolerance is needed [39]. Basically, multi-phase machines are electrical machines with an arbitrary number of phases $m > 3$. However, for the majority of them, m is five, seven or a multiple of three. The latter case often refers to the so called multi-three-phase machines, where the stator winding layout is composed by at least two separated star connected three-phase windings. For this reason, these machines are also known as multi-star (assuming a star connection) machines, but even multi-m-phase machines are possible. Being composed by a certain number of three-phase windings, they can be fed by the same number of three-phase VSIs, avoiding the need of a specific m phase inverter.

The winding design of multi-phase machines is not really more complex than a standard three-phase winding layout, however they need a higher number of inverter legs leading to additional costs and a more complex control strategy, which is the main issue. However, they can provide many benefits, some of them depending on the winding arrangement. The main advantages compared to standard three-phase machines are a higher fault tolerance operation, higher torque density, lower torque ripple, lower per phase current with the same output power, lower converter DC bus current ripple and more degrees of freedom for the control strategy [35]-[40].

3.1.1 General Design Aspects

A standard multi-phase winding design can be realized following the same principles for a classical three phase winding [40]. Being *m* the number of phases and *Q* the number of stator slots, each phase has to cover the same number of slots which is *Q/m* or, in other words, each phase has to extend over *360/m* mechanical degrees. The star of slot (SOS) method [38] can be used for the realization of a balanced winding. The more common standard multi-phase machines are the five and seven-phase, but in some cases also eleven phases are used.

However, for a multi-star machine, (from now multi-star and multi-three phase will be used as synonyms) the design tends to follow a different path. The realization can start from a standard three-phase winding arrangement, then each phase is split in *S* sub-phases or sub-belts which are separately star connected, resulting in a total of *3*S* total phases. Indeed, the final number of three-phase windings, or stars, composing the stator winding is equal to *S*. An important aspect of multi-star machines is that, unlike standard m-phase machines, the different stars have not any physical connection between them, so there will be *S* separated neutral points. Since their design can start from the splitting of a conventional three-phase layout, multi-star machines are also called split-phase machines. Another critical aspect is the electrical phase shift between the stars. If the phase shift is 0 or $2\pi/m$, there will be a symmetrical winding, as in fig. 25, otherwise the machine will be a multi-star asymmetrical one. From and electromagnetic point of view the machine with a zero phase shift is the same of a three-phase machine, since the rotating fields of the different three phase stars are completely superimposable, while the use of a certain phase shift can lead to some advantages, such as the cancelation of certain space harmonics. There is not always a unique solution to arrange a multi-star machine from a specific three-phase layout. One solution is to exploit the periodicities in the machine as in the case of sectored machines [41]. If p is the number of poles, the periodicity t of the machine is as in (30).

$$t = GCD\ (Q, p/2) \tag{30}$$

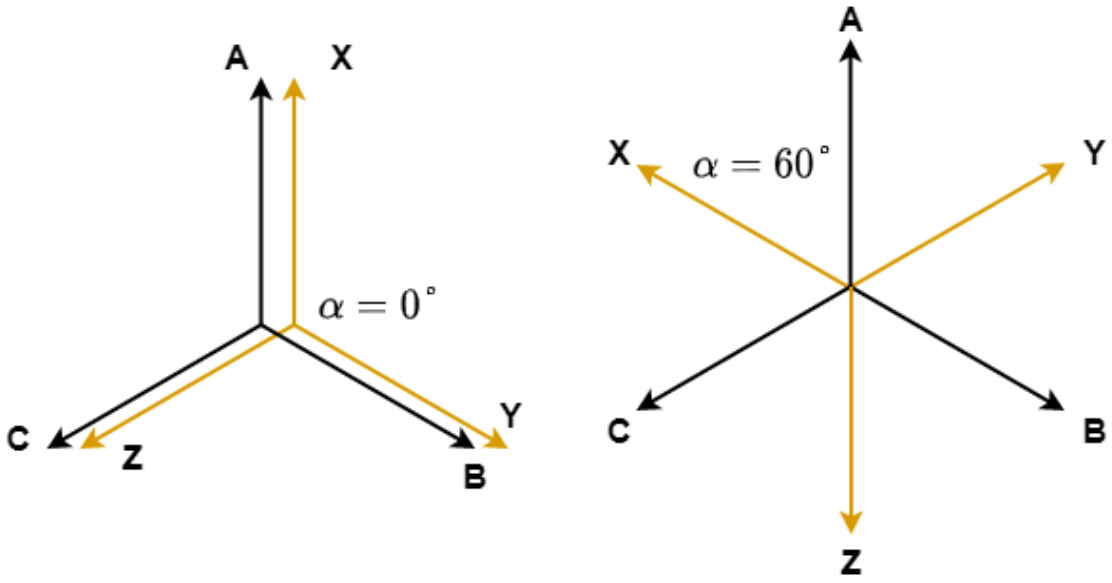

Fig. 25. Example of stars corresponding to symmetrical dual-three-phase windings. The electrical phase shift between the sets of three-phase windings is α.

It is possible to rearrange the winding into *t*, or integer submultiple, different stars, one for each sector, where one sector corresponds to one periodicity (or integer submultiple). With this solution there will be a zero-phase shift between the stars, so some possible advantages of multi-star machines cannot be achieved as it will be underlined later. In [40] the machine has *Q=18* and *p=6*, so *t=3*. Therefore, the only sectored machine which can be derived is a triple-three phase one.

Another possible solution to design a multi-star machine is to split the series connected coils per phase per periodicity, or in other words, the number of series connected coils per basic machine layout. The basic machine layout is composed by the first *Q/t* slots and *p/t* poles. For a machine with *t = 1*, the basic layout corresponds to the machine itself. If *N* is the number of considered series connected coils, the number of sub-three-phase windings (stars, assuming a star connection) which can be obtained with this method is *S = N* (or integer submultiples). It is clear that if *N = 1*, so for each periodicity the starting three-phase machine has only one coil per phase, it is not possible to obtain a multi-three phase machine. If *N* is a prime number the only one solution is given by *S = N*, so if *N = 3* a triple-three phase (TT) can be obtained, while if N = 2 a dual three-phase (DT) can be obtained.

DT machines are maybe the most common multi-three phase machines for their relatively simple design, the higher performances compared to the three phase counterparts and their higher fault tolerance capability [42]-[48]. Many studies have been done also for the DT fractional slot concentrated winding (FSCW) machines [42], [44], [47], [48] for their

capability of improving torque density and reducing the magneto-motive force MMF harmonic content. In [49] a feasibility analysis on DT FSCW machines is done basing on the SOS theory [37]. A balanced DT machine can be done if (31) and (32) are satisfied, respectively for double layer and single layer windings.

$$Q/2t = even \tag{31}$$

$$Q/4t = even \tag{32}$$

3.1.2 MAGNETO-MOTIVE-FORCE

One of the main aspects related to the research and employment of multi-phase machines is the harmonic content of their MMF. Multi-phase machines tend to have a lower MMF space harmonic content which determines lower rotor losses and lower torque ripple both for five phase machines (or more) than for multi-three-phase machines [50]-[52]. The cancelation of some space harmonics, which are present in three-phase counterpart, is achieved for all the standard multi-phase machines and for all the multi-three-phase machines for which there is an electrical shift between the different sets of three-phase windings. The shift determines which space harmonics are eliminated and can influence also other aspects as underlined in [42], such as the d-axis inductance L_d and the mutual inductance between the different sets of windings M. However, in [50], it is shown that the reduction of rotor losses with the employment of a number of phase $m > 3$ cannot be much high, since the majority of the aforementioned losses are due to the so called slot harmonics, which depend only on slot/pole combination. So, in order to minimize the rotor losses, both the winding arrangement and the slot/pole combination need to be considered. The slot harmonics order v can be predicted with the following expression:

$$v = kQ \mp \frac{p}{2} \tag{33}$$

Where k is an integer value. The most dangerous slot harmonics are the subharmonics which are a typical characteristic of FSCW and, generally, all the harmonics whose order is near the fundamental one, so the low order harmonics. The rotor losses are in fact dependant on the relative speed of the harmonics with respect to the rotor speed. Low order harmonics are the fastest and can be seen with a relative HF. The relative speed ω_r of the *v-the* harmonic is

$$\omega_r = \frac{2\pi f}{sign(v)\cdot v} - \frac{2\pi f}{p/2} \quad (34)$$

where sign(v) considers the rotational direction (forward or backward) of the considered harmonic.

Another important aspect related to the multi-phase-machine MMF harmonics is the possibility of increasing the fundamental winding factor k_{w1}, allowing for an increase of the average torque [53]. Hence, for multi-three phase machines, the phase shift is mandatory for winding factor maximization purposes. Keeping the different stars in phase do not enable this further benefit. However, the supply through inverters provides many harmonic currents. The fundamental winding factor refers to the synchronous space harmonic generated by a sinusoidal current, or, in other words, by the first current harmonic when the supply is provided by a VSI. In a three-phase machine there is only one synchronous space harmonic and it is generated by the first current harmonic. For multi-phase machines other synchronous space harmonics can be generated in addition to the fundamental one with the use of some higher order current harmonics. Each current harmonic determines a set of space harmonics, hence the MMF harmonic content has a dependence on both time and harmonic order [54]. The air gap magnetic field generated by the stator winding, if slot, saturation and end effects are neglected, contains the same MMF harmonics and its vector potential A can be expressed as in (35).

$$A = \sum_{n=-\infty}^{\infty} \sum_{k=-\infty}^{\infty} A_{n,k} e^{j(k\phi - n\omega_m t)} \quad (35)$$

In (35), ω_m is the mechanical speed of the machine, ϕ is the angular coordinate, n is the time harmonic order and k is the spatial harmonic order. Hence the rotating field components are function of both n and k. The rotational speed of each (n,k) component is reported in (36), so it depends on the ratio n/k and the resulting $\omega_{n,k}$ can have a positive or negative sign (can rotate forward or backward).

$$\omega_{n,k} = \frac{n}{k}\omega_m \quad (36)$$

For n = 1 and k = 1 the rotating field component corresponds to the synchronous spatial harmonic produced by the first harmonic current (the fundamental) and has in fact a mechanical speed of ω_m. However when the ratio n/k = 1 the corresponding n,k component is synchronous too and therefore may be used for additional torque production. This concept is valid for every synchronous spatial harmonic that can be produced. However, as underlined in [54], only some combinations are associated to a coefficient $A_{n,k}$ different from zero, hence only some harmonic currents have a corresponding spatial harmonic of the same order (n = k) and their existence is related

also to the number of phases m. If m increases, a higher number of harmonics can be exploited, while for $m = 3$ only the first current harmonic can be used.

3.1.2.1 EXAMPLE OF HARMONICS CANCELLATION

Considering for simplicity a DT machine with a certain electrical space shift φ between the two sets of windings, the final MMF harmonic content of the six-phase winding is given by the sum of all the harmonics of the two three-phase windings. Each rotating three-phase harmonic of electrical order υ produced by the first winding, which is taken as reference for the phase shift, is equal to:

$$f_{I,\upsilon} = a_\upsilon \cos(\omega t \pm \upsilon \alpha_e) \qquad (37)$$

where a_υ is the amplitude of the υ harmonic, $\alpha_e = pp\alpha$ is the angular coordinate in electrical radians (α is the mechanical coordinate in radians) and ω is the pulsation of the feeding current. The ± sign determines if the harmonic rotates clockwise (+) or counter-clockwise (-). For $\upsilon = 1$, (37) returns the typical expression of the three-phase fundamental rotating wave. The second set has an electrical phase shift of φ both in time and space which means that the axes of two adjacent phases of the different sets have a phase shift of φ electrical radians in space and the feeding currents of the same phases have a time shift to which corresponds a phase displacement of φ electrical radians. So, each MMF harmonic of the second set can be written as:

$$f_{II,\upsilon} = a_\upsilon \cos[(\omega t - \varphi) \pm \upsilon(\alpha_e - \varphi)] \qquad (38)$$

The υ harmonic of the DT winding is:

$$f_\upsilon = f_{I,\upsilon} + f_{II,\upsilon} \qquad (39)$$

Hence if $f_{I,\upsilon}$ and $f_{II,\upsilon}$ are in phase, the υ harmonic remains unchanged with respect to the three-phase winding. Otherwise the harmonic decreases or is cancelled. It is immediate to understand that depending on the phase shift φ some harmonics can be eliminated. For example, with a phase shift of $\pi/6$ the 5th and the 7th harmonics can be cancelled. In fact, (38), for $\upsilon = 5$, is equal to (40), while it is equal to (41) if $\upsilon = 7$ (the 5th and 7th harmonic rotates in opposite directions). In both cases (39) is equal to 0 since (40) and (41) are in phase opposition with respect to (37). The results can be seen also in fig. 26, and fig. 27. where the MMF waveform for a three-phase and double three-phase with 30° of phase shift windings are illustrated, as well as the respective harmonic spectra. The six phase configuration does not present the 5th and 7th harmonics.

$$f_{II,v} = a_v \cos[\left(\omega t - \frac{\pi}{6}\right) + 5(\alpha_e - \frac{\pi}{6})] \qquad (40)$$

$$f_{II,v} = a_v \cos[\left(\omega t - \frac{\pi}{6}\right) - 7(\alpha_e - \frac{\pi}{6})] \qquad (41)$$

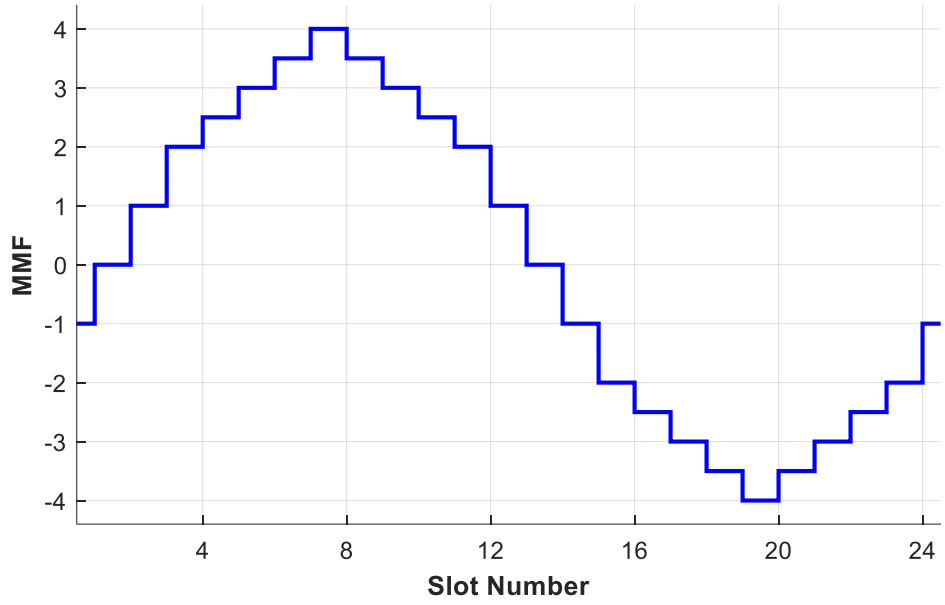

(a)

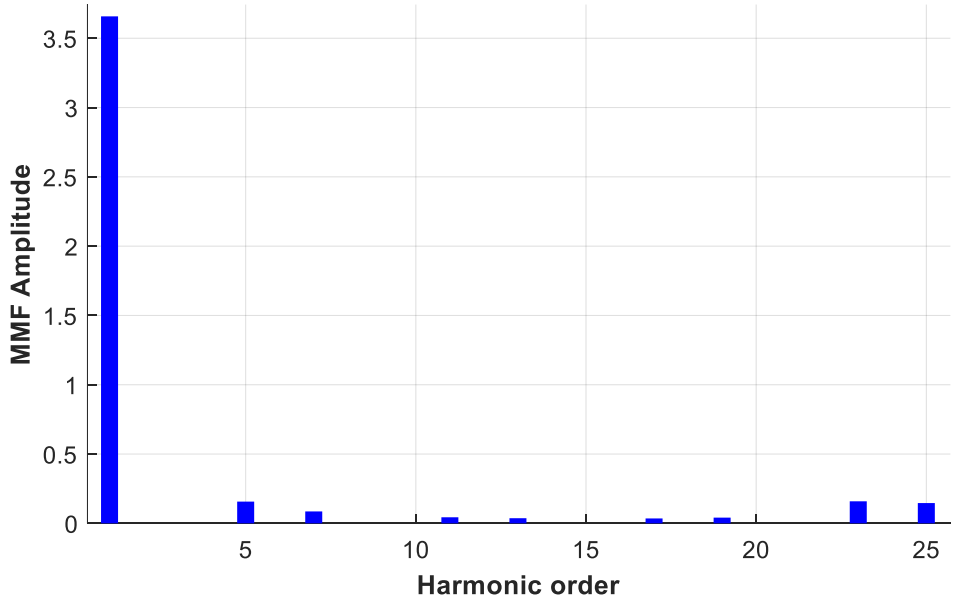

(b)

Fig. 26. Air gap MMF and spectrum for three-phase Q = 24, p = 2: (a) MMF; (b) MMF spectrum.

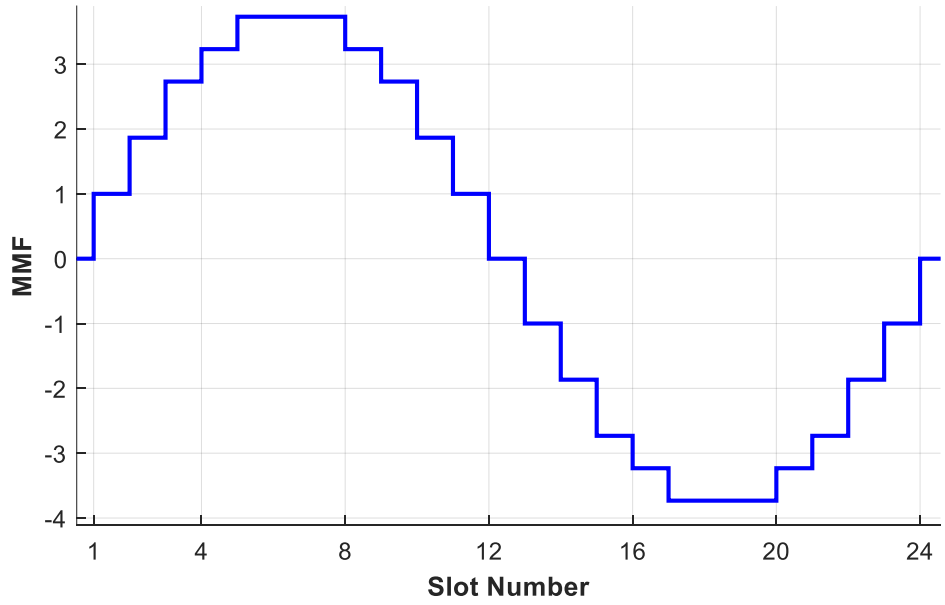

(a)

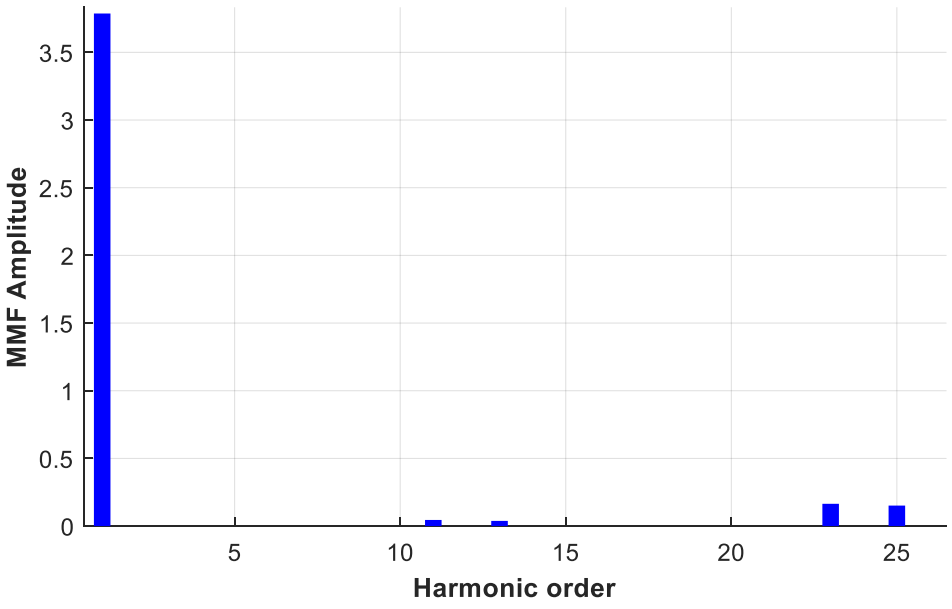

(b)

Fig. 27. Air gap MMF and spectrum for double three-phase Q = 24, p = 2 with 30° phase shift**:** (a) MMF; (b) MMF spectrum.

3.1.3 MAIN CHARACTERISTICS

Multi-phase machines are machines with a much higher redundancy compared to traditional three-phase counterparts and, for this reason, they present a series of peculiarities which allow performance and flexibility improvements as well as more control strategies, but also some additional issues may occur in some cases.

3.1.3.1 TORQUE ENHANCEMENT

As stated in the previous sections, multi-phase machines have a lower torque ripple with respect to their three-phase counterpart thanks to their lower MMF harmonic content which leads also to lower rotor losses. In addition, the possibility of increasing the fundamental winding factor allows to maximize the torque output for a given slot-pole combination. However, in some cases the torque can be further increased with a proper strategy. This is the case of the current harmonic injection (CHI) method, which has been addressed in some studies in order to maximize the torque density of the machine [36], [55], [56]. Basically, there are two main principles of exploiting the CHI. The first, which is the simplest and can be used in every machine, is to inject a higher order harmonic current, usually the 3rd, in order to be able to increase the fundamental harmonic current keeping constant the current peak value. The second principle is the aforementioned one in the previous section: the injected current harmonic/s is/are used to provide additional torque to that provided by the fundamental one. In addition, to use the n^{th} current harmonic, it is also necessary that the same harmonic order is present in the phase back electromotive force (BEMF). However, this principle cannot be applied to every machine. If the current harmonics employed for torque enhancement are zero sequence ones, such as the 3rd in multi-three-phase machines, a neutral connection for every winding set is needed. Otherwise no hardware changes are needed. For example, the 5th and 7th harmonics, don't need any zero sequence path to flow.

3.1.3.2 PHASE CURRENTS

The splitting of the feeding currents in more than three phases allows to reach higher powers without changing the power converters rating. On the other hand, the currents have to be compatible with the switching devices limits. Hence, the use of more than three phases is mandatory above certain powers. For the same reason, there is also the chance to decrease the power converters rating when the rated power is supposed to be constant, with respect to a three-phase system. When increasing the power of the drive, the switches have to carry higher currents, leading to a lower limit of the switching frequencies, which determines a higher current ripple. This aspect is crucial for high power applications, where the current ripple could reach significant values. Hence the splitting of the currents can have a further beneficial effect on torque ripple.

3.1.3.3 FAULT TOLERANCE

Multi-phase machines are often used for their capability of operating in faulty conditions. For multi-star machines, the easiest way to proceed when one or more phases of a specific winding set are subjected to a fault is to open the faulty winding and work with the remaining sets. As long as at least 3 phases (of the same winding set for a multi-three-phase machine) are safe, it is possible to operate with an independent control of current and flux, hence of torque and speed for every multi-phase machine. This procedure can be applied both for machine and for inverter faults. However, a huge part of the electrical drive faults are inverter faults. Hence the faulty inverter leg can be opened and the machine can work with the remaining m-1 phases [57], [58]. This certainly implies a more complex control strategy, but it allows a lower reduction of the overall performance.

3.1.3.4 CONTROL AND MODULATION TECHNIQUES

The main drawback related to the use of multi-phase machines is certainly the more complex control system due to the higher number of phases. However, the complexity of the control system is related also to the higher degrees of freedom which allow different strategies, from CHI to fault tolerant operations. From a hardware point of view, a standard m-phase machine requires an m-phase inverter, while the majority of the available inverters are three-phase ones. This disadvantage is partially overcome with the use of multi-star machines, which, thanks to their modularity, do not need specific m-phase inverters. However, the different winding sets have an inductive mutual coupling. In addition, these machines have lower phase inductances with respect to the three-phase counterparts, leading to lower impedance paths for undesirable current harmonics. The lower inductances, combined with the star couplings can trigger dangerous harmonic currents, in particular with VSI which use a standard PWM modulating technique [52]. These currents can be reduced with a specific design (higher phase leakage inductance), with the use of passive filters or with appropriate control strategy, which are computationally heavier than those utilized for three-phase systems.

The use of VSI inverters with standard PWM does not seem to exploit the best possible performance of multi-three phase machines. An interesting solution is provided in [41], where a sectored triple-star machine is controlled with a PWM strategy with carrier phase shift of 120° and 240° leading to a significant ripple reduction without increasing the computational burden. However, for both m-phase and multi-three-phase machines, the most common modulation technique is provided by the space vector PWM (SVPWM).

In particular, the most suitable strategy in terms of higher efficiency operation is the SVPWM with vector space decomposition (VSD) [40], [31]-[35]. The main aspect related to this strategy is the fact that, despite the total number of phases, there is only one frame for the electromechanical torque production, the α-β frame for a fixed reference, or the d-q frame for a rotating reference. The other frames are referred only to zero sequence harmonics and to other undesired harmonics, which can be controlled and minimized. The use of *S* neutral points for a *S*-three-phase machine decrease the order of the system from *m* to *m-S* [6], [59], [60].

3.2 Analysis on Multi-Three-Phase HWs: Possible Implementations

3.2.1 Initial Case Study

As vehicle to investigate multi 3-phase HWs in traction motors, a PM assisted synchronous reluctance machine is considered. Keeping the initial rotor design, i.e. an 8 poles rotor, and the main stator dimensions unaltered, two slot combinations are studied, i.e. 72 and 96 slots. The initial stator and rotor structure is the same as fig.6. A summary of the main machine parameters and requirements is provided in Table III.

Table III. Machine main parameters and minimum requirements

Machine Type	
PM-Assisted (NdFeB) SynRel	
Slot Combinations	
72	96
Rotor Poles	
8	
Speed [rpm]	***Torque [N.m]***
5000 (Base Minimum)	400
15000 (Max)	130
DC Link Bus Voltage [V]	
620 - 700	

Considering the limits of applicability of HWs, the focus is on the different multi 3-phase hairpin structures which can be adopted for both configurations. For each HW arrangement, all the simulation results are compared to their random-wound counterparts equipping stranded round conductors. In terms of modelling assumptions, the main differences between bar- and random-wound solutions are:

- The fill factor is assumed equal to 40% for the random arrangement, whereas an 80% fill factor is considered for the HW.
- AC losses are considered null for the random-wound windings, inherently meaning that each conductor comprises a high number of parallel strands which make the current distribution uniform within the considered frequency range. On the other hand, each hairpin leg is modelled as solid conductor using a suitable mesh density. This allows to take all the AC losses components into account.

3.2.2 FEASIBILITY ANALYSIS

3.2.2.1 CONVERTER RATING

From Table III it is possible to estimate within an acceptable accuracy the inverter power needed for a continuous operation of the drive. The required minimum torque is 400 Nm with a minimum constant torque speed limit of 5 krpm. Considering that the mechanical torque is always lower than the estimated electromagnetic torque due to additional losses and non-ideal behaviour of the materials, the 2D models are designed such that the electromagnetic torque is at least 10% higher than the required mechanical value, for a total of 440 Nm. Hence the output power P_{out} = 230 kW. Assuming for simplicity an efficiency of 97% for both the inverter and the electrical machine, and a power factor of 0.8, the phase current flowing in each device as a function of the phase voltage is straightforward to estimate. The switching device phase current corresponds also the electrical machine line current. In particular, it is interesting to estimate the phase current corresponding to the phase voltage limit (or vice versa), thus to the converter rated power. The maximum fundamental phase voltage is then directly linked to the DC bus voltage, depending on the adopted modulation technique. Currents and DC bus voltages are plotted in fig. 28 for different number of phases when the inverter uses a classical SVPWM in the linear region and operates in its rated conditions. It can be observed that for the system DC bus voltage, the required rated current to reach an active power of 230 kW is below 400 Arms also for the three-phase configuration, which is a high, but feasible value. Adopting a multi-three-phase configuration would allow lower current values, but also to increase the total drive power if requested.

The total power can be expressed through a theoretical infinite number of torque-speed combinations. However only certain combinations can meet the requirements. In the next

section the main available winding configurations will be considered as a mean to exploit these requirements.

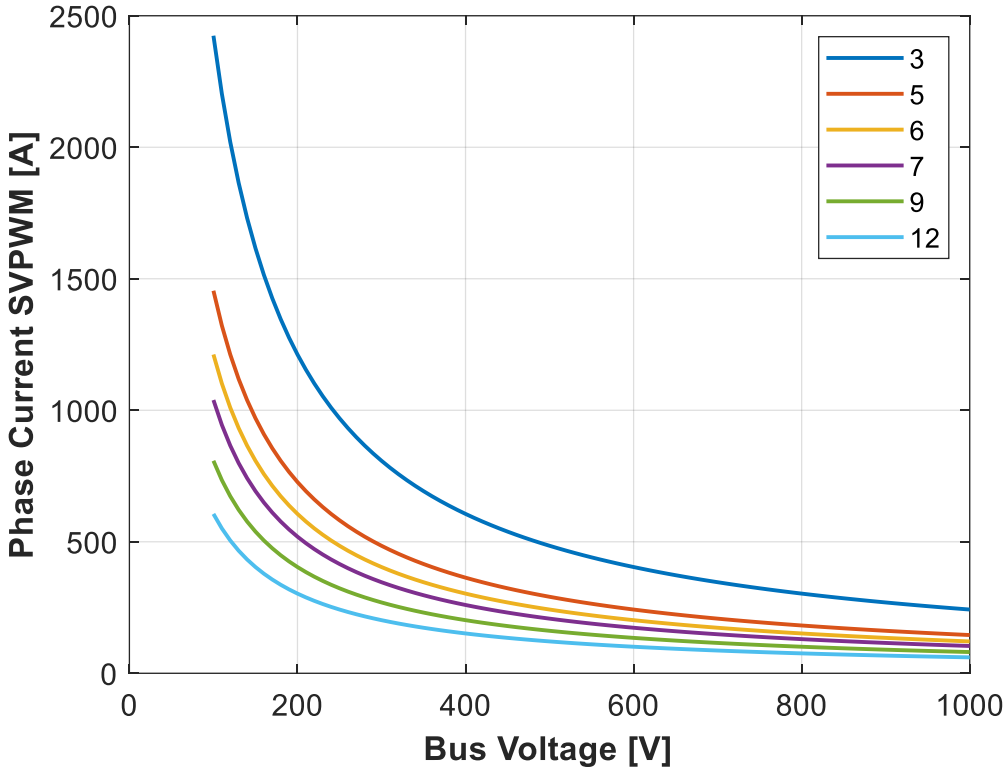

Fig. 28. Inverter phase current as a function of the DC bus voltage for different number of phases with SVPWM and a full use of the DC bus voltage for the linear modulating region.

3.2.2.2 STATOR CONFIGURATIONS

When designing an electrical machine for high-speed applications, the number of turns and parallel paths have to be carefully chosen to remain within the voltage limits. While for classical stranded conductors the number of degrees of freedom is quite high, more constraints are in place for machines with hairpin conductors. The important guidelines illustrated in [20], [22] need to be carefully followed for HWs, with a particular focus on the maximum number of parallel paths which allows a correct conductors' transposition. Only integral slot distributed windings are considered (ISDW) in the available literature. The minimum number of series connected turns N_s can be determined as in (42), while the maximum number of parallel paths N_{aa} which allows a correct transposition and uniform connections is calculated using (43).

$$N_s = LCM\left\{\frac{n_L pp}{2}, q\right\} \quad (42)$$

$$N_{aa} = \frac{ppqn_L}{N_s} \quad (43)$$

The examples shown in [20], [22] refer to 3-phase windings, however all the assumptions and considerations can be extended to multi 3-phase configurations. In fact, considering a balanced multi 3-phase ISDW, each 3-phase set is equally and evenly distributed along the stator circumference. The number of slots-per-pole-per-phase is lower but remains an integer, which is the main conditions to exploit correct connections, as it can be noticed in (42) and (43). Hence, the expressions reported in (42) and (43), can be applied separately to each 3-phase set.

Considering the 72 slots solution, in order to meet both the required performance and the voltage limit, for the 3-phase machine n_L is chosen equal to 6, while the number of effective parallel paths is $n_{pp} = 4$. According to (43), n_{pp} could be higher, but increasing the number of paths would increase the manufacturing complexity. A higher n_L could result in reduced AC losses, but it would not be applicable due to the voltage limit. In fact, when n_L = 8 or 10, n_{pp} is limited to 2. However, the 72 slots, 8 poles 3-phase winding can be converted only into a 9-phase one with three 3-phase sets having an electrical shift of 20°. The 6- and 12-phase solutions would not be feasible for the 72 slots configuration since q would no longer be an integer like in the 3-phase winding. With n_{pp} = 2, the number of series-connected turns of each phase is multiplied by 2/3 (if the same n_L is adopted), allowing a lower phase voltage although the number of parallel paths per phase is halved. Fig. 27 shows how to pass from a 3- to a 9-phase winding halving n_{pp}. On the other hand, always taking into account the manufacturing aspects, it could be also possible to rise n_L to 8 without exceeding the voltage constraints. A higher number of n_L would also allow for a lower phase current if the power was kept constant, so lower Joule losses would be expected. Table IV resumes the main differences between the 3- and 9-phase windings. N_t represents the number of series-connected turns for each parallel path of any phase. The winding factor refers to the fundamental harmonic, therefore the 9-phase machine is expected to have a higher torque. Here the 9-phase machine with $n_L = 6$ and $n_{pp} = 2$ is investigated since it can provide a better exploitation of the torque-speed characteristic. However, also the case with $n_L = 8$ is reported for the sake of comparison in terms of Joule losses.

Table IV. COMPARISON BETWEEN 3- AND 9-PHASE TOPOLOGIES FOR 72 STATOR SLOTS WITH HAIRPIN AND STRANDED ROUND CONDUCTORS

	Hairpin		***Random***	
Parameter	***3-phase***	***9-phase***	***3-phase***	***9-phase***
q	3	1	3	1
n_L	6	6	6	6
n_{pp}	4	2	4	2
N_t	18	12	18	12
Line Current [A_{rms}]	454.68	227.34	454.68	227.34
Number of Converters	1	3	1	3
Winding Factor	0.96	1	0.96	1

Table V. COMPARISON BETWEEN 3-, 6- AND 12-PHASE TOPOLOGIES FOR 96 STATOR SLOTS WITH HAIRPIN CONDUCTORS

	3-phase	***6-phase***	***12-phase***
q	4	2	1
n_L	6	6	6
n_{pp}	8	4	2
N_t	12	12	12
Line Current (A_{rms})	682	341	170.5
Number of converters	1	2	4
Winding Factor	0.957	0.99	1

In order to study a different number of 3-phase sets, the 96 slots configuration is exploited, where 6- and 12-phase winding arrangements are possible in addition to the conventional 3-phase one. If $n_L = 6$, the 3-phase solution would require 8 parallel paths per phase which could provide some challenges with respect to the end winding connections and conductors' transpositions. Therefore, the analysis on the 96 slots, 3-phase machine will not be provided. Transforming the 3-phase winding either into a 6- or a 12-phase layout permits reducing the number of parallel connections per phase to 4 or 2 respectively, without exceeding the voltage constraints. Table V summarises the main parameters of the possible solutions. The data for the random windings with stranded conductors are omitted in Table V since they are basically the same as the hairpin machines.

The windings with round, stranded conductors have fewer constraints in terms of conductors per slot and parallel paths. Therefore, to simplify and making the comparison fully fair, 6 equivalent stranded conductors per slot are considered for all the winding configurations.

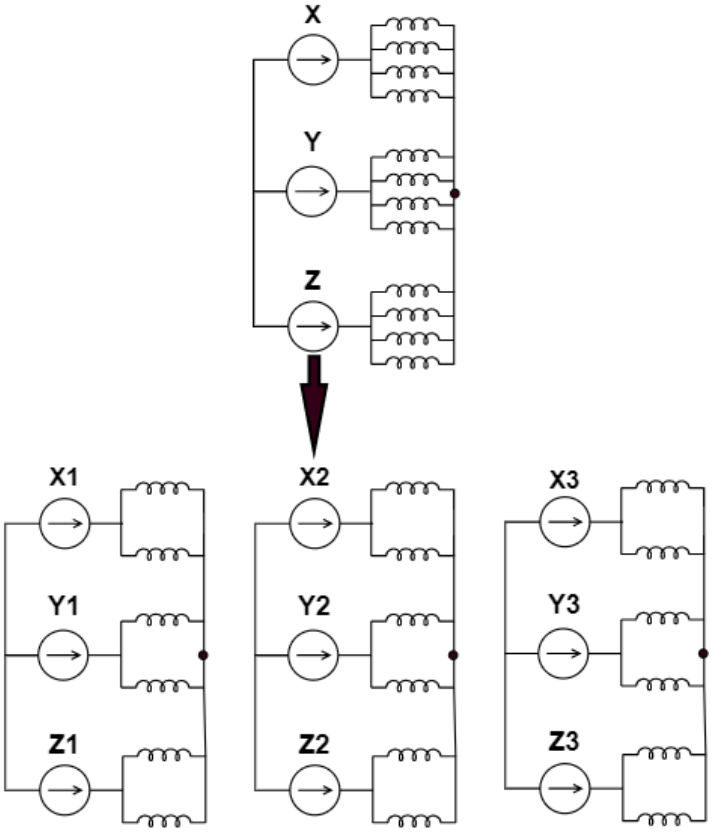

Fig. 29. Winding layouts examples for the 72 slots stator. Transformation of a 3-phase winding with 3 slots-per-pole-per-phase and 4 parallel paths per phase into a triple 3-phase configuration with 1 slot-per-pole-phase and 2 parallel paths per phase.

3.2.3 FE ANALYSIS

All the described machine topologies are analysed through FE models. All of these models implement the same identical materials for cores, windings and magnets. For a fixed slot number, the only difference from a 3-phase machine and its multi 3-phase counterpart consists in the winding arrangement so that the comparison can be easier and fairer. As the overall stator dimensions are kept unmodified when passing from random to HWs, the latter features a higher amount of copper than random layouts, due to their higher fill factor. The FE simulations are performed using MagNet software and exploiting its 2D modelling features, meaning that the end windings are neglected and the border effects cannot be computed. However, the DC component of the end winding losses can be calculated for all the cases using (44) for the estimation of the end winding length l_{ew} [32]. In (41), c_s is the average coil span. In [32], (44) is proposed for random windings, while front and back connections of hairpin conductors are typically shorter.

$$l_{ew} = 2.4c_s + 0.1\ [m] \tag{44}$$

In addition, always concerning the end winding losses, the effective value depends on the ratio R_{ac}/R_{dc} between AC and DC resistances. In the end region, the field strength is much lower than in the core, so the ratio R_{ac}/R_{dc} can be near to the unit depending on the machine geometries. If the flux density is sufficiently low, the ratio R_{ac}/R_{dc} would be near to 1 even at high operating frequencies (e.g. at ≈1 *kHz*), so an approximation of the end winding losses as purely DC would be acceptable. An analysis on the end winding losses in HWs will be provided in section 3.4. All the studied machines (see Tables IV and V) are modelled exploiting their periodicities. For both the 72 and 96 slots models, having both an 8 poles ISDW, there is a 1/8 odd periodicity, so 1/8 of each machine is analysed as shown in fig. 30, where the modelled angular sector of the 72 slots stator can be observed together with the mesh used.

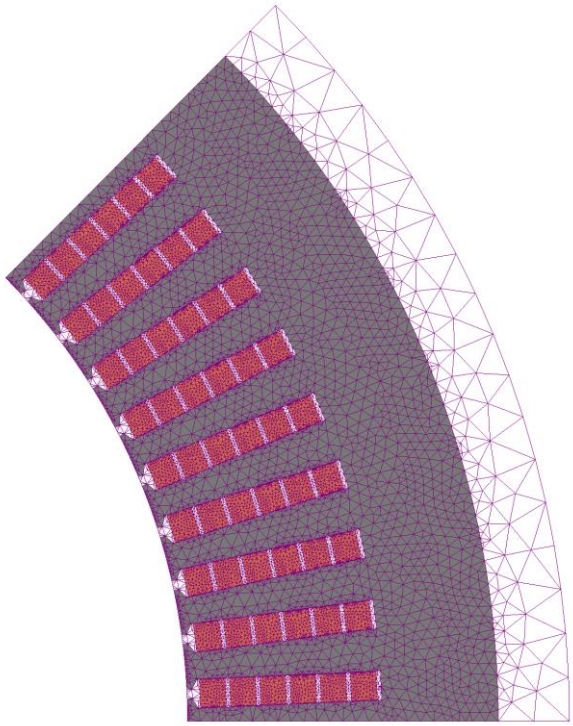

Fig. 30. 72 slots solid conductor 2D stator model with $n_L = 6$. The initial mesh is displayed.

The simulations are run using sinusoidal current sources feeding the stator phases. The torque-speed charts of each machine are estimated through the simulation at some relevant operating frequencies assuming a continuous power operation. All the results consider the fundamental harmonic voltage limit provided by a SVPWM scheme having a DC link voltage of 620 V. The value is computed through an FFT analysis of the induced voltages across the machine coils when the machine rated current is applied. Fig. 31 shows the estimated torque-speed characteristics for the HW machines. The 9-phase machine has a higher torque with respect to the 3-phase case and permits extending the

constant torque region thanks to the lower number of series-connected turns per phase. The 6- and 12-phase configurations for the 96 slots machines have very similar curves and torques. In fact, they feature almost the same fundamental winding factor and the same number of series-connected turns per phase.

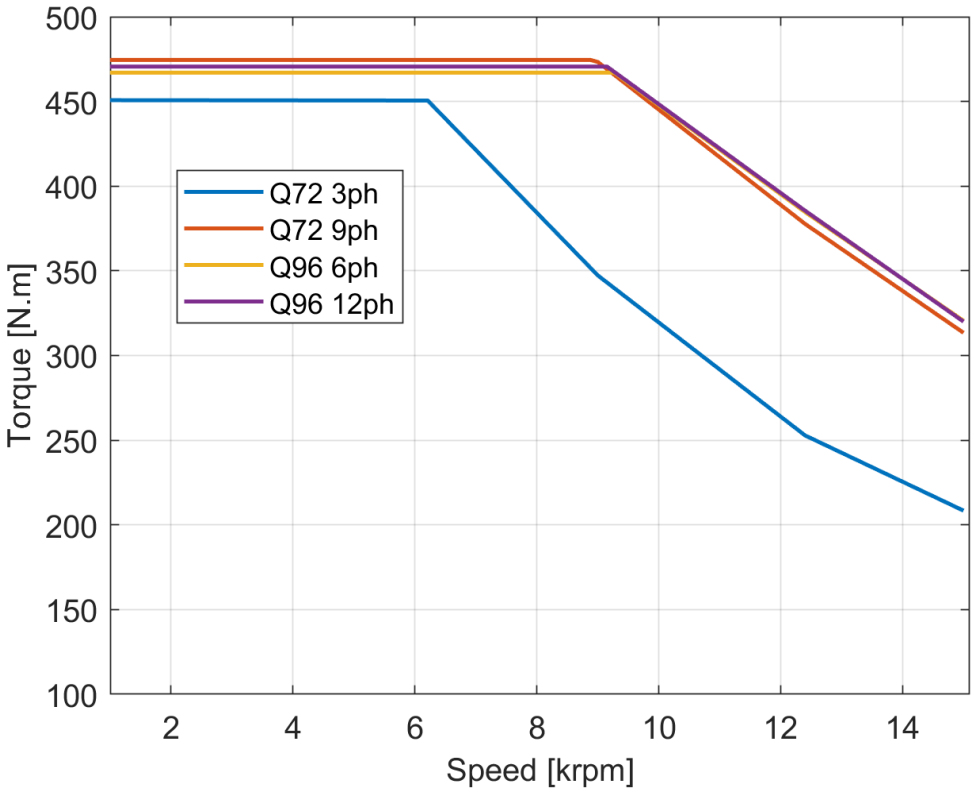

Fig. 31. Torque vs speed characteristic approximation for the different HW machines. Q refers to the number of slots.

Table VI and Table VII provide a summary in terms of losses for all the analysed machines at the base speed of 5000 rpm, also highlighting the comparison against the same machines equipped with random windings. Considering the active windings, the relevant losses in the 72 slots machines equipped with hairpins are higher than those in machines with random windings. This is an expected result as AC losses are present in the hairpin conductors at base speed already, as seen from the current density map shown in Fig. 32. For the 96 slots machines, at base speed, the active windings Joule losses are lower for the solid conductors compared to the stranded round ones, contrarily to what happens with the 72 slots case. This means that in the 96 slots machine the winding has a lower R_{ac}/R_{dc} ratio than the 72 slots case study. The lower ratio is caused by the smaller hairpin dimensions. However, including the DC component of the end winding losses, the total losses for the solid conductors result more similar to those of the stranded round ones for the 72 slots winding, while they are fairly lower for the 96 slots one. Basing on

the previously made considerations, the DC component at the speed of 5000 rpm (333.33 Hz) is predominant in the end region, so the contribution of the end winding losses is in favour of the HW. However, at higher operating frequencies, the Joule losses in hairpin conductors significantly increase and are more elevated than in the corresponding random winding machines, even considering the DC loss component of the end winding.

TABLE VI. SIMULATION RESULTS FOR THE 72 SLOT MODELS AT 5000 RPM

Simulation at 5 krpm	***3-phase***		***9-phase***	
	Hairpin	**Round**	**Hairpin**	**Random**
Torque [Nm]	451	452	475	477
Active Winding Losses [W]	4044	2361	4156	2361
End Winding Losses [W]	1194	2386	1194	2386
Total Winding Losses [W]	5238	4747	5350	4747
Magnet Joule Losses [W]	17.8	18.4	9.7	9.8
Rotor Iron Losses [W]	237	237	218	220
Stator Iron Losses [W]	2790	2730	2851	2780
Total Losses [W]	8283	7732	8428	7757
Efficiency [%]	96.6	96.8	96.7	97

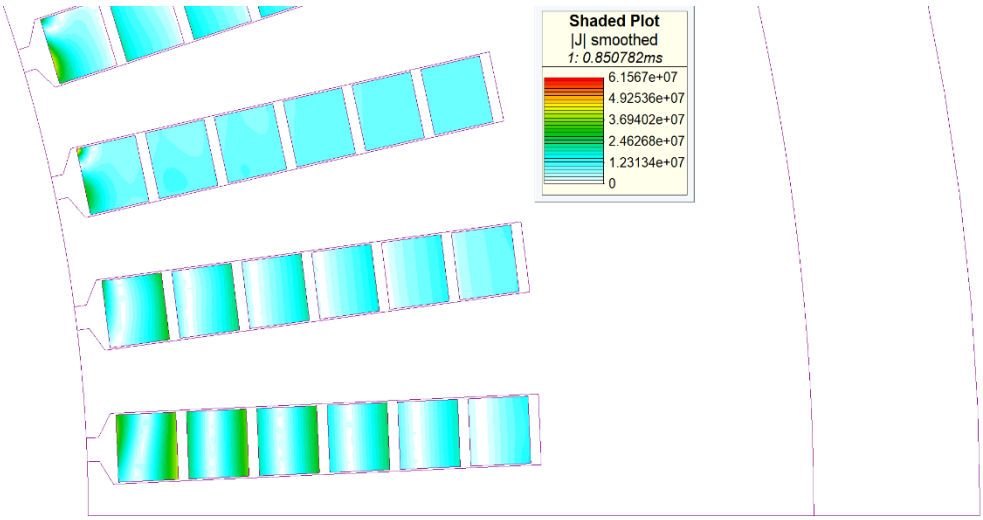

Fig. 32. Instantaneous current density at base speed for the 72 slots machine.

Table VII. SIMULATION RESULTS FOR THE 96 SLOT MODELS AT 5000 RPM

Simulation at 5 krpm	***6-phase***		***12-phase***	
	Hairpin	**Round**	**Hairpin**	**Random**
Torque [Nm]	466	467	471	472
Active Winding Losses [W]	2995	3987	3000	3987
End Winding Losses [W]	1986	3973	1986	3973
Total Winding Losses [W]	4980	7960	4986	7960
Magnet Joule Losses [W]	6.3	6.0	6.2	5.9
Rotor Iron Losses [W]	151	157	149	156
Stator Iron Losses [W]	2253	2216	2267	2230
Total Losses [W]	7390	10339	7408	10352
Efficiency [%]	97	95.9	97	95.9

3.3 DOUBLE THREE-PHASE HW - IMPROVED MODEL

Section 3.2 has been focused on the possibility to implement a multi-three-phase HW in order to improve the machine performances. The results linked to the torque enhancement and wider constant torque speed region have been promising, however the initial designs present too high AC winding Joule losses for a continuous operation in the rated condition. This sections presents an updated version of the double-three phase HW machine with a particular focus on the Joule losses reduction. Another important aspect is that the rotor structure is different from the previous one and cannot be further changed since this work is placed in the context of a European project in collaboration with the University of Nottingham, where the rotor has been designed. The following results should then be useful in preparation for the realization of a HW prototype. The main aspects related to the new model are the following:

- The number of total phases is equal to six. The configuration is a double three-phase with an electrical shift of 30°. With this configuration it is possible to exploit the main advantages of a multi-phase winding, but also the control strategy should be less complicated with respect to the 9 and 12 phase ones. Hence the total number of slots is fixed to 96.
- The number of slot conductors is six, with an asymmetric configuration. The 2 slot bottom conductors are thicker (2.8 x 4mm), in order to decrease the DC resistance, while the remaining four have a smaller radial dimension (2.8 x 1.8

mm), to limit the AC/DC ratio. The number of phase parallel paths is 4 as in the preliminary analysis.

The 2D FEM of the new machine structure can be seen in fig. 33.

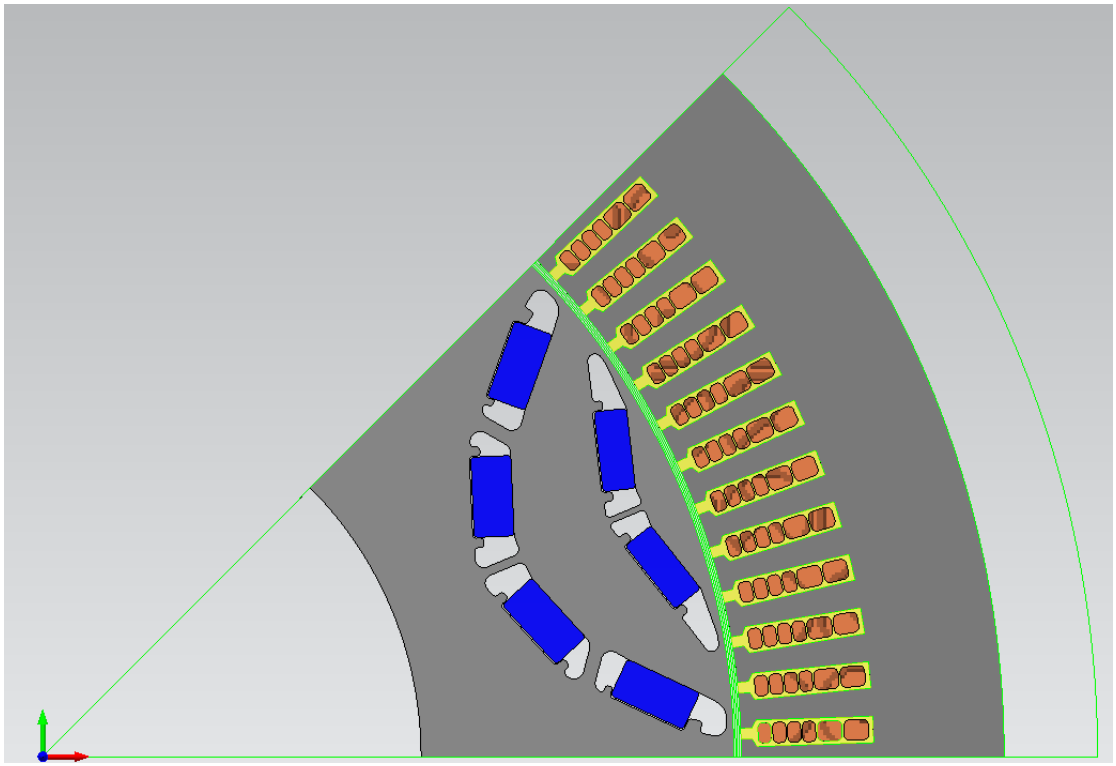

Fig. 33. 2D FEM of the new double three-phase machine.

3.3.1 Choice of the Conductors' dimensions

The choice of the conductors' dimensions is crucial to optimize the winding Joule losses. For this specific application the main aim is to decrease as much as possible the DC losses, but also having an AC/DC factor $K_r \leq 2$ for the maximum operating frequency (1 kHz). Ideally, for a specific frequency, every layer is linked to an optimal radial dimension, which minimizes the total losses and it is called critical conductor height. The ideal winding is then formed by a set of conductors having all different radial dimensions, where the first one from the slot bottom has the higher radial dimension, while the one closest to the air gap has the smaller one. Considering a conductor resistivity corresponding to the copper at 120°C, the critical conductor height as a function for the frequency for all the six layers of the considered machine is shown is fig. 34. It can be seen that in particular the first conductors would require really thick sections, while much attention should be paid for those close to the air gap. This plot can provide a first idea for a proper choice of the dimensions and can be also done for multiple sets of conductors, depending on the number of different hairpins that can be used.

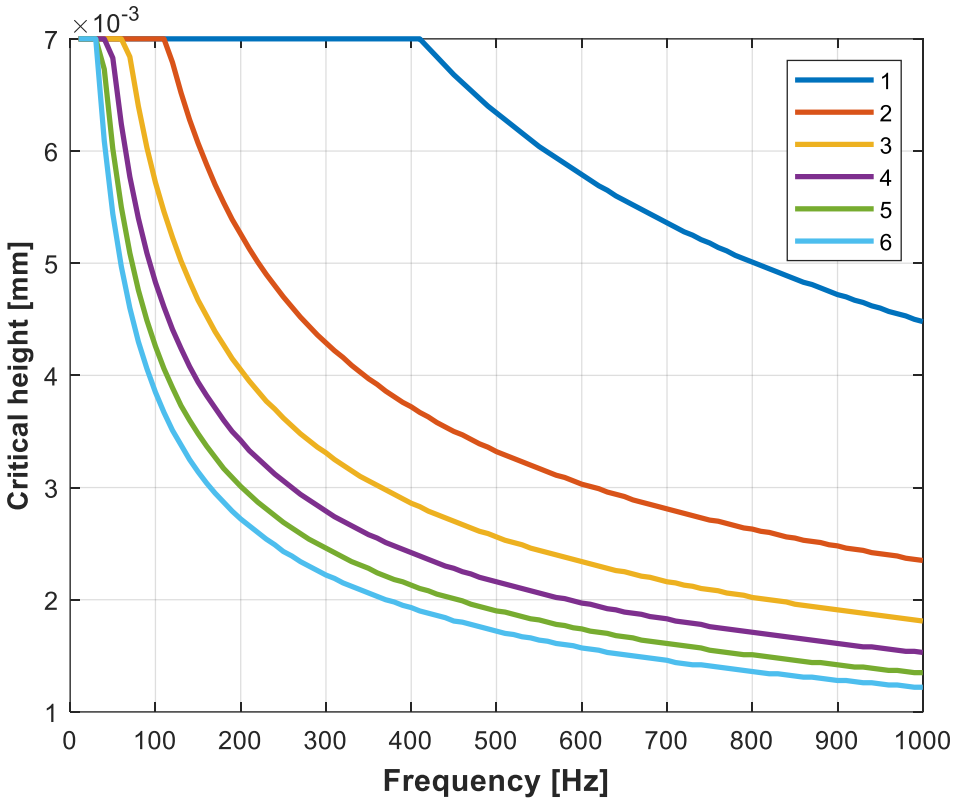

Fig. 34. Critical conductor eight as a function of frequency for the different winding layers.

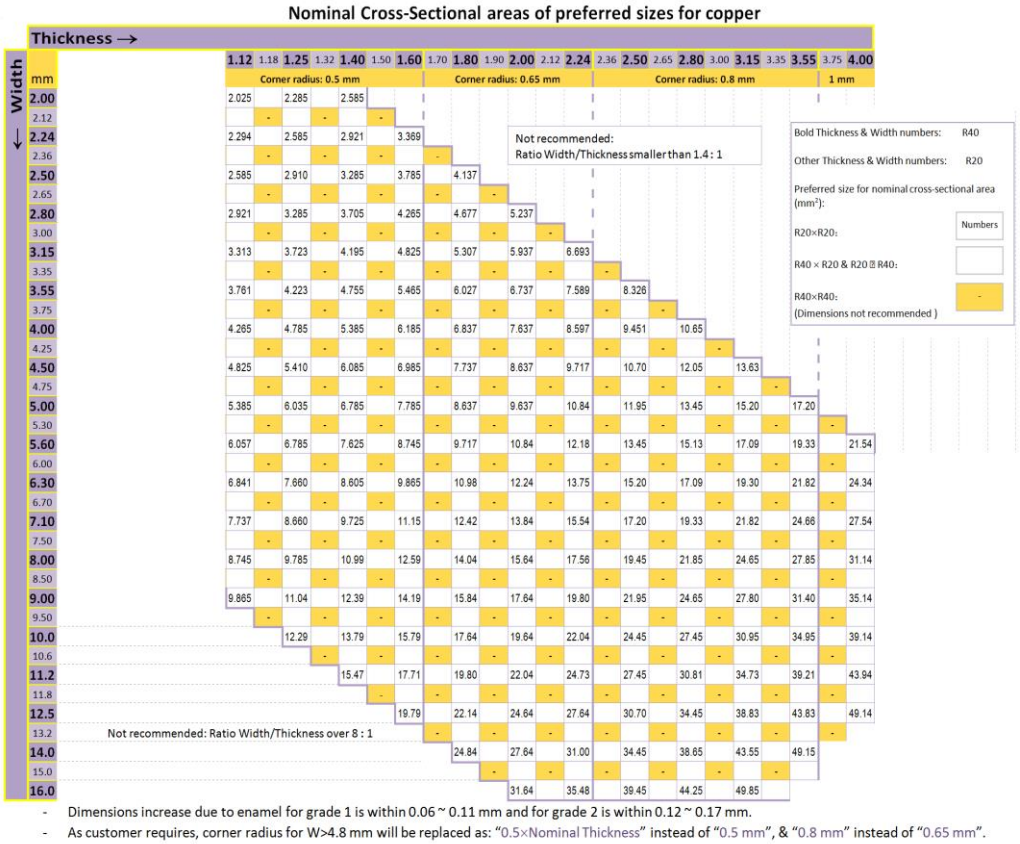

Fig. 35. Hairpin conductor feasible dimensions according to standard IEC 60317-0-2 [61].

However, when it comes to the selection of feasible dimensions also from a practical realization point of view, the number of constraints increase due to mechanical limits. Some combinations are preferable, while the adoption of others is not possible, according to the standard IEC 60317-0-2 [61], as it can be seen also in fig. 35. In particular, heights above 4 mm are not considered. Another additional rule is that the ratio *R* between the bigger and the smaller conductor dimension is $R \geq 1.4$. For this reason, being the conductor width 2.8 mm for the considered machine, the best feasible choice for the last conductor is adopting a height of 4 mm which can guarantee lower Joule losses for all the operating range with respect to lower radial dimensions. In order to perform the winding connections and transposition according to the rules illustrated in [20], [21], the second conductor should have the same identical dimensions, such that the first two slot layers are equally filled with a single hairpin topology. This would also help to further reduce the Joule losses for the first few hundreds of frequencies. The choice of the remaining conductors is quite straightforward and has the main aim to keep low the losses at the highest frequencies. The Joule losses can be evaluated for all the operating frequencies and different sets of radial dimensions and then, according to fig. 35, the closest height to the optimum solution can be selected. The selected height for the remaining conductors is then 1.8 mm and the comparison between the analytical Joule losses for the proposed winding and a classical configuration (all conductors have the same dimensions) having the same amount of copper, can be seen in fig. 36 when a current of 100 Arms flows in each conductor. The reduction of the Joule losses for the main part of the operating frequencies is important and the AC/DC factor is limited also at the maximum frequency. These improvements determine only a small increase in the DC losses with respect to the classical configuration, which is not an important issue since the thermal limits are not reached at the lowest speeds.

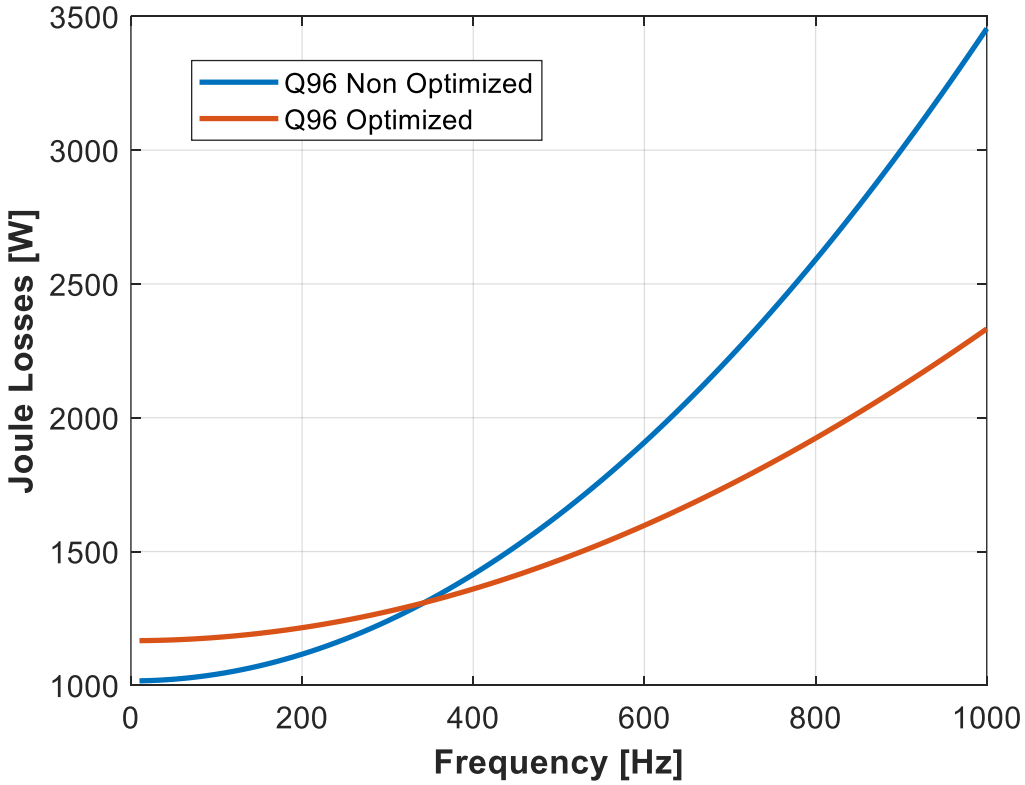

Fig. 36. Active length winding Joule losses: proposed winding vs classical configuration.

3.3.2 TORQUE-SPEED CHARACTERISTICS

The main characteristics of the new proposed machine are estimated using MagNet 2D through transient magnetic simulations. The main results can be found in fig. 37-39. Fig. 37 shows the torque as a function of the current vector angle with respect to the q-axis. The voltage limits have been calculated according to the maximum phase voltage which can be achieved in the linear region of a SVPWM modulation when the DC bus voltage is 700 V. Fig. 38 shows the induced phase voltage for the different current vector angles at 1 kHz, while the resulting torque-speed characteristics can be seen in fig. 39. All the results have been plotted also for five different loads (K_t), from low load (K_t = 0.2) to full rated load (K_t = 1). The machine is able to provide a torque of nearly 450 Nm at rated load and the base speed is around 9 krpm, far above the minimum requirement of 5 krpm. Regarding the components temperatures, a thermal map obtained with electromagnetic and thermal coupled simulation at the new base speed of 9 krpm is shown in fig. 40. The coupled simulation procedure works as follows and consists in an iterative process. Firstly, a transient magnetic simulation is run, with the initial temperature of each element hypothesized equal to 20 °C. The obtained losses are then utilized in the FE thermal machine model to run a static thermal simulation, in order to calculate the steady state

temperatures. Then the temperature of each component is put back into the magnetic model for another transient magnetic simulation with the new initial conditions and so on. The procedure is stopped when the temperature variation is below a certain threshold. In this case the procedure has been stopped when the variation was below 1%. The thermal model hypothesizes a cooling system with a stator water jacket having an equivalent heat transfer coefficient of 3000 W/T/m^2 and an average water temperature of 50 °C. Simulations show that the estimated temperatures are compatible with the involved materials and show that a full load continuous operation is still possible at 9 krpm.

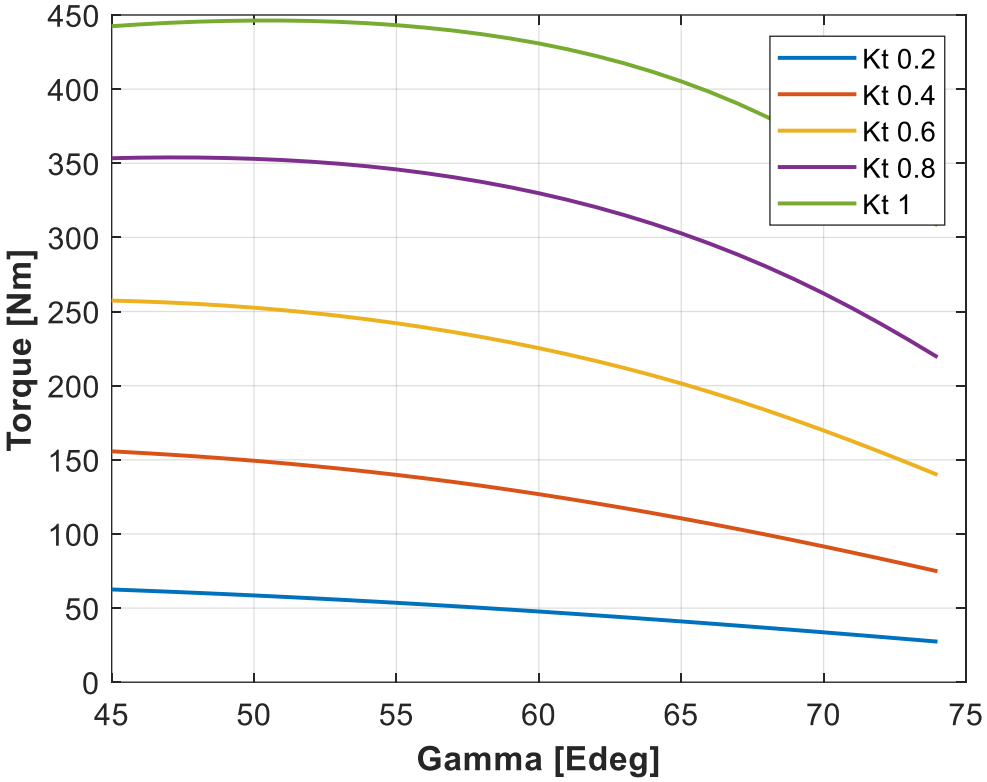

Fig. 37. Torque as a function of the electrical current vector angle.

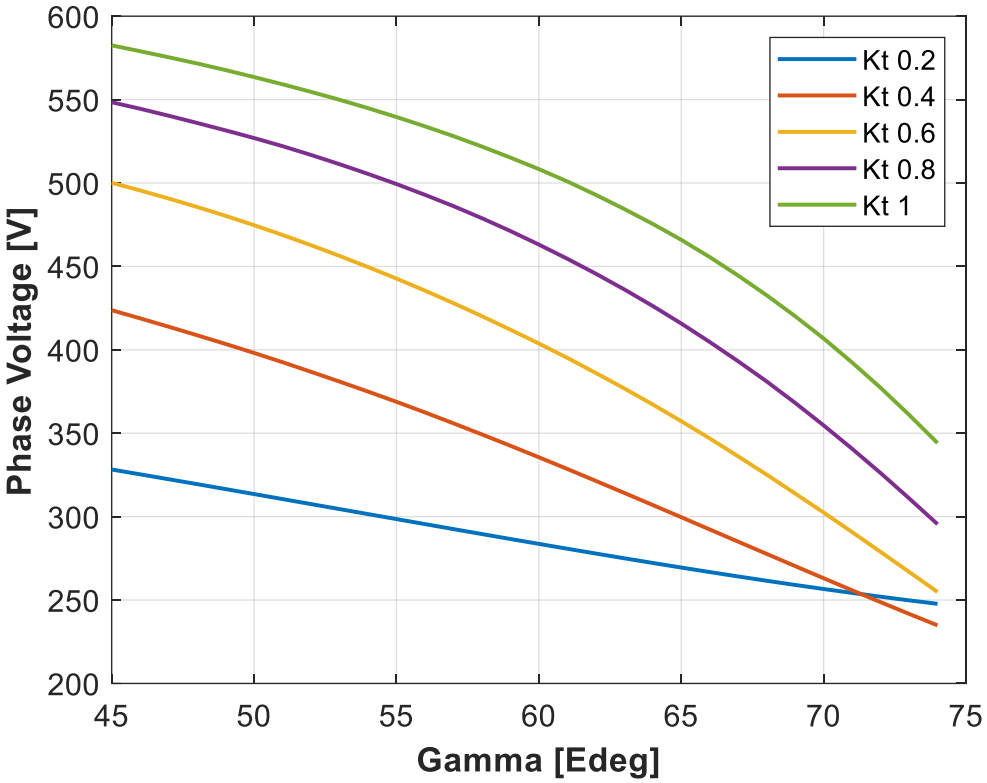

Fig. 38. Induced phase voltage at 1 kHz as a function of the electrical current vector angle

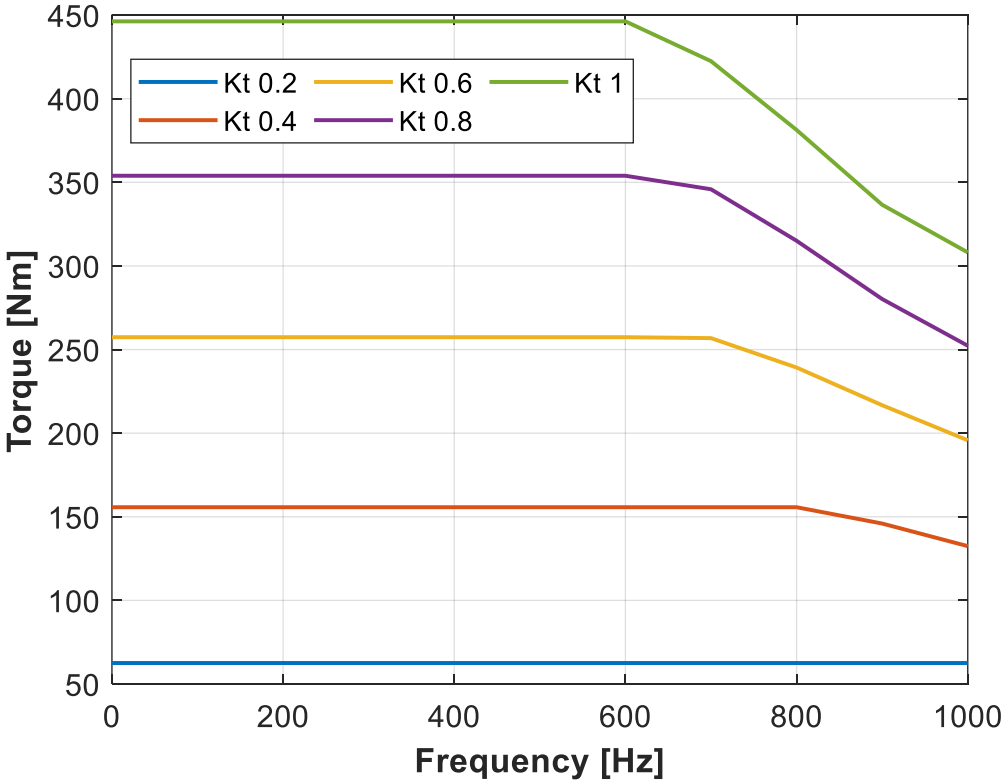

Fig. 39. Torque-speed characteristic from 0 to 1 kHz.

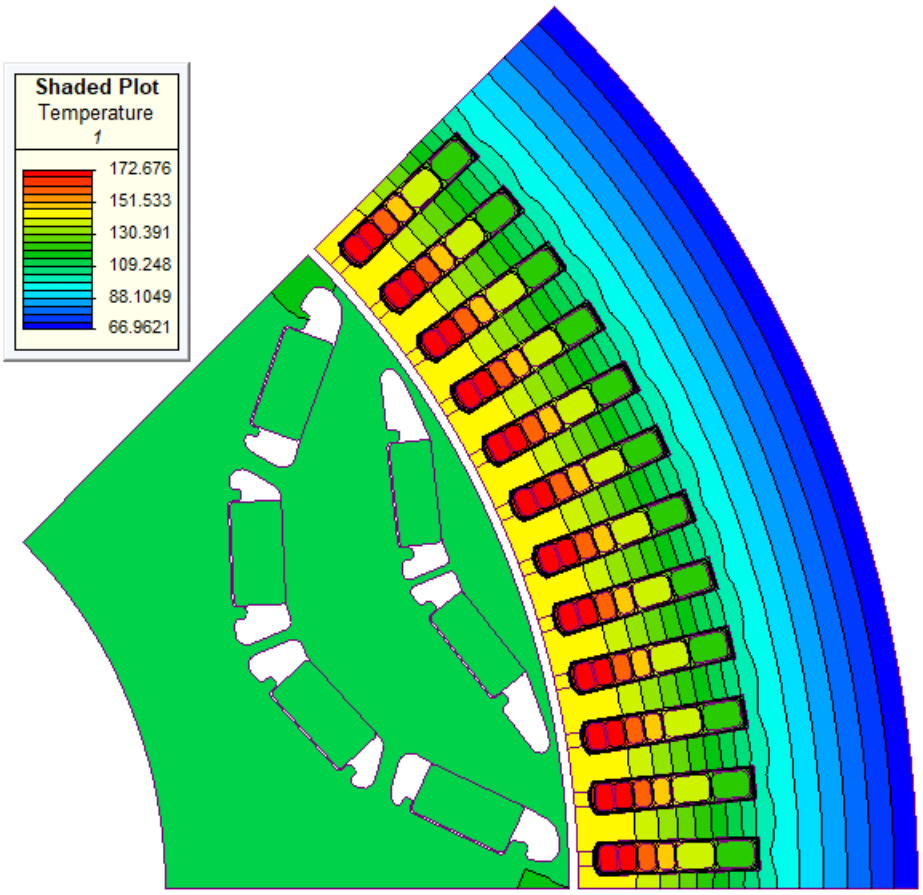

Fig. 40. Machine 2D thermal map at 9krpm with full load.

3.3.3 INDUCTANCE MAPS

For the sake of completeness, the inductance and permanent magnet flux maps are shown in this sub-section. From them, it is possible to estimate the behaviour of the machine in the different working conditions, which is usually a crucial aspect for the calibration of its control. Due to the huge amount of involved simulations, the maps have been realized with magnetostatic 2D FE simulations. The adopted method is the so called frozen permeability method (FPM) which allows a more precise estimation of the parameters also when high saturations occur. The FPM is a method with which the system can be linearized for a given operating condition. This feature allows to separate the d- and q-axis fluxes into their contributions from the permanent PMs and the stator inductances. It is also possible to take into account all the cross-coupling inductances and fluxes. More details about FP theory and application can be found in [62] and [63]. However, a short summary of the procedure is explained here:

- For a couple of d- and q-axis currents (I_d and I_q), a magnetostatic simulation is run, then the permeability of the entire model is blocked (i.e. “frozen”). In this

way the model is linearized for the specific working point and the superposition effects theorem can be applied. In other words, all the flux components can be considered separatedly for the working point, independently of whether the saturation is high or low. However, the obtained results are reliable only in correspondence of the operating condition, thus a dense set of I_d and I_q currents needs to be selected.

- The linearized model then is simulated with no currents, such that only the influence of the PMs is evaluated. In this way it is possible to obtain the PM d- Ψ_d and q-axis Ψ_q flux linkage components for every I_d and I_q.
- Two additional simulations are needed to obtain the d-axis L_d, q-axis L_q and dq-cross- coupling L_{dq} inductances: one with only d-axis current and another one with only q-axis current. For these simulations the PMs need to be replaced with a non-magnetic material having the same relative permeability.

Hence, four total simulations are run to obtain one set of L_d, L_q, L_{dq}, Ψ_d and Ψ_q, whose values are illustrated in the maps of fig. 41-46, when the PM temperature is 100°C. The adopted conventions for the dq transformation are instead the followings:

- The d-axis coincides with the PMs axis.
- Ψ_d produced by a north pole (flux lines concatenate the coil going outward) is negative. This is given by the FE software. Therefore, I_q has to be negative to develop a positive cylindrical torque.
- The dq transformation keeps constant the phase values. The values of the I_d and I_q are the currents flowing in each conductor (i.e. in each phase path).

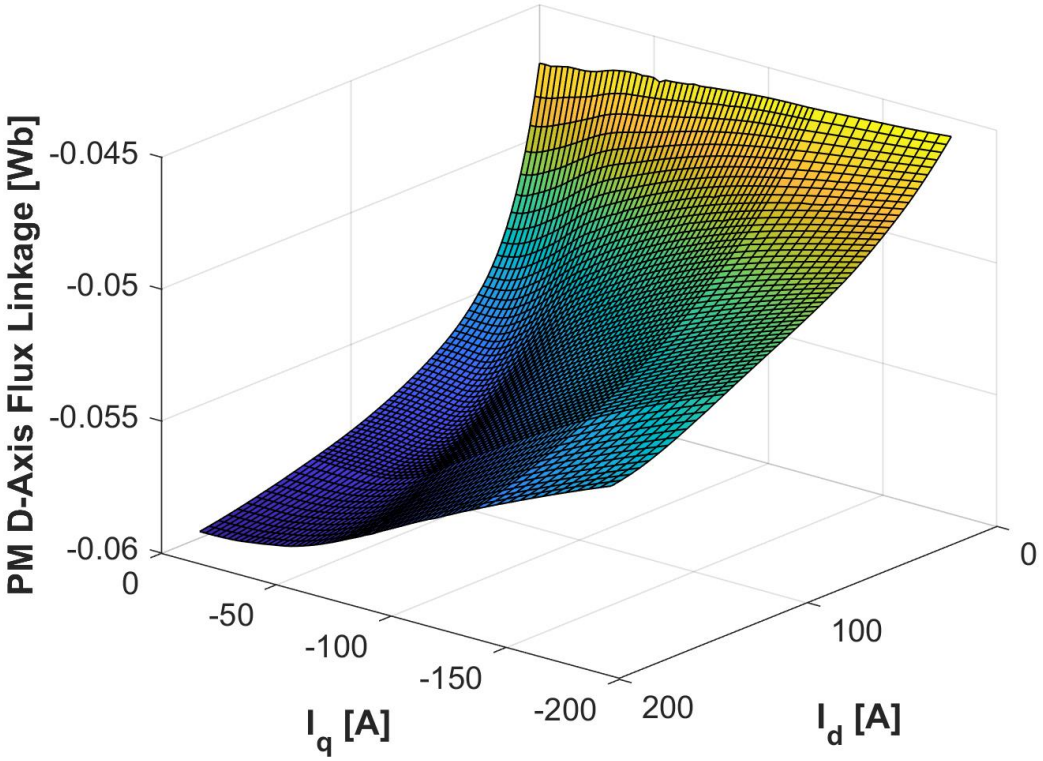

Fig. 41. Permanent magnet d-axis flux linkage component map.

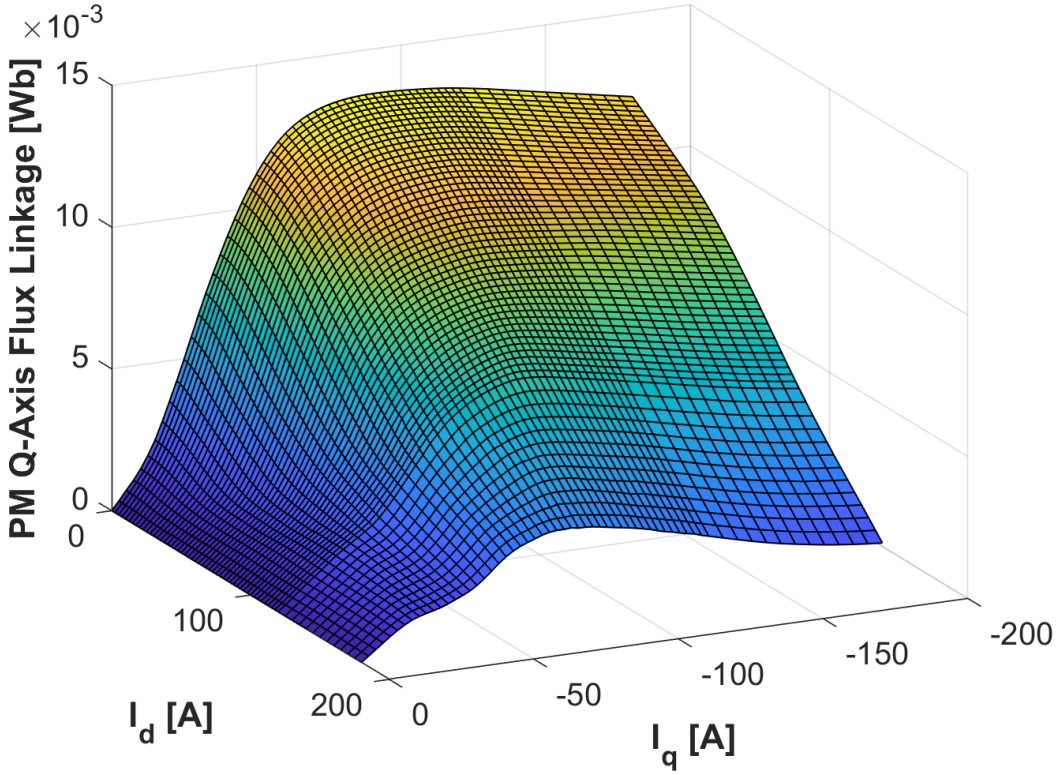

Fig.42. Permanent magnet q-axis flux linkage component map.

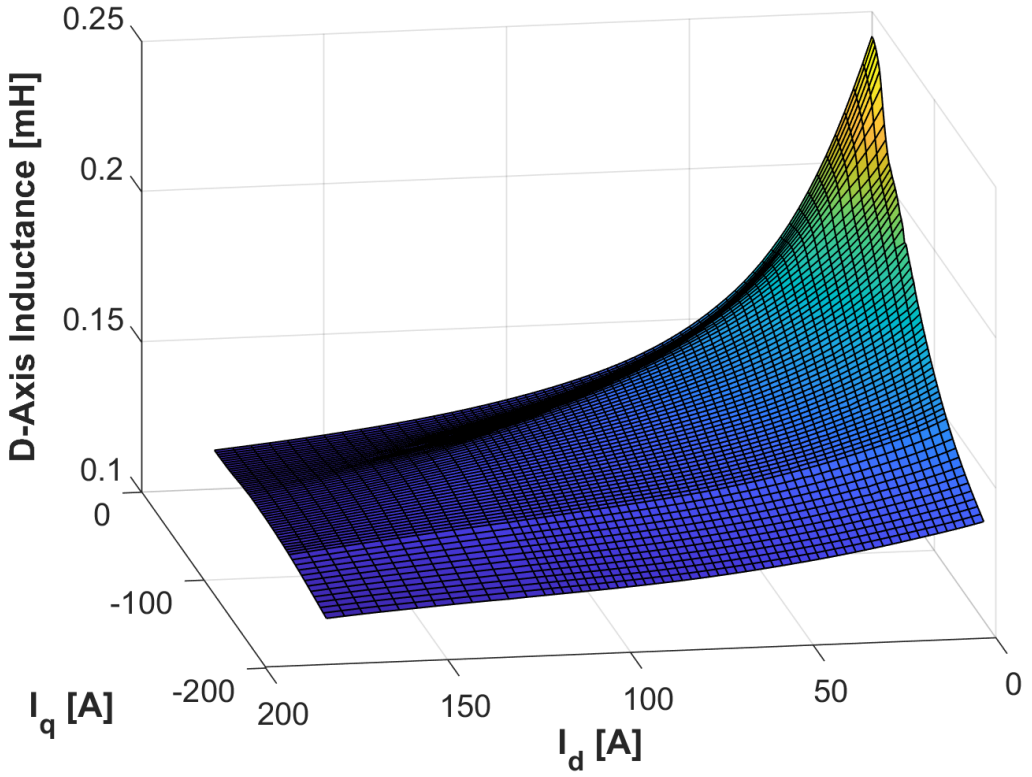

Fig. 43. D-axis machine inductance map.

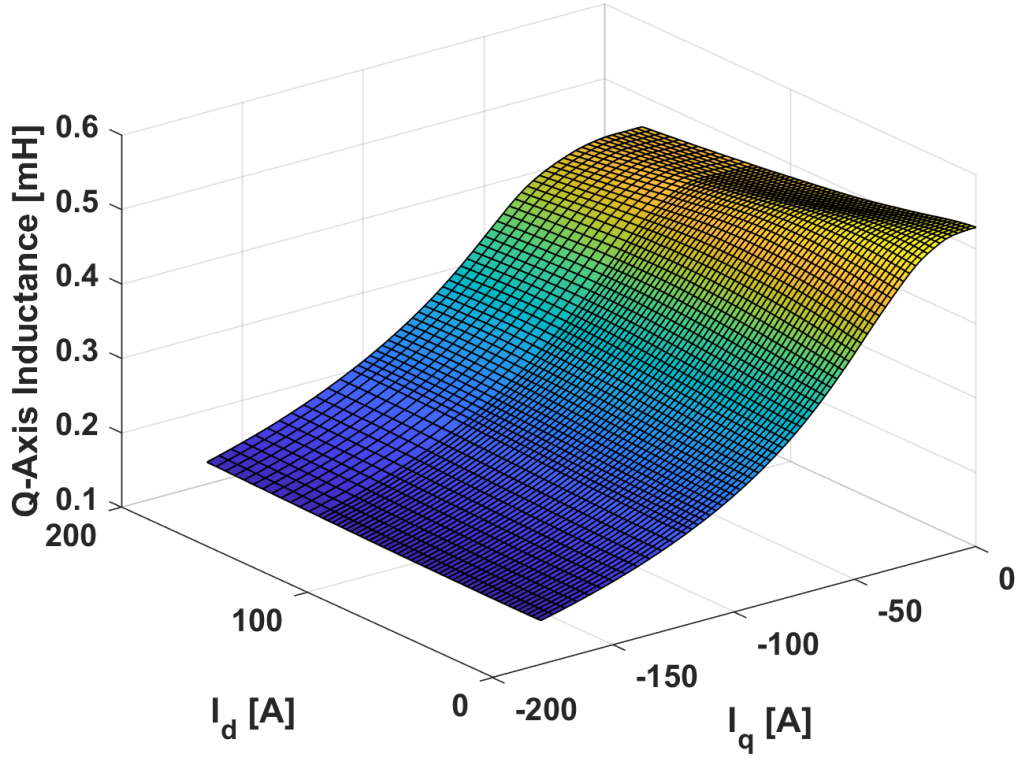

Fig. 44. Q-axis machine inductance map.

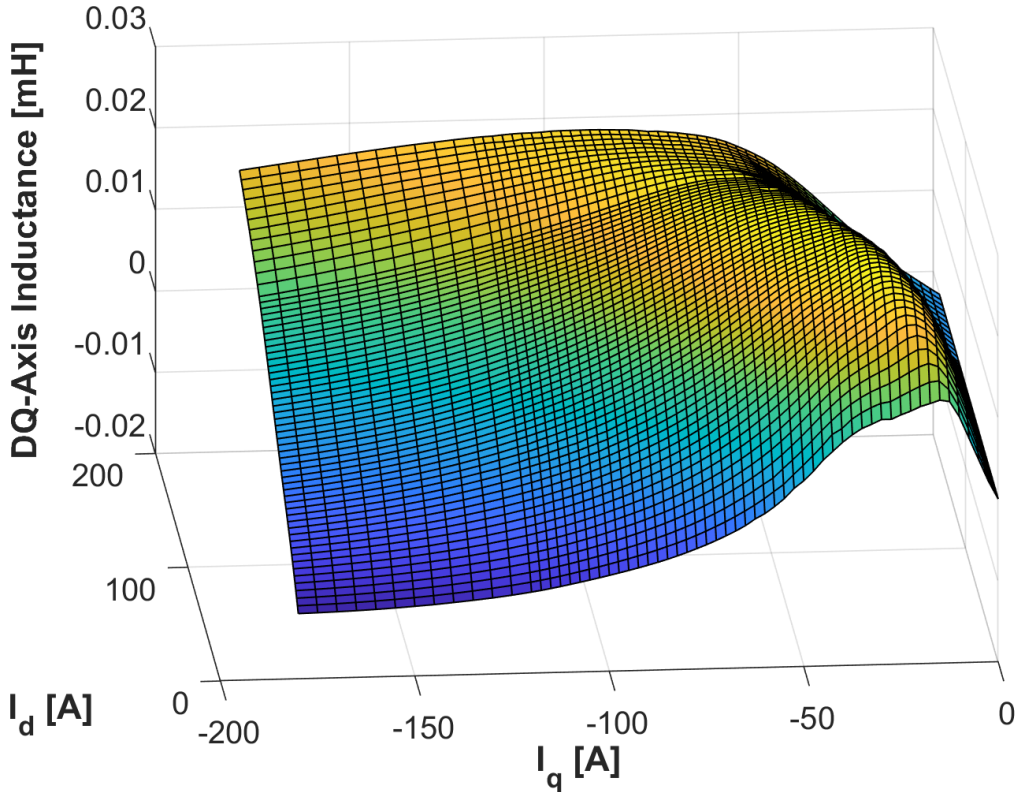

Fig. 45. DQ-axis machine inductance map.

It can be seen that the map shapes are not easily predictable and that the load heavily influences the behaviour of all the involved parameters. As expected, at low loads Ψ_q tends to zero, which means that from a PM flux linkages point of view, the model appears to be decoupled as an ideal one. However, this is not true for increasing loads, where both I_d and I_q affect the values of Ψ_q. Ψ_d is influenced by the load as well and cannot be considered constant. Different values of I_d and I_q modify with different impact the relative permeability of the entire machine, changing continuously the reluctance seen by the PMs. Another interesting aspect is provided by the L_{dq} map: at really low loads the cross coupling is negligible, however it rapidly changes for increasing values of the current, showing again that the hypothesis of a decoupled model could lead to significant errors, especially when the saturation is important. The maps of L_d and L_q have instead simpler shapes. In particular, L_q is mainly determined by the value of I_q, while both I_q and I_d have an important impact over L_d. From the inductance and the flux maps it is then straightforward to evaluate the torque map with the classical formulation. The torque map is shown in fig. 46 for current values I_d and I_q going from 0 to 200 A_{pk}. Not all the involved values are feasible for the drive, however having a larger amount of data regarding the machine behaviour could be useful.

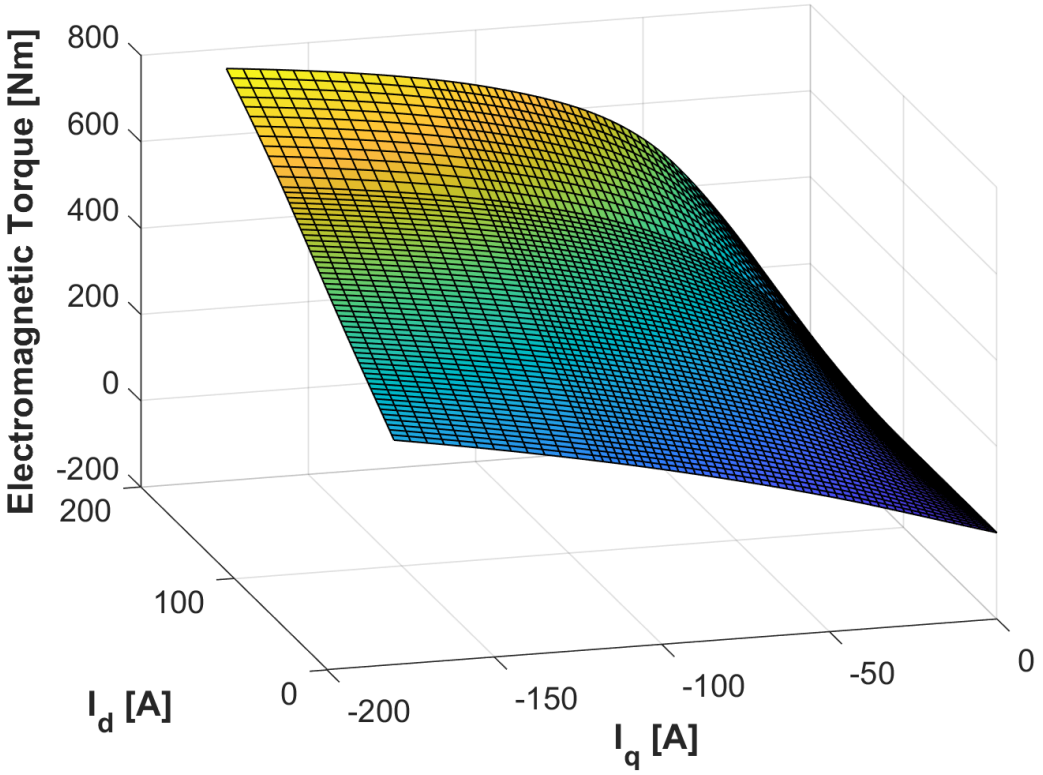

Fig. 46. Torque map as a function of I_d and I_q.

Having estimated the machine behaviour for many different operating points, a comparison between the estimated rated load torque characteristic obtained with the machine maps and the FE transient simulations can be done as a means of a validation of the mapping approach. The comparison is shown in fig. 47 with the torque as function of the current vector angle with respect to the q axis. The match is really good, thus the estimation of the machine characteristics through inductance mapping obtained with the FP method can be considered sufficiently reliable for the considered machine. This is a really important aspect since it can allow to generate, in a relative low amount of time, detailed inductance and flux maps. These maps can then be adopted to determine the initial set point of a maximum torque per ampere (MTPA) and maximum torque per voltage (MTPV) control strategy.

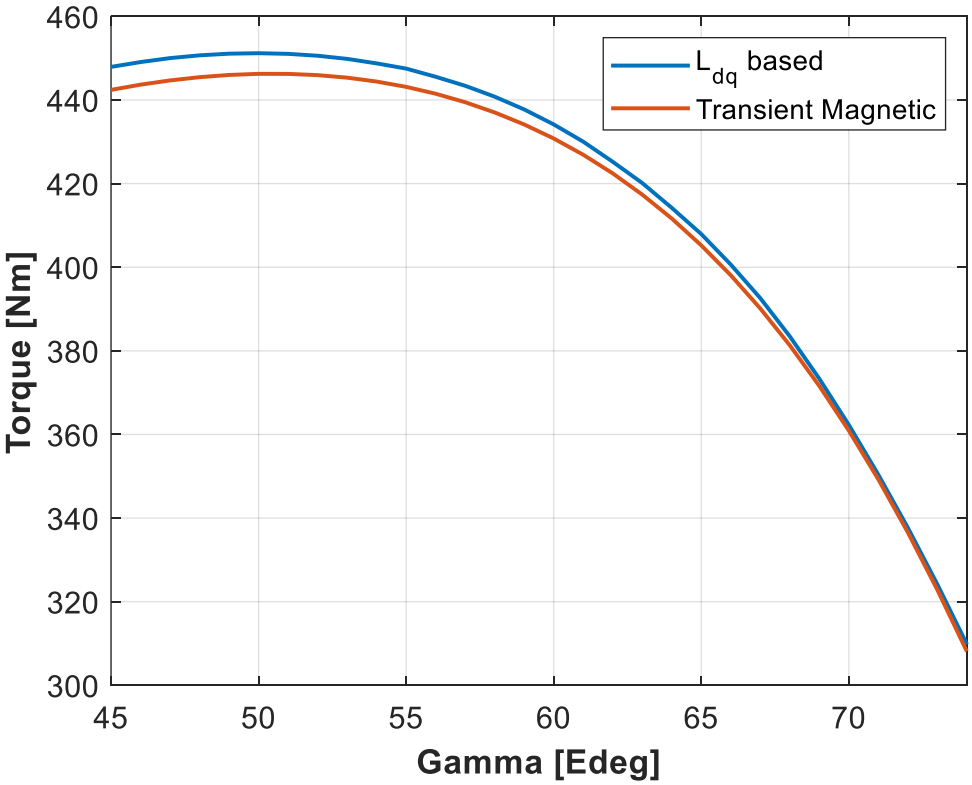

Fig. 47. Comparison between the torque obtained with transient magnetic simulations and inductance mapping at rated load.

3.3.4 Conclusion on Multi-Three-Phase HWs

Sections 3.1-3.3 have addressed the possibility to implement the combination of HWs with a multi-three-phase winding configuration. The analysis has been performed starting from some specific requirements for traction applications and a double-three-phase configuration has been selected in order both to exploit the main advantages of multi-phase machines and to limit the complexity of the electrical drive. This choice can, first of all, further increase the machine torque. In addition, it is easier to obtain wide constant torque speed regions. Being HWs sensitive to AC losses, a specific attention has been paid to the selection of the conductor dimensions, with their radial dimension being the most critical parameter. With a HW asymmetrical configuration, having two thicker conductors at the slot bottom and the remaining four with a smaller radial dimension, it has been possible both to keep the active length DC Joule losses low and to limit the AC losses for the entire machine operating frequency (0 – 1 kHz). The final result is a DTP machine which can easily meet all the initial minimum requirements. The machine dq-axis inductances and fluxes have also been mapped using the FP method. The calculated torque characteristic with this method matches with a high precision with those estimated

through the transient magnetic simulations, allowing a much faster mapping of the machine characteristics whose knowledge is needed for a proper MTPA and MTPV control strategy.

3.4 Analysis of End Winding AC Losses in HWs

Another important aspect relative to the design of HW machines is the estimation of the end winding AC losses. This section is focused on their impact taking as a case study the end winding of the machine model described in section 3.3, in order to have more reliable data about the total winding Joule losses.

3.4.1 Previous Studies

The majority of the studies available in literature have focused on the modelling and reduction of AC losses in the active part of machines, while few works have dealt with the end winding regions. In [64] and [65], the end winding leakage inductances are investigated, while in [12] and [66] their cooling is analyzed through oil spray. To the authors' knowledge, only in [67] and [68] the total machine Joule losses are analyzed and the end windings AC losses are considered separately. The results indicate that for a few hundreds of Hertz the end winding losses are nearly DC only, while the frequency dependent effects can become much more relevant around the 1 kHz range. However, a critical analysis on the end windings is missing and the impact of AC losses in the relevant regions is provided for a few values of the frequency. Hence, this section presents an analysis of the AC losses in the end winding regions for a wide frequency range and their comparison against losses occurring in the machine active part.

3.4.2 Case Study

As previously mentioned, the end winding AC losses study is performed starting from the double-three phase machine model under analysis. The winding parameters are summarized in Table VIII.

TABLE VIII. WINDING PARAMETERS

Winding topology	DTP Full Pitch
Slots	96
Number of poles	8
Number of slot conductors	6
Dimensions of conductor 1 [mm]	2.8 x 1.8
Dimensions of conductor 2 [mm]	2.8 x 4

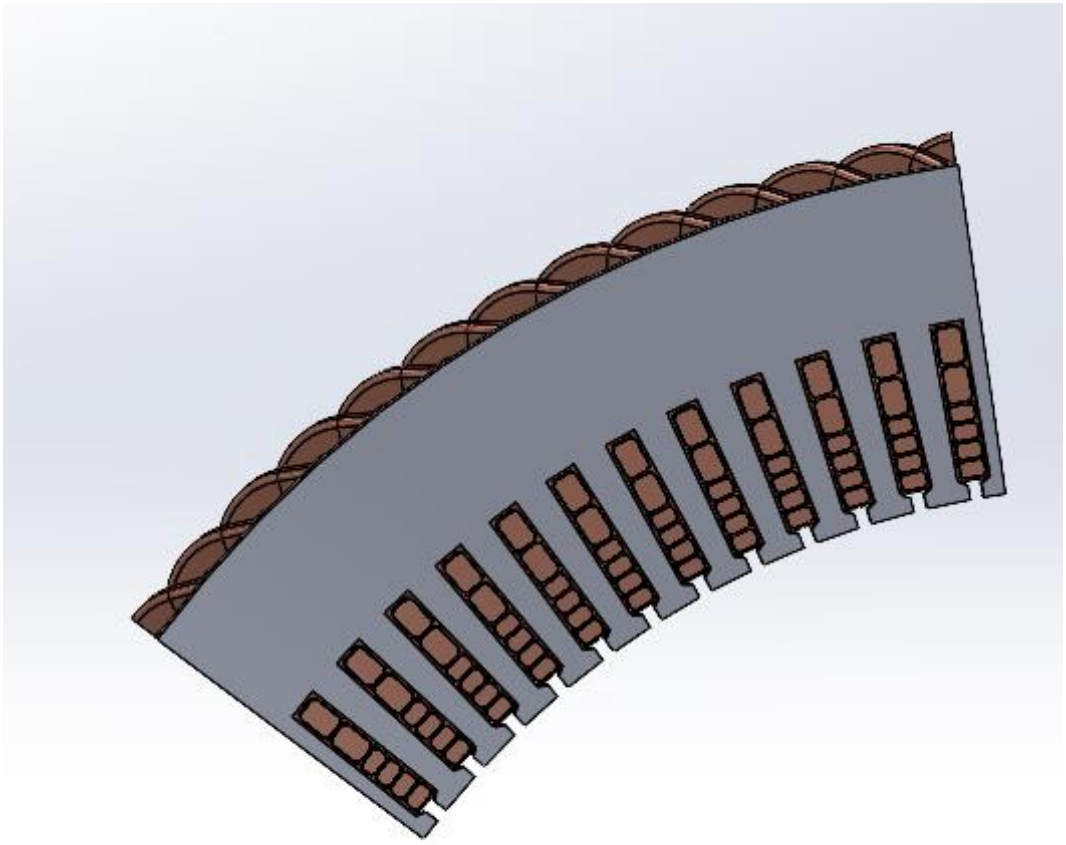

Fig. 48. 2D stator sector of the considered machine.

Two bigger conductors, having a radial dimension of 4 mm, are placed in the slot bottom and fill the first two winding layers, while the remaining layers are filled with the remaining four thinner conductors. While a 2D model (see fig. 48) is sufficient to calculate the Joule losses occurring in the active sides of the machine conductors, a 3D model is needed to determine them within the end winding region. First, a winding scheme is hypothesized and then, basing on it, the end windings are modelled though the

CAD-based software Solidworks, where connections and conductor transpositions are suitably built, as it can be seen in fig. 49 and 50. As opposed to 2D FEA electromagnetic modelling, 3D FEA simulations are quite laborious and can take a huge amount of time, thus some measures and assumptions are adopted to speed up the process. These include:

- only 1/8 of the machine is modelled, thus exploiting its periodicity as much as possible;
- since the aim is to study the entity of AC losses in the end windings, the active length can be reduced without affecting the end winding losses;
- the rotor influence on AC losses in the machine active part is somewhat present, but it is also usually quite limited as long as the machine is not highly saturated. Hence, being the end windings surrounded by air, the rotor can be neglected, allowing to further reduce the computation burden. In addition, it allows the adoption of the time harmonic simulations rather than transient with motion ones, which would require much more time to be solved;
- only the end winding insertion side is modelled. Apart from the welding spots, HW end region sides are rather similar, and a similar behavior can be assumed in terms of AC losses. However, the insertion side tends to be slightly more compact, thus it is the one where a slightly higher impact of the proximity losses is expected.

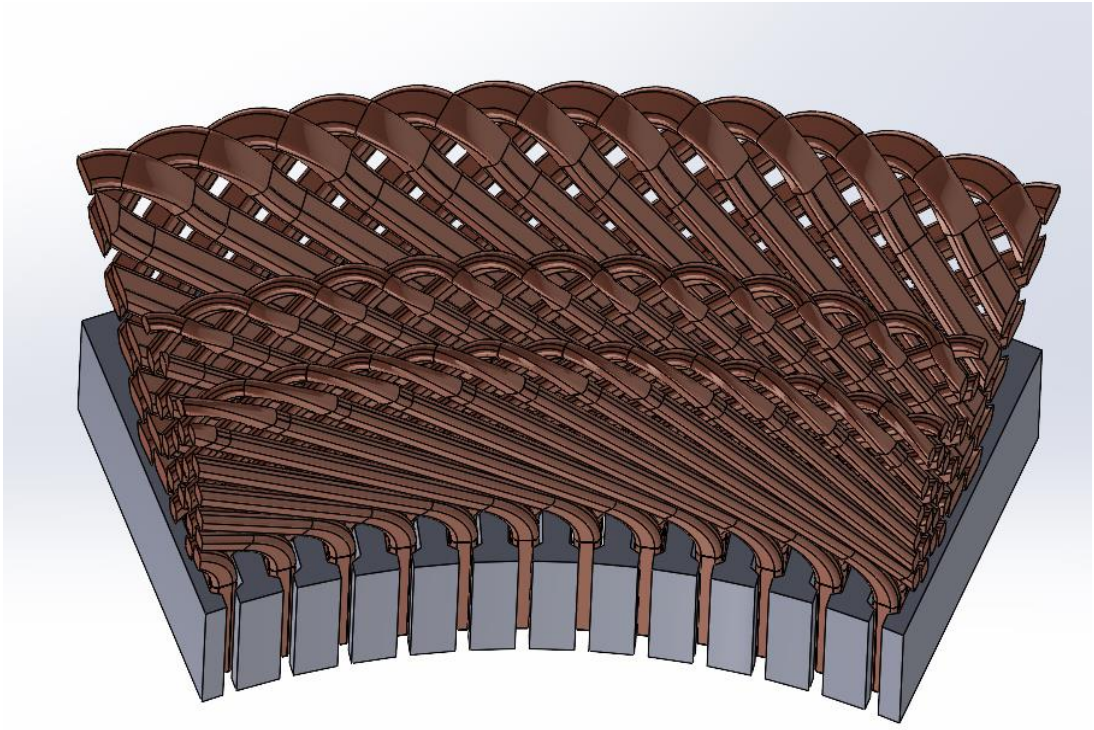

Fig. 49. 3D model of the machine sector. Front view.

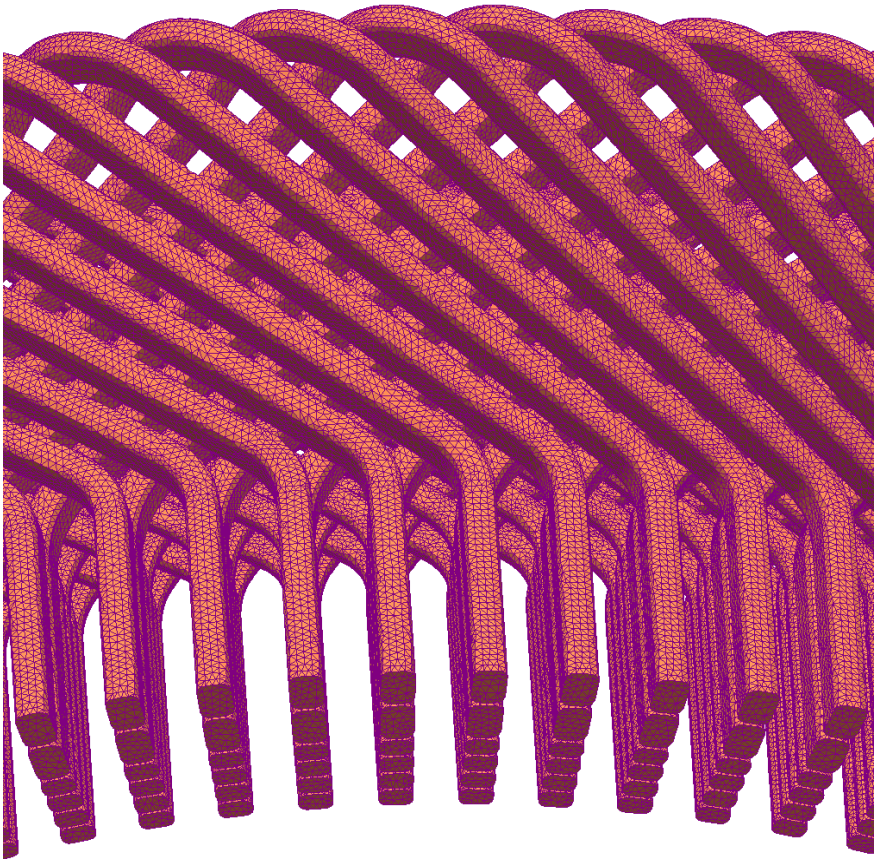

Fig. 50. 3D Model of the winding. The mesh is displayed.

3.4.3 SIMULATION RESULTS

Two types of FEA simulations are performed in the 2D and 3D models: 1) static simulations are carried out to evaluate DC losses and 2) time harmonic simulations are performed to evaluate AC losses as a function of frequency. The frequency range varies from DC to 1500 Hz, which covers the whole automotive typical operating range. All the simulations are run imposing sinusoidal currents feeding the phases, while the conductor material is pure copper with a temperature of 120°C. The simulations have been performed also for two opposite case studies: with low saturation (LS) and with high saturation (HS) where the ferromagnetic material has been replaced with a lower permeability material. The method to isolate the end winding region losses is quite straightforward. Once 3D and 2D simulations have been performed, the end winding losses, P_{ew}, can be estimated by simply subtracting the 2D active Joule losses to the total losses of the 3D model for both static and time harmonic simulations. An important aspect regards the estimation of the end winding AC/DC loss ratio K_r. Nearly all the connections are between the following layers: layers 1 and 2, layers 3 and 4, and layers 5 and 6 as underlined in [20]-[24]. There are a few exceptions, provided by the jumpers, which can

connect layers 2 and 3 or layers 4 and 5, but their number is much lower and is kept usually as low as possible. In addition, they are not present in correspondence of all the machine poles. In the considered machine sector, no jumpers are modelled, thus three main types of connection are considered in the end winding of the modelled part. For this reason, three different K_{rk} can be evaluated, depending on which layers' connection is considered (i.e. L1-L2, L3-L4, L5-L6). Fig. 51 illustrates the different values of K_{rk}, depending on the connected layers for the end winding region, while fig. 52 shows the 2D (active length) counterpart, where the average K_{rk} every two layers (ETL) is evaluated for the sake of comparison. From the theory illustrated in [32], it is known that the value of K_{rk} for each layer is strictly linked mainly to the operating frequency, conductor radial dimension and the position of the layer. From the theory it is known that the value of K_{rk} for each layer is strictly linked mainly to the operating frequency, conductor radial dimension and the position of the layer. In fig.51 and 52, it can be seen that, in the end winding region, the impact of the layer position is lower but still exists. In fact, the lower K_{rk} occurs in both cases for the conductors of L3-L4, which have the same dimensions as those of L5-L6.

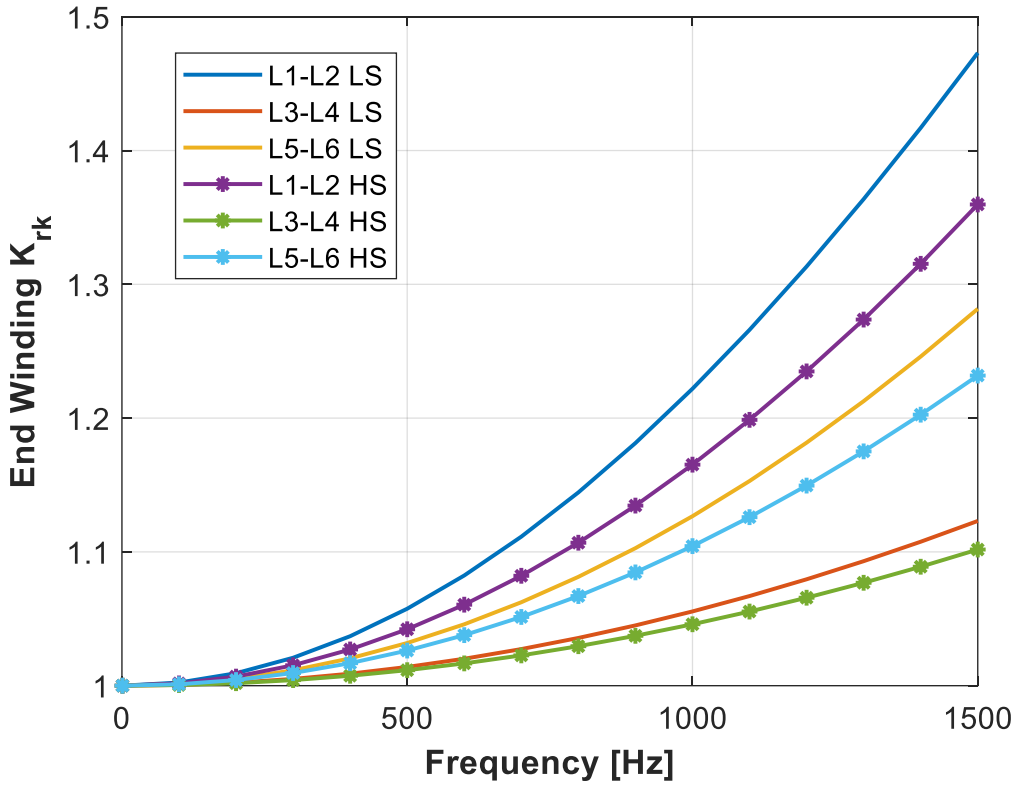

Fig. 51. End winding K_{rk} as a function of frequency for the three different connections.

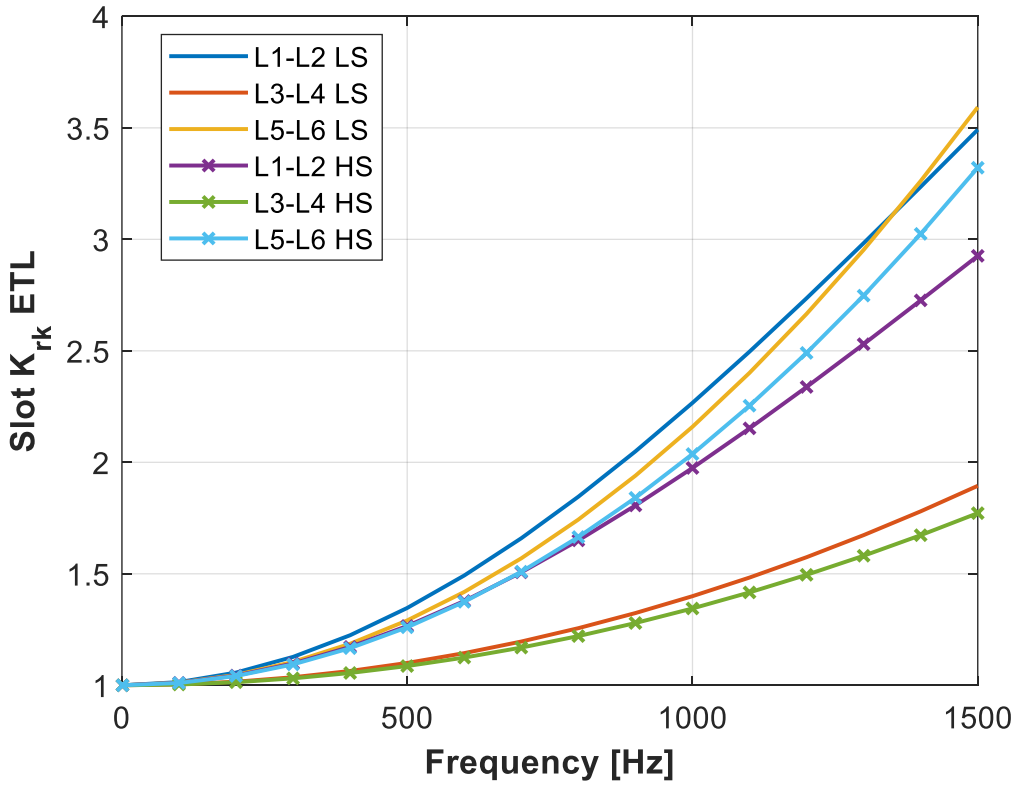

Fig. 52. Active length K_{rk} every two layers as a function of frequency**.**

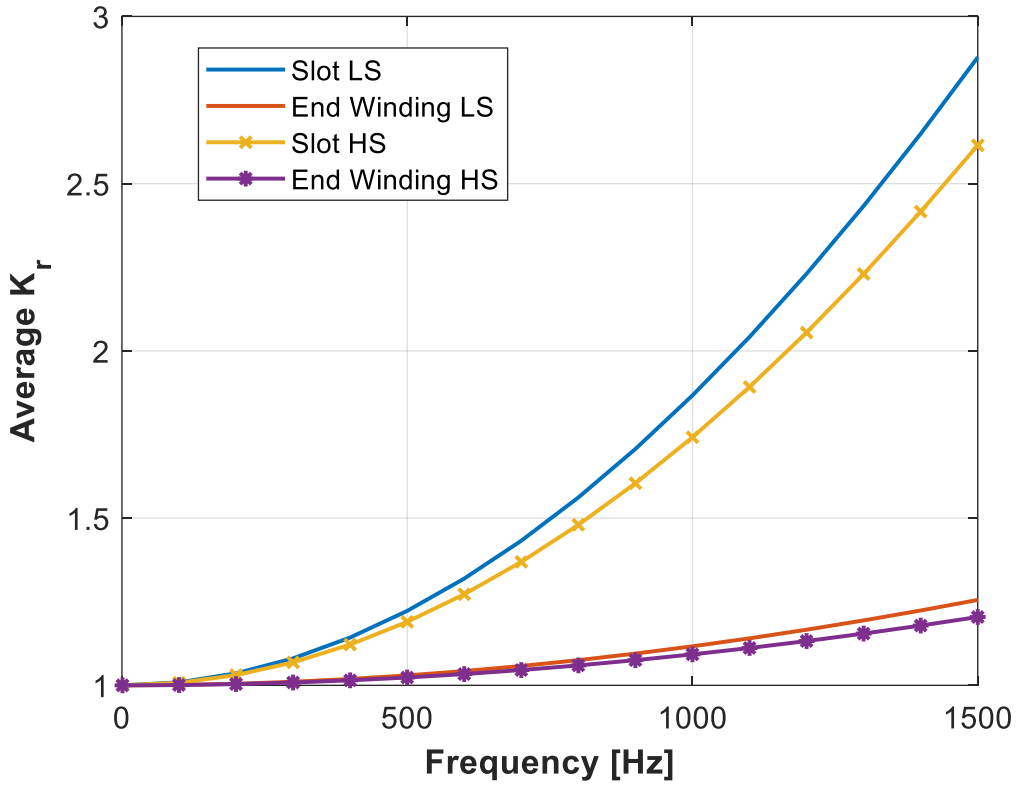

Fig. 53. Comparison of the average value of the AC/DC losses K_r for the entire end region and active part of the winding.

Fig. 53 provides a comparison in terms of the average K_r between the end windings and the active part. Fig.53 can be useful to provide a comprehensive overview of the entity of AC losses in the entire end region. It can be seen that, for the maximum frequency of 1500 Hz and LS, a value of 1.26 is nearly obtained. However, in the range from 0 to 900 Hz, the average value is always below 1.1 and with a value of only 1.05 at 650 Hz. In the active part it has a value of 2.9, 1.9 and 1.23 respectively at 1500 Hz, 1000 Hz and 500 Hz. It can be noted also that the K_r curves during conditions of HS are always similar to the ones of LS, but slightly lower values are obtained. In fact, the maximum average K_r is 1.2 at 1.5 kHz for the end winding region and 2.61 for the active one. Thus, the core saturation has also some influence on the end winding region and determines a reduction of the AC losses as in the active part, even if the impact seems quite limited. While the obtained results are strictly related to the specific design of the considered case study, the findings suggest that the end winding losses can be at first approximated as frequency-independent for a considerable frequency range with an acceptable error. In fact, for the considered worst case scenario (LS), K_r in the end winding region exceeds 1.1 only when K_r approaches 1.7 in the active part, which occurs above 900 Hz. For higher values, this approximation could start to be unacceptable, as it can be seen also in Fig. 54.

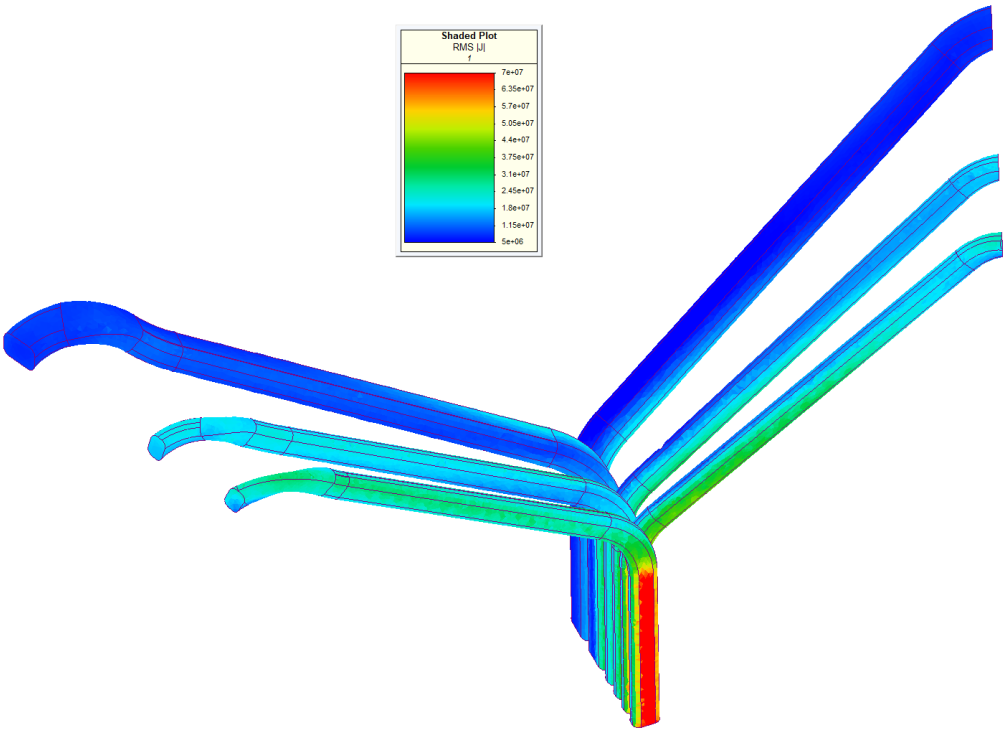

Fig. 54. RMS value of the current density in the conductors of a single slot at 1500 Hz for LS.

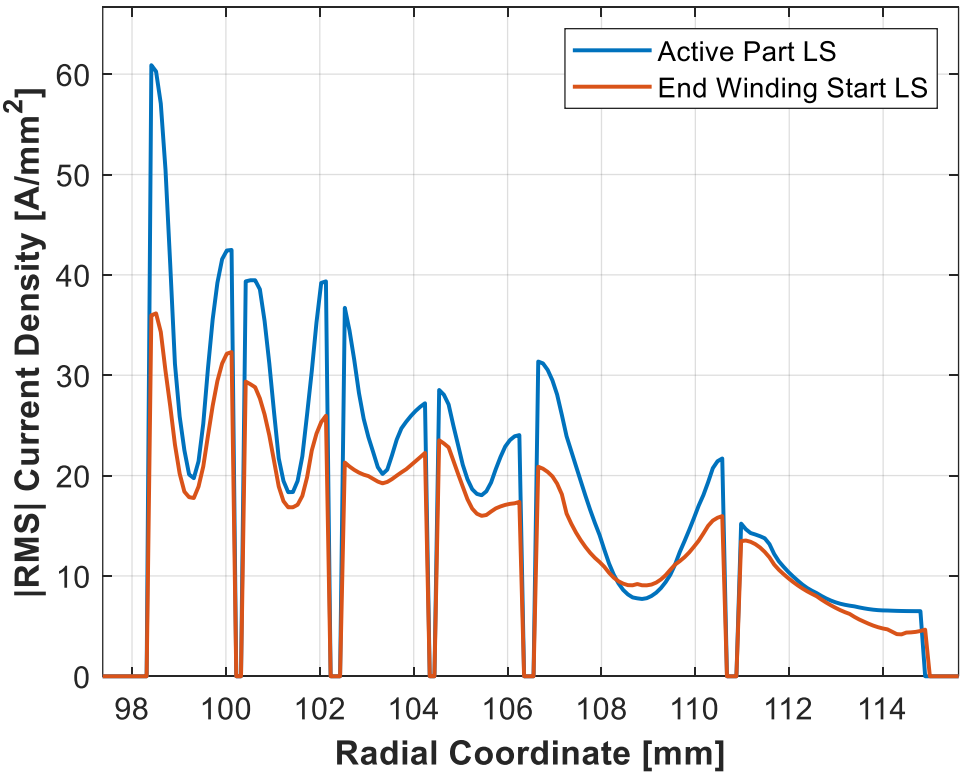

Fig. 55. RMS value of the current density in the conductors of a single slot at 1500 Hz as function of the radial coordinate for LS.

Fig. 54 illustrates the current density map for the conductors of a single slot at the maximum evaluated frequency of 1500 Hz and LS. It can be noted that the values are significantly higher in the active part, however the current displacement is still visible also in the end winding due to the relatively HF. In particular, as quantified in fig. 51, the higher values are obtained in the conductors of the layers 5 and 6. Further details can be provided by fig. 55 and fig.56, where the current density and the flux density are plotted as a function of the radial position for two locations: in the middle of the active part and the at the beginning of the end winding region, at a distance of only 2 mm from the active part. Quite similar results are obtained for both LS and HS, thus only the curves for LS are shown. It can be noted that, in the first part of the end winding region, where the border effects are high, the current density distribution is still uneven, even if much lower peak values are obtained compared to the active region. Fig. 56 is instead useful to understand better the previous results. The RMS value of the flux density |B| is shown here, where the same trend for the active part and the end winding region can be observed, with the main difference being that in the end region it is flatter. The value of |B| is directly linked to the proximity effects, which are stronger where there is a higher a value, while

the K_{rk} depends mainly on the proximity effects and conductor radial dimensions. For this reason, in the end winding L3-4 experiences again lower values than L5-6 since they have the same dimensions, but are still subjected to different |B| values. On the other hand, L1-2 has a higher K_{rk} due to its much bigger radial dimension, which has proportionally a higher impact when the |B| distribution is more even.

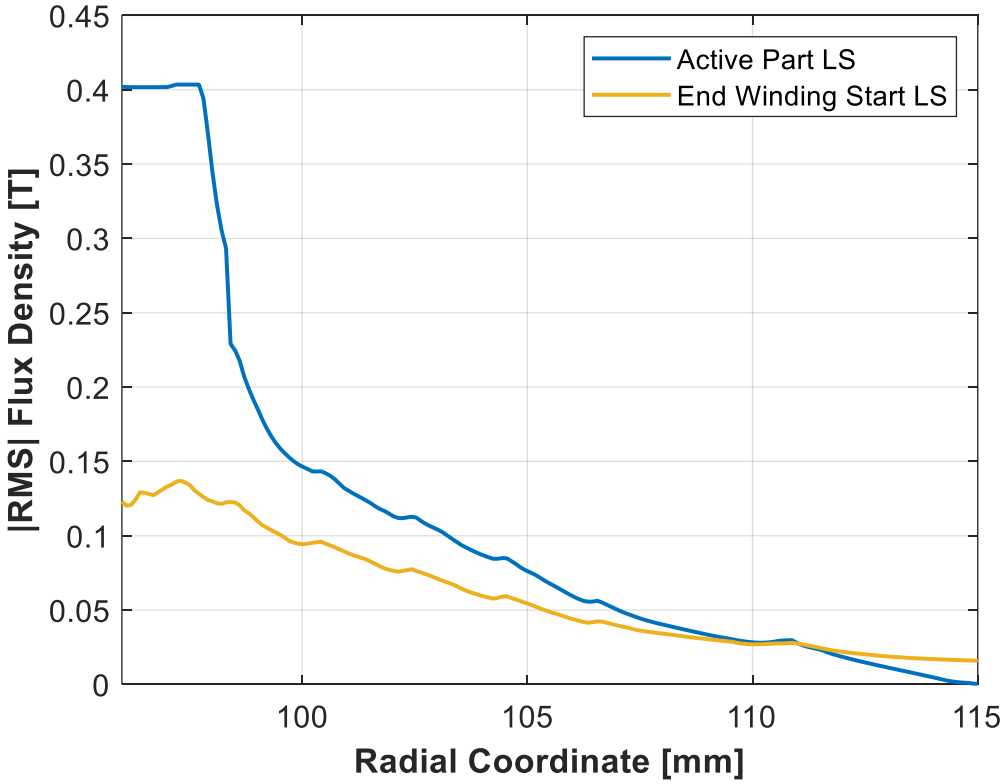

Fig. 56. RMS value of the flux density as function of the radial coordinate for LS.

3.4.4 Conclusion on End Winding AC Losses

Section 3.4 focused on the analysis of the AC losses occurring in the end winding regions of a HW machine through 3D FEA simulations. The modelling approach and the main assumptions to reduce the computation burden for the 3D analysis were illustrated in detail. The AC/DC loss ratio K_{rk} was evaluated for the different layer connections in the end windings, and its average value was compared also with the one occurring in the active part for a wide frequency range (up to 1.5 kHz). It was observed that the layers involved in one of the connections still have some influence on K_{rk} also in the end windings, though with a much lower impact than in the active part of the machine. Additionally, it was proven that the end winding region exhibits low values of K_r for several hundreds of hertz, allowing to approximate the losses as pure DC with a relatively

low error (<10 %), while this approximation is no longer reasonable when approaching 1 kHz. Since the actual operating frequency of the considered machine is 0-1 kHz, the initial hypothesis of DC losses end winding can be considered as acceptable.

Future work will focus on analyzing other machine topologies and/or other end winding shapes, with the aim of generalizing the approach and of providing design recommendations related to the end conductors of HWs. Some prototypes will be also built to validate the developed FEA models and the main findings of this section.

3.5 FINAL CONSIDERATIONS ON CHAPTER 3

Chapter 3 has addressed the possibility to improve the machine performance through the adoption of multi-three-phase HWs, and with a proper conductor dimension choice to mitigate AC losses. For HF values AC losses can become relevant also in the end windings. However, if the conductors were already optimized to reduce active length losses (as done in this thesis), the AC component would more likely be low, and the approximation as DC losses would determine a low error.

This chapter was then focused on torque density and efficiency improvements of HWs electrical machines intended for transport applications. The next chapter will be rather focused on their reliability, through the analysis of the voltage stresses occurring within the windings and the possibility to mitigate them in order to increase the insulation lifetime.

4. Analysis of Voltage Stress Within Electrical Machine Windings

Increasing machine performance figures, such as reliability, efficiency and power density are key factors to reduce the energy consumptions and to save materials, which is a crucial objective in view of a higher sustainability. Increasing insulation lifetime and consequently machine lifetime goes in the same direction and this goal can be achieved through the reduction of the root causes. Electrical and thermal stresses are primary sources of insulation aging [71]. Thermal stress can be reduced with a proper cooling system and current density selection. On the other hand, electrical stress can be more difficult to predict and mitigate. It depends also on the drive parameters (cable length, voltage amplitude and rise time, involved materials, etc.) which are often fixed for a certain application or can be only slightly modified. Hence, this chapter is focused on modelling the main sources of electrical winding insulation stress and on possible ways to reduce them.

4.1 A Comprehensive Modelling Tool for the Characterization of Electric Drives Based on Fast Switching Semiconductors

Usually, power appliances are designed to operate with input voltage within 10% of the rated nominal value. All other voltage excitations may be seen as transients, which may arise from abnormal conditions, such as: short-circuits, switching operations, lightning discharges, and from almost any change in the operating conditions of the system. There are exceptions, for example, electrical machines fed through PWM voltage source converters, since these produce steep voltage pulses which are applied repeatedly to the machine terminals [69]. The inverters may produce voltages with very short rise times, which in presence of long cables may increase the electrical stress significantly, leading to partial discharge inception and to the stator insulation failure in a short time.

In general, standards classify the transient voltages that power equipment experiences into four groups [70], including:

1) Low-frequency transients, which are oscillatory voltages (from power frequency to a few kHz), weakly damped and of relatively long duration (i.e., seconds, or even minutes).

2) Slow front transients, which refer to excitations caused by switching operations, fault initiation, or remote lightning strokes. They can be oscillatory (within a frequency range between power frequency and 20 kHz) or unidirectional (with a front time between 0.02 and 5 ms), highly damped and of short-duration (i.e., in the order of milliseconds).
3) Fast front transients, which are normally aperiodic waves, generally associated to lightning surges with a front time between 0.1 and 20 μs.
4) Very fast front transients, referring to surges with rise times in the range up to 100 ns and frequencies from 0.5 to 30 MHz.

The capability of a winding to withstand transient voltages depends on the specific surge voltage shape, the winding geometry, the insulation material, the voltage-time withstand characteristic and the past history of the winding [71]-[72]. The voltage stresses within windings need to be determined to design a winding insulation suitable for all kinds of over-voltages.

Transients cause both over-voltages at the machine terminals [73] and uneven voltage distributions within machine windings [74]. These result in increased local thermal and electric stress on the insulation system and additional losses, which in turn cause an accelerated degradation of the insulation and its electrical properties [75]. Stator insulation failure is one of the main reasons for machine breakdowns and the introduction of power converters utilizing WBG devices, based on Silicon carbide (SiC) or Gallium Nitride (GaN), further increase the electrical stresses.

The accurate prediction of the response of coils and windings to fast or very fast voltage surges is a complex problem and is generally addressed by building detailed models. The earliest attempts were made in 1910s, but until 1960s these efforts were of limited success due to computational limitations. This changed with the application of computers and the development of efficient computational algorithms. In this context, several modelling approaches have been proposed and applied to study the behaviour of windings.

4.1.1 Methods for the Prediction of Voltage Overshoot at Machine Terminals

Voltage overshoots at machine terminals are linked to the HF behaviour of the system, so HF models of the system, in particular of the feeding cable and the machine, are mandatory. There are two typical approaches used for the development of such models: the finite element (FE) analysis [76] and the direct measurement through an RLC meter

[77] or an impedance analyser [78]. FE models can be rather time consuming: in fact, while a 2D approximation of the field problem is usually sufficient for the cable [79], a full 3D analysis may be required for the electrical machine. Hence, when the electrical motor is available, the equivalent parameters extraction is carried out through impedance measurement. While the electrical machine's models always consist in lumped-parameters ones [76]-[80], the cable can be represented either through transmission lines [78] or with a series of sufficiently short lumped sections [77], approximating a distributed parameter line. For both cases, the per unit length impedances (stray capacitances, inductances and resistances) need to be extracted. It is clear that the accuracy for the voltage overshoot estimation depends on both the modeling approach and the parameter extraction. The machine terminals overvoltage is mainly caused by the differential mode (DM) behaviour of the system. Hence, rather than using three-phase models [79], its estimation can be carried out via DM models [78], thus saving simulation times without significantly compromising the accuracy.

4.1.2 Methods for the Prediction of the Voltage Distribution Within Machine Windings

The uneven voltage distribution process occurring in electrical machines has been investigated for both form-wound [81], [82] and random-wound windings [83], [84]. While in form-wound coils the interturn voltages are not so critical due to the sequential winding location, random-wound windings can have significant effect on parasitic parameter values [85]. A classical way to model such phenomenon is based upon multi-conductor transmission line theory [86], where the relative electrical parameters can be calculated either using simplified analytical approaches or more accurate FE evaluations [83]-[87]. Depending on the objectives of a specific research activity, the equivalent circuits usually implemented for estimating the voltage stress within windings can be complex and the estimation of the circuit parameters can be computationally expensive. Therefore, usually some mutual parameters (e.g. mutual capacitances between turns) are neglected, dielectric losses are not taken into account and the calculations are made for one frequency only [83], [87], [88]. In specific applications, e.g. when front transients are not very fast, losses cannot be neglected [89] and sometimes a frequency-domain modelling approach may be needed [90].

While a number of "uncoupled" modelling approaches are adopted for the estimation of over-voltages at the machine terminals and of the voltage distribution within windings,

this thesis proposes a coupled and fully comprehensive methodology which is able to provide information regarding both these quantities, simultaneously.

The tool can represent a powerful means to ensure a reliable design of electric drives employing converters with fast switching devices such as SiC and GaN. This is especially important in the aerospace field, where there is an ever-increasing need for HF operations, on one side, and for elevated reliability levels, on the other hand [91], [92]. The proposed modelling approach can be used to estimate the impact of the electrical aging on the electrical machine insulation system when its output quantities (i.e. over-voltages and voltage distributions) are considered as electrical input parameters in a suitably built lifetime model.

4.1.3 CONVERTER-CABLE-MACHINE MODEL

The PWM pulses deriving from WBG devices can reach very high voltage gradients (*dV/dt*), even higher than 20 kV/μs. The associated HF harmonics have a significant impact on the maximum voltage value at machine terminals. The wavelength of an electromagnetic wave is inversely proportional to its frequency, so at frequencies in the order of a few MHz the wavelength of these harmonics is comparable or smaller than the cable length, even for a few meters' cable. If a voltage pulse is applied to a cable of sufficient length, forward and backward travelling waves occur. These travel at a speed $v = 1/\sqrt{L_0 C_0}$, where L_0 and C_0 are the per-meter inductance and capacitance of the cable. Another important parameter is the cable characteristic impedance, which is defined as the ratio between the forward travelling voltage wave and the corresponding current wave. At very HF, the characteristic impedance can be simplified as $Z_0 = \sqrt{L_0/C_0}$. The behavior of the system strongly depends on v and Z_0. However, also the cable length and the characteristic impedance Z_m of the electrical machine supplied by the PWM pulses play a significant role. The so-called reflected wave occurs when there is an impedance mismatch between feeding cable and electrical machine. Since Z_0 and Z_m are usually rather different, a reflection appears, giving rise to a certain overvoltage. The reflection coefficient is defined as in (45) and the maximum theoretical voltage V_m (i.e. when a full reflection occurs) at machine terminals is as in (46), where V_{in} is the voltage applied at the beginning of the line.

$$\Gamma = \frac{Z_m - Z_0}{Z_m + Z_0} \qquad (45)$$

$$V_m = V_{in}(1 + \Gamma) \qquad (46)$$

Typically, $Z_m >> Z_0$, so V_m can reach up to twice V_{in}. A full reflection happens when the cable is longer than the critical length l_{cr} of the system, which is a function of v and the pulse rise time t_r, i.e. $l_{cr}=v \cdot t_r/2$. The equivalent mathematical condition for which there is a full reflection is $t_r < 2 \cdot t_p$, where t_p is the propagation time of the applied pulse. Nevertheless, a full reflection can happen also for $t_r < 3 \cdot t_p$ [93] and the voltage at the machine terminals, under particular conditions, can be even higher than twice V_{in} [94].

As mentioned above, the overvoltage can be analysed through a DM model. The proposed model replicates the system behaviour when the inverter, driven by Space Vector Modulation, has an output transition from state V_0 (0,0,0) to state V_1 (1,0,0) (see fig. 57). This assumption is valid considering that for a 2-levels inverter only 3 switches are working at the same time, providing in state S1 a current path with one phase (e.g. A) connected in series to the parallel of the other two phases (e.g. B and C). A voltage source, generating the converter output voltage, and HF cable and machine models connected

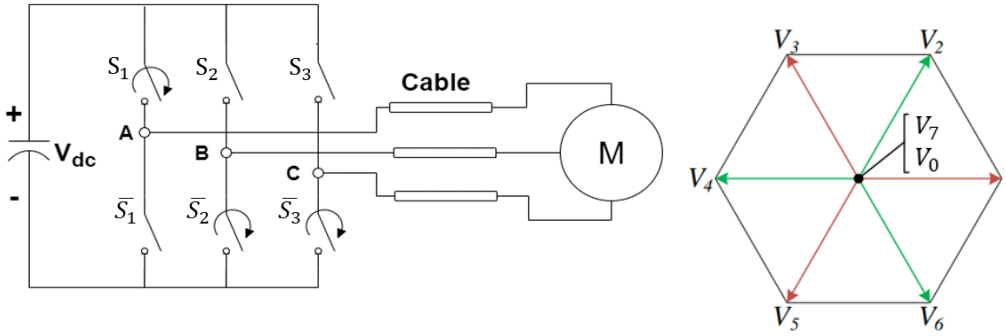

Fig. 57. Inverter, cable and machine scheme: commutation of the inverter.

together realize the equivalent DM circuit for line-to-line voltage evaluations. It is worth to note that, although this work is focused on DM overvoltage, the calculated equivalent parameters can be used also to build common mode (CM) or three-phase models.

4.1.3.1 CONVERTER

The converter is modelled as black-box, providing the output voltage. For preliminary investigations, the converter is modelled as an ideal DM voltage source providing an output voltage whose amplitude, rise time, frequency and duty cycle can be customized for every simulation, allowing to perform sensitivity analyses on the system behaviour at different supply conditions.

4.1.3.2 CABLE

The HF model of the feeding cable is based on [78], which determines the equivalent cable parameters through impedance measurement for different frequency values. However, some updates and modifications are applied in this work. The equivalent longitudinal parameters are not lumped only in the supply path (phase A), but also in the return path (phase B in parallel to phase C), as seen in fig. 58.

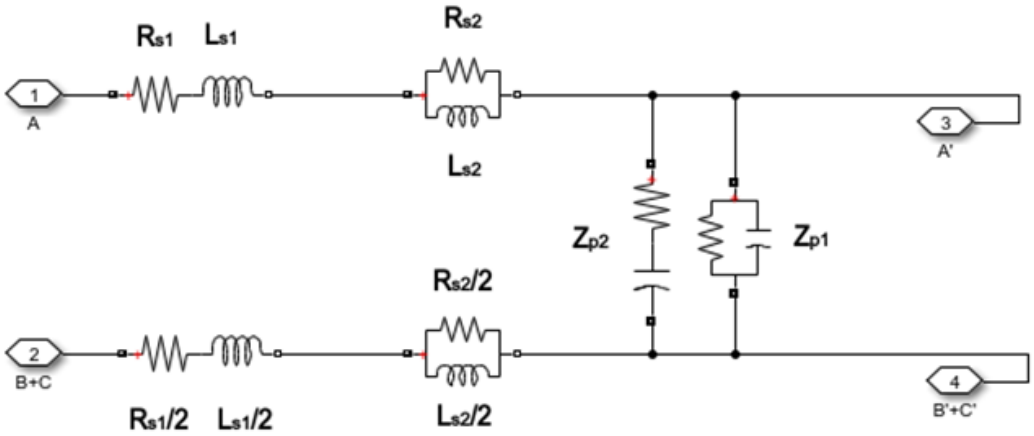

Fig. 58. 1 m section of the DM cable model.

The parameters for the phase A have been estimated and then DM connection has been applied. The equivalent longitudinal parameters of phase A (i.e. R_{s1}, L_{s1}, R_{s2} and L_{s2}) are referred to the supply path (i.e. single-phase connection), while the same parameters are divided by two for the return path, since phases B and C are in parallel. R_{s1} and L_{s1} are respectively the equivalent resistance and inductance which model the low-medium frequency behaviour of the cable short circuit impedance, while R_{s2} and L_{s2} are representative of the HF behaviour, where the influence of skin and proximity effects are higher. The transversal parameters (i.e. Z_{p1} and Z_{p2}) dominate the open circuit impedance behaviour and take into account the dielectric losses, the inter-phase capacitance and conductance. The measurements are carried out at 1) open circuit for the estimation of the transversal parameters Z_{p1} and Z_{p2}, and 2) short-circuit for the extraction of the longitudinal parameters. Fig. 59 and 60 show the comparison between the measured DM longitudinal and transversal impedances of a single cable section and the corresponding impedances provided by the model with the estimated impedance parameters. An excellent match is observed for the whole range of the considered frequencies between

the measured data and the fitted ones. Further details on cable topology will be provided in section 4.1.5.

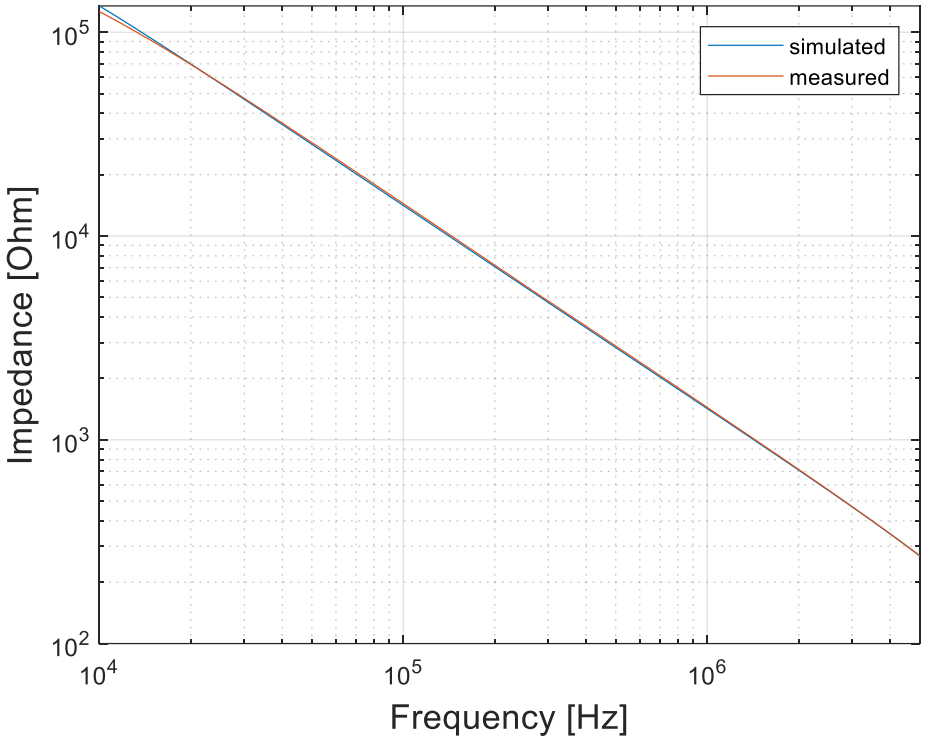

Fig. 59. DM short circuit impedance of 1m cable section- comparison between simulated and measured results.

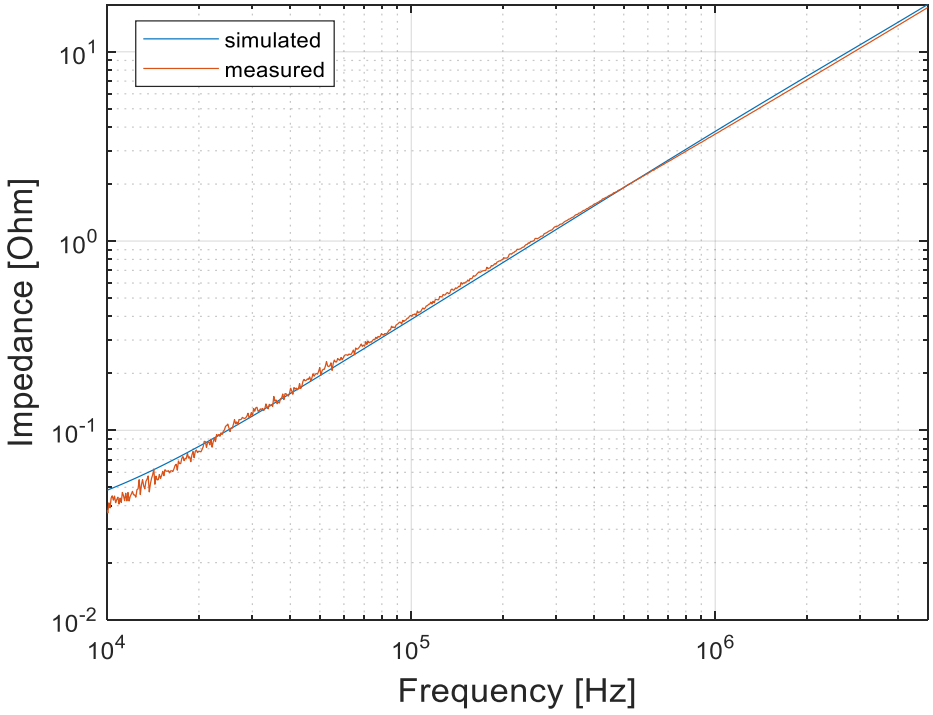

Fig. 60. DM open circuit impedance of 1m cable section- comparison between simulated and measured results.

4.1.3.3 ELECTRICAL MACHINE

The machine equivalent circuit model is taken as that of fig. 61 [68] due to its ease of implementation. The equivalent parameters have been calculated similarly to the methods adopted for the cable, starting from impedance measurement in the low-to-high frequency range and following the procedure detailed in [78]. The machine parameters are L_d, R_e, R_t, L_t, C_t, R_{g1}, C_{g1}, R_{g2} *and* C_{g2}. L_d represents the stator winding leakage inductance; R_e is the equivalent resistance which takes into account the ferromagnetic losses; R_t, L_t, C_t are necessary to capture the HF resonances; R_{g1}, R_{g2}, C_{g1} *and* C_{g2} are the parasitic impedances towards the stator frame and influence the CM behavior of the machine. After estimation of these equivalent parameters, a DM connection is applied for both verification of the impedance as a function of frequency and for time domain overvoltage simulations. The frequency DM response can be observed in fig. 62, where again a very good match between simulated and measured results can be appreciated. However, some discrepancies can be observed above 1 MHz, probably due to possible inaccuracies at very HF, where the equivalent parasitic impedances can become comparable to the parasitic impedances of measurement apparatus.

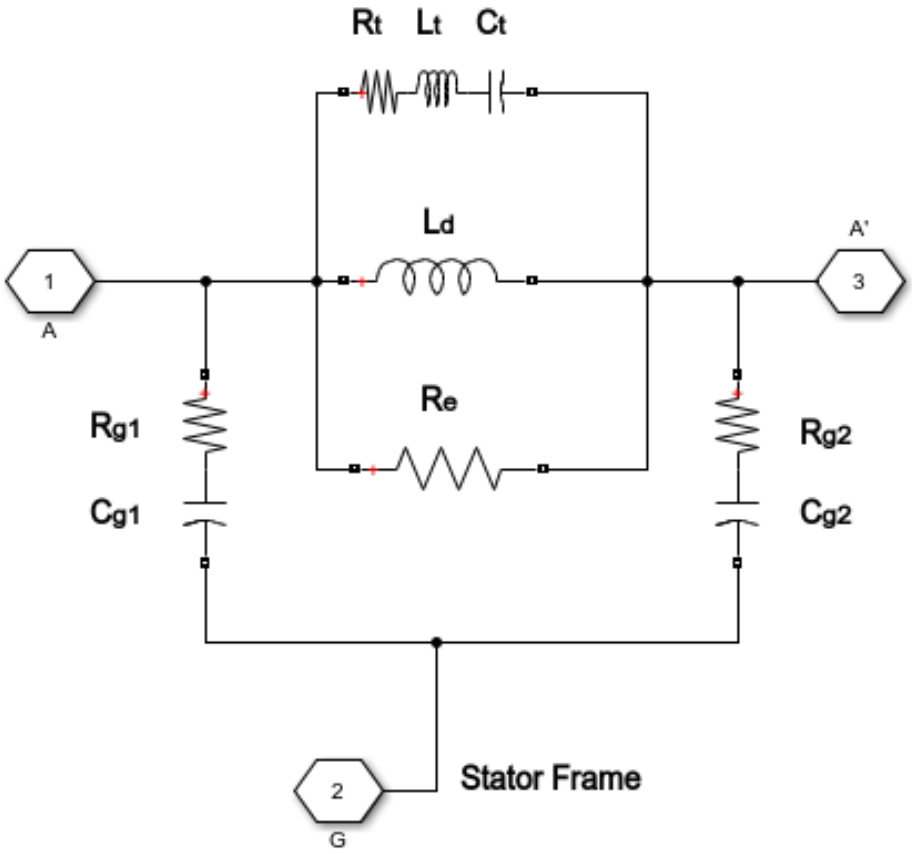

Fig. 61. Single phase HF model of the electrical machine.

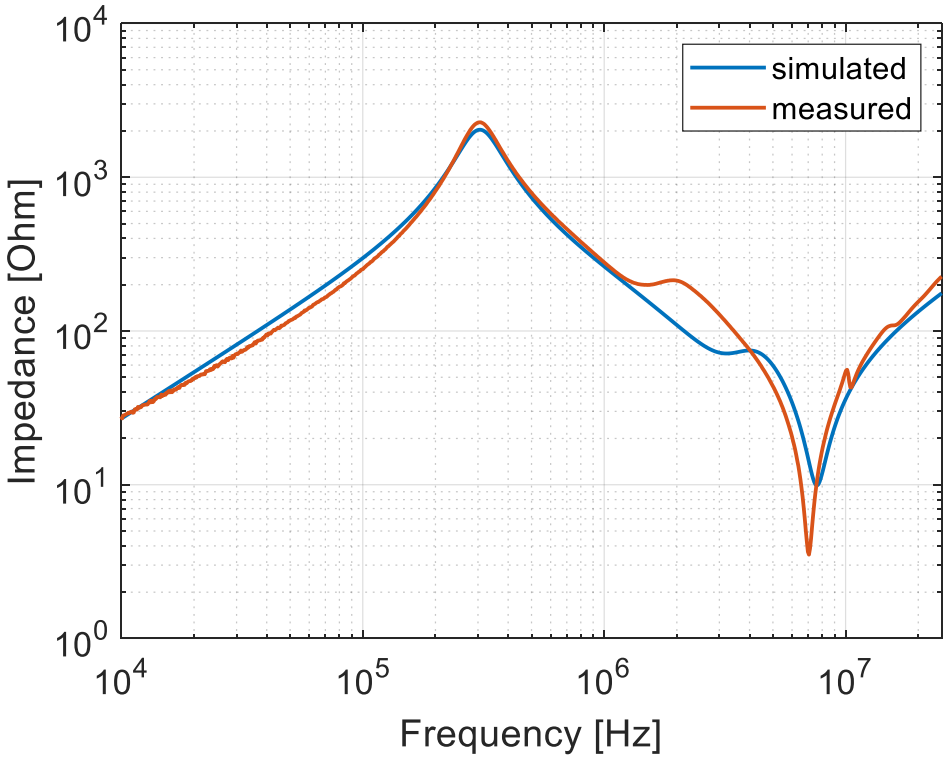

Fig. 62. DM impedance of the electrical machine – comparison between simulated and measured results.

4.1.4 VOLTAGE DISTRIBUTION MODEL

Under steady-state voltage conditions the voltage distribution in a winding is linear and the interturn voltages are low or absent. Under steep-fronted transient voltage conditions the voltage distribution is non-linear and the interturn voltages can be very high. Hence, the interturn winding insulation has to be designed to withstand the stresses caused by HF transient voltages.

While for system-level studies it is sufficient to model the component as a black-box model, when the internal transient response is required, a much more detailed model in which all regions of critical dielectric stress are identified needs to be used. Internal transient response is a result of the distributed electrostatic and electromagnetic characteristics of the windings. For a steep-fronted voltage surge, most of the wave front will reside across the first few turns, which can be overstressed. The wave front slopes off and the amplitude is attenuated as the wave penetrates along the winding. For all practical winding structures, this phenomenon is relatively complex and can only be investigated by constructing a detailed model and carrying out a numerical solution for the transient response and frequency characteristics in the regions of concern. An accurate model may consider each turn of the winding represented by capacitances, inductances

and resistances [71], [72]. Winding capacitances play a vital role in establishing the initial voltage distribution along the winding when a steep-fronted voltage is suddenly applied. Under these conditions, displacement currents can flow in the winding capacitance, but they cannot flow in the winding itself because of its inductance.

4.1.4.1 ASSUMPTIONS

The machine winding consists of a chain of series-connected coils that are distributed around the machine stator. Under steep-fronted transient conditions, the effective self-inductance of a coil differs considerably from the 50 Hz value. Initially, the self-inductance arises from flux that is confined mainly to paths outside the high-permeability iron core by eddy currents that are set up in the core by the incident surge. The reluctance of the flux paths changes as the flux penetrates into the core. Similar considerations apply to the mutual coupling between coils. However, due to the limited extent of flux penetration into the core, the flux linkage from one coil to a coil in a neighbouring slot is very small, so the mutual coupling between coils under surge voltage conditions is also very small. The capacitance between coils is very low because each coil is embedded in a slot which acts as a grounded boundary. The inter-coil capacitance is usually limited to that in the line-end coil and is very small too. However, due to the fact that the coil is embedded in the slot, the coil-to-ground is significant [86].

Considering all the above, the following assumptions can be made when deriving the equivalent circuit of a machine winding:

- The behaviour of the core iron is like that of a grounded sheath and the slot iron boundary may be replaced by a grounded sheath, which is impenetrable to HF waves.
- The series inductance and resistance of the coils are frequency dependent due to the eddy currents in the core and to the skin effect in conductors.
- Only transverse electromagnetic (TEM) propagation mode is considered, so the theory of multi-conductor transmission lines can thus be applied [86].
- The basic unit in the equivalent circuit for the winding is a coil. A stator coil occupies two distinct regions of the machine: 1) the slot region, in which the active coil sides are placed inside the slots in the magnetic core structure and 2) the overhang region, in which the end turns are positioned in air.
- A multi-conductor transmission line model, composed of a number of conductors equal to that of the coil turns, should be considered for each region. As a result,

the coil should be comprised of a series of five transmission lines with discontinuities at the junctions between the lines. The five interconnections constitute five discontinuities for wave transits: four are due to the iron/air interfaces and the fifth due to interruption of an end-winding section by the coil terminals.

- The two opposite overhang parts of the stator core are considered uncoupled because eddy-currents in the core provide effective shielding at high frequencies.
- Overhang and slot parts are also uncoupled because of the eddy current in the core.
- The two parts of the coil at the coil entry are uncoupled since they are nearly perpendicular to each other over most of their length and are further shielded from each other by eddy currents in adjacent coils.
- Insulation between the lamination permits magnetic coupling to the coils inside adjacent slots. However, the two slot parts of the coil are not coupled because of the eddy current in the neighbouring coils.
- Coupling between adjacent coils of different slot layers has a lower effect than the coupling between adjacent turns.
- The capacitive couplings between coils of one phase winding, and between coils of different phase windings, are very small and are thus neglected.
- The capacitance between turns in a coil and between the coil and the core are important and should be taken into account.

In conclusion, each turn of the coil may be modelled as a single conductor transmission line coupled to its adjacent turns.

4.1.4.2 LUMPED PARAMETER CIRCUIT

An accurate representation of the winding for determining the inter-turn voltage distribution should be based on a multi-conductor transmission line with uniformly distributed and frequency-dependent parameters. Nevertheless, a distributed-parameter winding model may be very time consuming and for many practical cases this detailed model can be reduced by lumping series elements within an active side of a single turn and shunt elements between active sides of different turns. Therefore, the active side of a single turn can be represented by series resistances (i.e. $R_{i,i}$) and inductances (i.e. $L_{i,i}$) with mutual inductances between turns (i.e. $L_{i,j}$), and parallel (i.e. C_{ig}) and series (i.e. $C_{i,j}$) capacitances arranged as in fig. 61. Resistances in parallel to these capacitances should

be also included in such a network to model the dielectric losses accurately. Representing accurately these losses can require a rather complicated model, which should also address the frequency-dependent characteristic of the losses. However, when conventional impulse waves are applied, the peak voltage normally occurs on the first major oscillation and the error incurred by not modelling the winding loss is rather small. For these reasons, this study is carried out without including the loss model.

As previously mentioned, the complete coil model should be represented by five sections. However, considering all the assumptions listed above, all of the 3D effects are neglected in first approximation and therefore the whole model coincides with that shown in fig. 61. Additional reduction of the network may not yield useful results for transient voltage investigations.

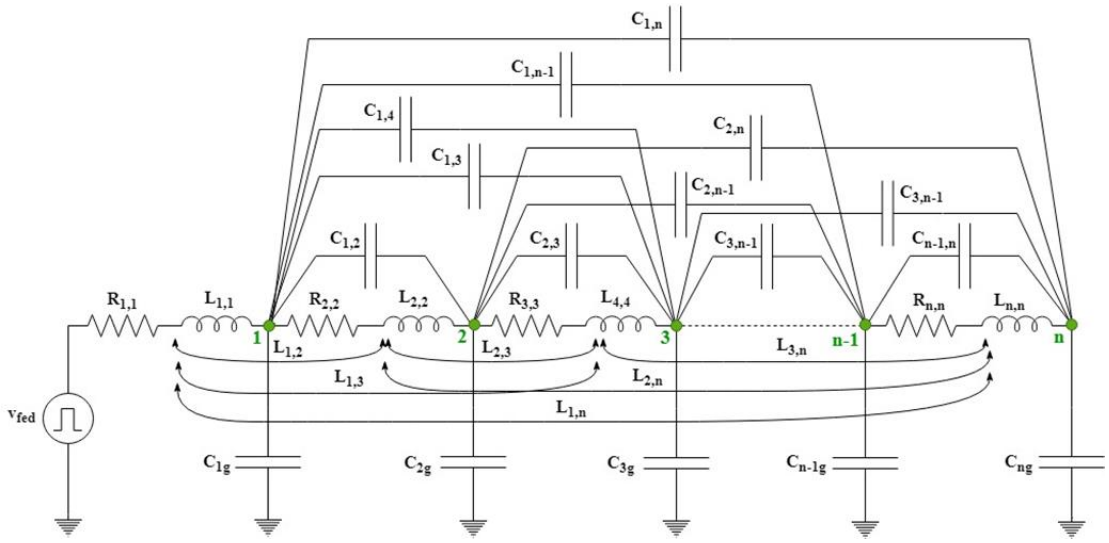

Fig. 63. Equivalent lumped-parameter circuit of a machine coil.

It is clear that any electrical circuit software can be used to solve the network of fig. 63, however this would be manageable only when the number of nodes is limited and, most importantly, it would not be flexible since a different network should be built every time the number of nodes (i.e. the number of conductors in the slot) needs to be modified. Hence, the lumped-parameter model should be solved using any numerical tool irrespectively of its number of elements and nodes. This is done by first developing the state-variable formulation which can be used to approximate the behaviour of a machine winding in HF transients, and then by implementing the obtained expressions in MatLab Simulink environment. Referring to the circuit of fig. 63, only the input voltage v_{fed} is known and it corresponds to the surge voltage feeding the winding. At any node *i* of the network made of *n* nodes, the Kirchhoff's current law can be applied thus obtaining (47).

In (47), i_i and i_{i+1} indicate the currents entering the nodes *i* and *i+1* respectively, v_i is the voltage across C_{gi} and v_k that across all of the C_{ik} comprised in the circuit, with $k \neq i$ and ranging from 1 to *n*.

$$i_i - i_{i+1} - C_{ig}\frac{dv_i}{dt} - \sum_{\substack{k=1 \\ k\neq i}}^{n} C_{i,k}\frac{d(v_i - v_k)}{dt} = 0 \qquad (47)$$

Always referring to the circuit of fig. 63, the Kirchhoff's voltage law can be applied to any loop including two adjacent node-to-ground capacitances, i.e. $C_{i,g}$ and $C_{i+1,g}$, and the series parameters Ri,i and $L_{i,i}$. The expression (18) is thus obtained and provided below. The Kirchhoff's voltage law needs to be used also for the additional loop including v_{fed}, $R_{i,i}$, $L_{i,I}$ and C_{1g}, thus resulting still in (18), if one assumes that when $i=1$, then $v_{i-1}=v_{fed}$.

$$v_{i-1} - v_i - R_{i,i}i_i - L_{i,i}\frac{di_i}{dt} - \sum_{\substack{k=1 \\ k\neq i}}^{n} L_{i,k}\frac{di_k}{dt} = 0 \qquad (18)$$

From (47) and (18), it can be noticed that the system state variables are the currents entering in each node and the voltages across the node-to-ground capacitances of the network. To tidily group the state variables in two independent vectors, namely $\bar{\mathrm{i}} = (\mathrm{i}_1 \quad \mathrm{i}_2 \quad \ldots \quad \mathrm{i}_n)^{\mathrm{T}}$ and $\bar{\mathrm{v}} = (\mathrm{v}_1 \quad \mathrm{v}_2 \quad \cdots \quad \mathrm{v}_n)^{\mathrm{T}}$, (47) and (18) can be firstly elaborated as in (49) and (50), respectively.

$$i_i - i_{i+1} = \left(C_{ig} + \sum_{\substack{k=1 \\ k\neq i}}^{n} C_{i,k}\right)\frac{dv_i}{dt} - \sum_{\substack{k=1 \\ k\neq i}}^{n} C_{i,k}\frac{dv_k}{dt} \qquad (49)$$

$$v_{i-1} - v_i = R_{i,i}i_i + L_{i,i}\frac{di_i}{dt} + \sum_{\substack{k=1 \\ k\neq i}}^{n} L_{i,k}\frac{di_k}{dt} \qquad (50)$$

After a few manipulations, the final expressions can be written in the state form given in (51) and (52). Here, $\boldsymbol{C_{sw}}$ is a matrix of capacitances having the terms $\mathrm{C_{ig}} + \sum_{\substack{\mathrm{k=1} \\ \mathrm{k\neq i}}}^{\mathrm{n}} \mathrm{C_{i,k}}$ on its main diagonal and all the terms $-C_{i,k}$ in the corresponding positions *i,k* of the matrix, $\boldsymbol{R}$ is a diagonal matrix whose elements are the series resistances $R_{i,i}$, $\boldsymbol{L}$ is the matrix having self-inductances $L_{i,i}$ on the main diagonal and mutual-inductances $L_{i,k}$ in the corresponding positions *i,k*. In (51) and (52), to achieve the state form and to allow for a compact description of the equations, the vector $\overline{\mathrm{v_{fed}}} = (\mathrm{v_{fed}} \quad 0 \quad \ldots \quad 0)^{\mathrm{T}}$ and the matrix $\boldsymbol{D}$ are newly introduced. The latter matrix has all the elements of the main diagonal equal to -1, all the elements in the first sub-diagonal equal to 1 and all of the remaining elements equal to 0. The above equations are implemented in Matlab-Simulink environment, while

the values of all of the elements included in the matrices $\boldsymbol{R}$, $\boldsymbol{L}$ and $\boldsymbol{C_{sw}}$, are determined through 2D finite element (FE) modeling of one machine slot. Their detailed description is provided in the next section.

$$\frac{d\bar{v}}{dt} = \boldsymbol{C_{sw}}^{-1}\left(-\boldsymbol{D}^{T}\,\bar{\imath}\right) \tag{51}$$

$$\frac{d\bar{\imath}}{dt} = \boldsymbol{L}^{-1}\left(\overline{v_{fed}} + \boldsymbol{D}\,\bar{v} - \boldsymbol{R}\,\bar{\imath}\right) \tag{52}$$

4.1.4.3 FE MODELS

Given the complexity associated to an eventual analytical determination of resistances, inductances and capacitances, a FE analysis is chosen as means to do so. Considering all the assumptions and hypotheses described above, only one slot pitch is modelled. The electric field simulation software ElecNet is used to find the capacitances, whereas the low-frequency electromagnetics simulation software MagNet is employed for resistances and inductances. Apart from some differences inherently related to the nature of the problems, most of the pre-processing and solving features (such as creation of the geometry, assignment of materials, meshing and simulation parameters, types of solvers, etc.) are common to both software. The one slot pitch models comprise all the relevant elements necessary for the analysis, including the slot itself, two half teeth, conductors, enamel, interturn insulation and slot liners.

According to the considerations carried out in 4.1.4.1, the slot acts as a grounded boundary at high frequencies. In ElecNet, the "ground" boundary condition is available and thus this is applied to the modelled slot, which thus represents an electrically grounded conductor, where the electric potential is constrained to zero. As a result, the electric field is made normal to the boundary. To specify the voltage over a component, the latter has to be changed to an electrode. All the conductors built within the model are thus changes to electrodes. Finally, before selecting the most suitable solver and then running the simulation, the mesh needs to be defined. First, it is worth mentioning that electrodes are nor meshed, as there is no need to calculate the potential or the electric field inside it. The grounded slot is considered as an electrode with 0 V, meaning that also this component is not meshed. All the rest of the components are meshed in such a way to achieve high accuracy in the main areas of interest. Hence, focus is given to the components within the slot, i.e. all the insulations, whereas a less dense mesh is used for the areas surrounding the slot. A 2D solution mesh and the electric field distribution are shown in fig. 64 a) and fig. 64 b) respectively, where some of the modelling aspects

described above can be observed. With the definition of the mesh, the model is fully defined and is ready for the solution. The time-harmonic solver is chosen as the most suitable for the sake of this study. The time-harmonic simulations are performed at one specified frequency, and sources and fields are represented by complex phasors. A first evaluation is carried out by imposing a voltage equal to 10 V to any of the *n* conductors (electrodes), keeping at 0 V all the other *n-1* ones. In this way, after the solution is ready, the self-capacitance (i.e. the node-to-ground capacitance C_{ig}) and the mutual-capacitances between the *i-th* electrode and all of the other

n-1 ones (i.e. the turn-to-turn capacitances $C_{i,k}$, with $k=1,\ldots,n$ and $k\neq i$) are calculated through phasorial analysis. It is worth mentioning that, after completing this set of FE evaluations, the determined capacitances have to be first stored and then manipulated in Matlab in such a way to obtain the matrix $\boldsymbol{C_{sw}}$ necessary for the numerical resolution of the assumed lumped-parameters circuit assumed.

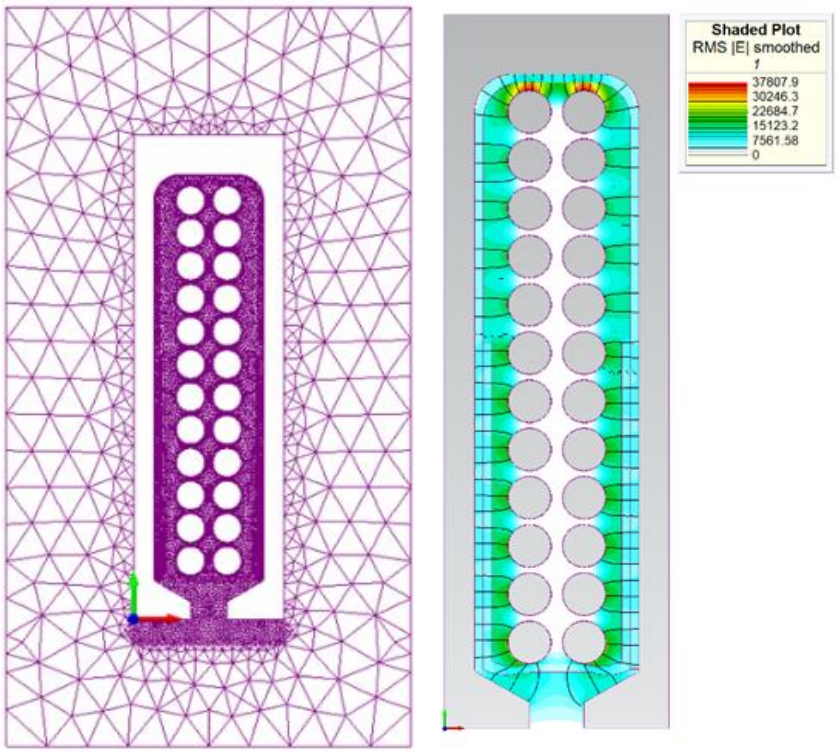

(a) **(b)**

Fig. 64. a) solution mesh and b) electric field distribution of the 2D FE slot pitch model developed in ElecNet.

Keeping in mind that all the steps relative to the geometry creation and the material assignments are also valid for the electromagnetic FE analysis with MagNet, all the rest of the modelling passages necessary to finally calculate the circuit resistances and inductances is detailed in this sub-section. In MagNet, each modelled conductor needs to be defined as a coil comprising 1 turn. These *n* coils are all modelled as “solid”, allowing

to accurately take into account the potential non-uniform current distribution occurring at HF, thus guaranteeing the correct estimation of the resistances.

As well as for the electric field simulation analysis, a suitable solution mesh is defined before solving. In this case, the main areas of interest also involve the conductors (coils). This concept can be seen in the solution mesh reported in fig. 65 a). Time-harmonic solutions are employed also for the FE evaluations in MagNet. The magnetic field distribution is shown in fig. 65 b). To determine the resistances and the inductances of the equivalent circuit under study, a first evaluation is carried out by imposing a current equal to 1*A* to any of the *n* conductors (coils), keeping at 0*A* all the other *n-1* ones. In this way, after the solution is ready, the terms $R_{i,i}$ and $L_{i,i}$ and the mutual-inductances between the *i-th* coil and all of the other *n-1* ones (i.e. the inductances $L_{i,k}$, with $k=1,\ldots,n$ and $k\neq i$) are calculated through phasorial analysis. It is worth mentioning that, after completing this set of FE evaluations, the determined circuit parameters have to be first stored and then manipulated in Matlab in such a way to obtain the matrices **R** and **L** necessary for the numerical resolution of the assumed equivalent circuit.

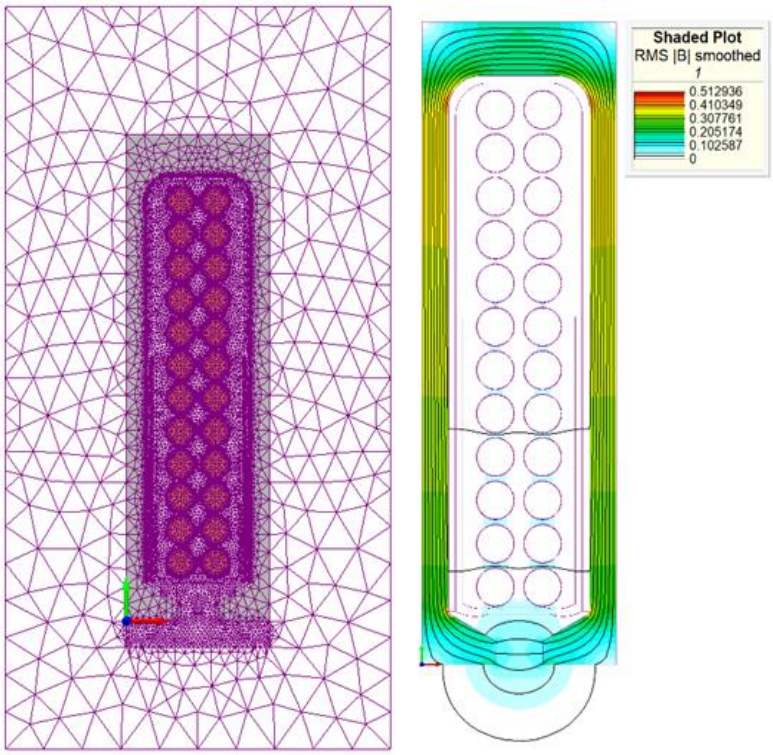

(a) **(b)**

Fig. 65. a) solution mesh and b) magnetic field distribution of the 2D FE slot pitch model developed in MagNet.

4.1.4.4 SUMMARIZING REMARKS

The whole automated process is coded in Matlab and the relevant steps, ranging from the definition of the geometrical dimensions to the solution of the dynamic system, are provided below:

1) The characteristic design parameters, such as slot dimensions, number of conductors, slot and conductor insulation thicknesses, etc. are defined in Matlab.
2) Matlab launches ElecNet, where the slot pitch model is built and simulations are performed to determine the capacitances.
3) Matlab launches MagNet, where the slot pitch model is built and simulations are performed to determine resistances and inductances.
4) The calculated equivalent circuit parameters are elaborated in Matlab in such a way to obtain the matrices $\boldsymbol{R}$, $\boldsymbol{L}$ and $\boldsymbol{C_{sw}}$ needed for the system resolution.
5) The input parameters are defined for the voltage source v_{fed}.
6) Matlab launches Simulink, where the dynamic system model is built and the simulation is run, thus finding the state variables, i.e. 1) turn currents and 2) node voltages.
7) Matlab post processes the results by plotting the obtained state variables.

4.1.5 CASE STUDY

The benchmark case study is a high-performance electric drive intended for more electric aircraft applications. The basic structure of the system consists of an AC-DC converter directly connected to the on-board voltage supply, i.e. 230V AC at 360-800Hz, a DC-AC converter, with a DC-link voltage of 564V, which supplies via appropriate cabling a speed controlled electrical machine. The inverter is connected to the motor via a 6 m three core cable using wire based on SAE AS 22759/41, with a diameter of 8AWG, twisted triple, single shielded (Nichel-coated copper), single jacket. Finally, the electrical machine has a rated continuous power of 5.7kW and is intended for continuous hydraulic power supply applications. It features an 8-poles, interior permanent magnet (IPM) rotor and a 36-slots stator, with a double-layer, integer-slot, three-phase winding comprising 3 coils-per-pole-per-phase, each consisting of 12 turns. Table IX summarizes the main characteristics of the electric drive under analysis.

The real shape of the benchmark stator slot is characterized by a trapezoidal layout, as typical in low power machines. On the other hand, the slot geometry assumed by the FE models is implemented by considering parallel sides for the sake of simplicity. In other

words, a constant slot width is considered and this is taken equal to the mid-segment of the trapezoid. Hence, the slot liners follow the parallel profiles of the slot sides. Apart from these adjustments, all the rest of the dimensions are identical to the benchmark machine. Regarding the conductors, the effective number of turns, i.e. 12 turns per coil, is considered. The rest of the phase turns is modelled through a lumped RL impedance as the interturn voltages are particularly significant on the first turns only.

Table IX. ELECTRIC DRIVE MAIN CHARACTERISTICS

Machine	Slots	36
	Poles	8
	Rated Power	5.7 kW
	Rated Voltage	230 V
	Frequency Range	360 - 800 Hz
Converter	DC Bus Voltage	564 V
	SiC MOSFETs rating	900*V*, 11*A*
Cable	Length	6 m
	Topology	8 AWG Tripolar Shielded

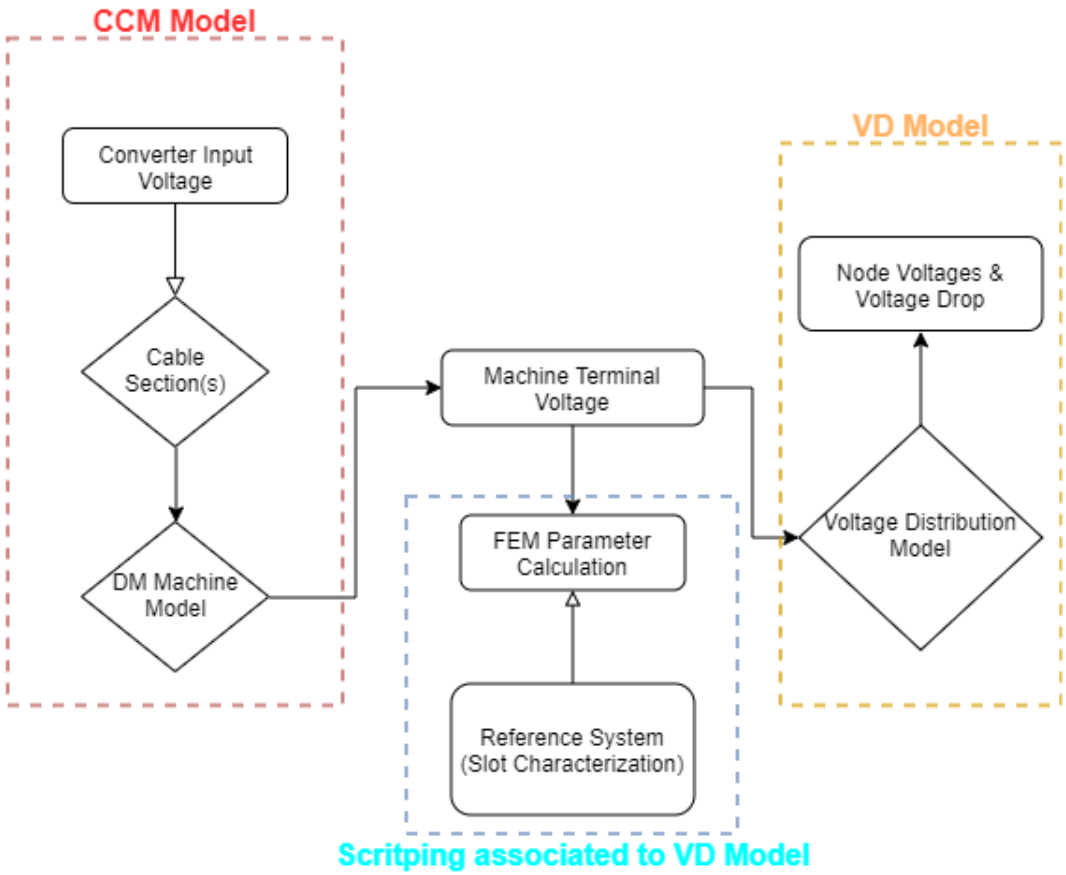

Fig. 66. Simplified flow chart of the whole system model (i.e. merging of the two models).

As highlighted above, the development of a comprehensive model able to estimate both over-voltages at the machine terminals and voltage distributions within windings represents the main contribution of this paper. So far, the two models have been developed and implemented separately. However, their inherent flexibility allows for a straightforward merging and an easy and automatic communication within MatLab environment. The converter-cable-machine model estimates the voltage waveform at machine terminals, thus including overshoot and rise time. The latter is used to calculate the frequency at which the equivalent circuit parameters should be computed via FE analysis [87], while the terminal voltage waveform is used as input (i.e. v_{fed}) for the voltage distribution Simulink model, thus allowing to compute node currents and voltages. The node voltages represent the turn-to-ground voltages which can be then post-processed to determine the interturn voltages. Fig. 66 shows a simplified flow chart illustrating how the merged models (indicated as CCM, i.e. converter-cable-machine, and VD, i.e. voltage distribution) operate.

4.1.5.1 PRELIMINARY RESULTS AND CONSIDERATIONS

Some preliminary simulations can be performed to assess the system behaviour. For the given case study, a first investigation assumes that the converter output is as in fig. 67 (blue waveform), i.e. a voltage ramp with an amplitude of 564 V and gradient equal to 20 kV/µs (rise time about 23 ns). Fig. 67 also shows the estimated voltage at the machine terminals, in red, featuring an overshoot nearly twice the converter output voltage amplitude (i.e. the DC link bus voltage) and a rise time t_r=28 ns. This results in a supply frequency of $0.35/t_r$=12.5MHz being used for FE determination of resistances, inductances and capacitances. Since the voltage at motor terminals is the result of the sum of an incident and reflected wave (which can be considered at first approximation as two first order responses), the supply frequency is computed basing on the bandwidth of a first order response. The resulting voltage distribution is obtained and reported in fig. 68 for the first three turns, which are the most significant, proving that the voltage within windings is rather unevenly distributed.

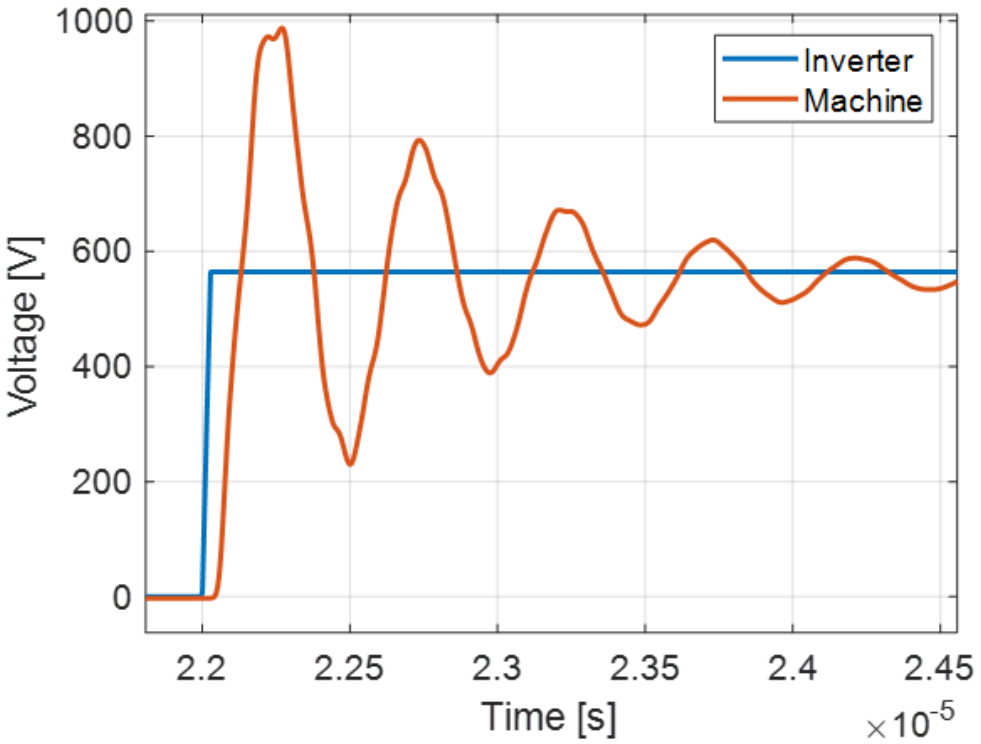

Fig. 67. Machine line-to-line voltage (in red) ensuing from an inverter output voltage (in blue) of 564 V amplitude and 23 ns rise time.

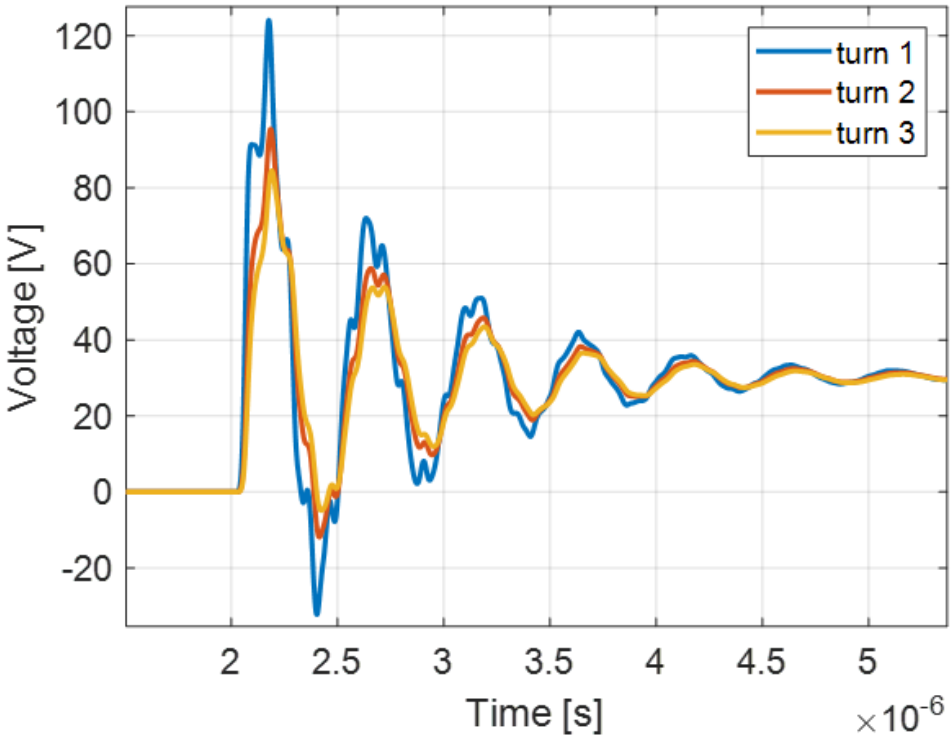

Fig. 68. Voltage drop across the first three winding turns.

4.1.6 EXPERIMENTAL RESULTS

The aim of this section is to prove that the validity and the accuracy of the proposed model by comparing the relevant results against experimental measurements carried out on a purposely-built prototype. First, the description of the experimental setup is provided and then then validation exercise is detailed.

4.1.6.1 EXPERIMENTAL TEST SETUP

A DC power supply unit (PSU) is used to feed an H-bridge converter (fig. 69), which is based on 900*V*, 11*A* SiC MOSFETs. The converter is linked to the electrical machine via a 6 *m* long cable, connected in DM. The motor features some accessible interturn terminals for voltage probing and only the stator is analysed, thus inherently neglecting the rotor effects [87]. A Hall effect probe is used to measure the current and differential voltage probes are used to record the voltages (both at the machine terminals for the

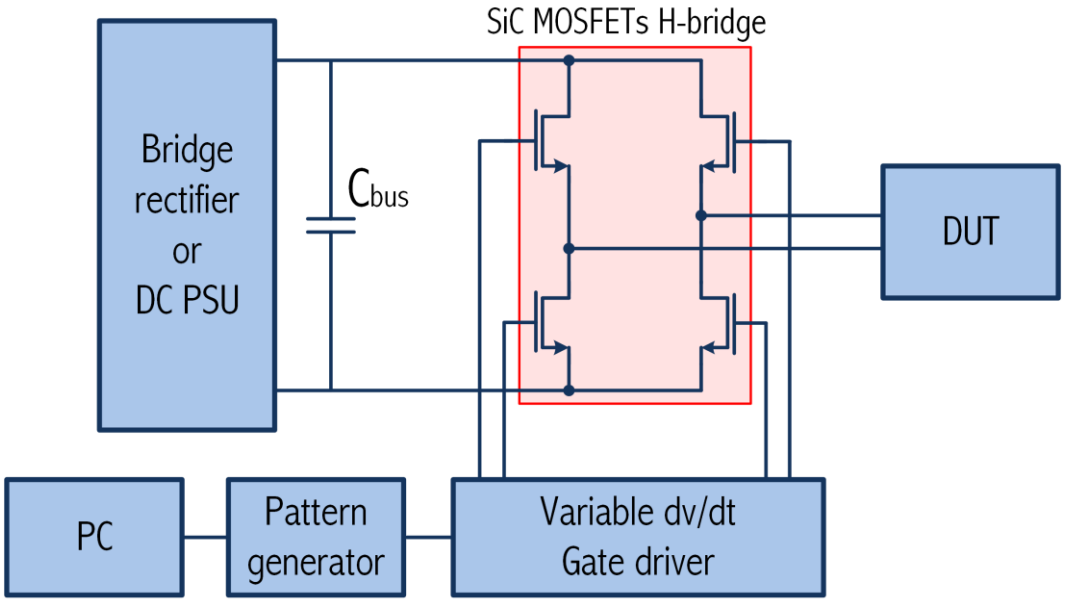

Fig. 69. Block scheme of the experimental setup.

overshoot validation and at interturn terminals for the voltage distribution validation). The user interface allows to select a unipolar or bipolar output, to modify duty cycle, switching frequency, *dV/dt*, etc. A picture of the most relevant parts of the described setup is reported in fig. 70, showing the system including the SiC converter, the connecting cable and the electrical machine.

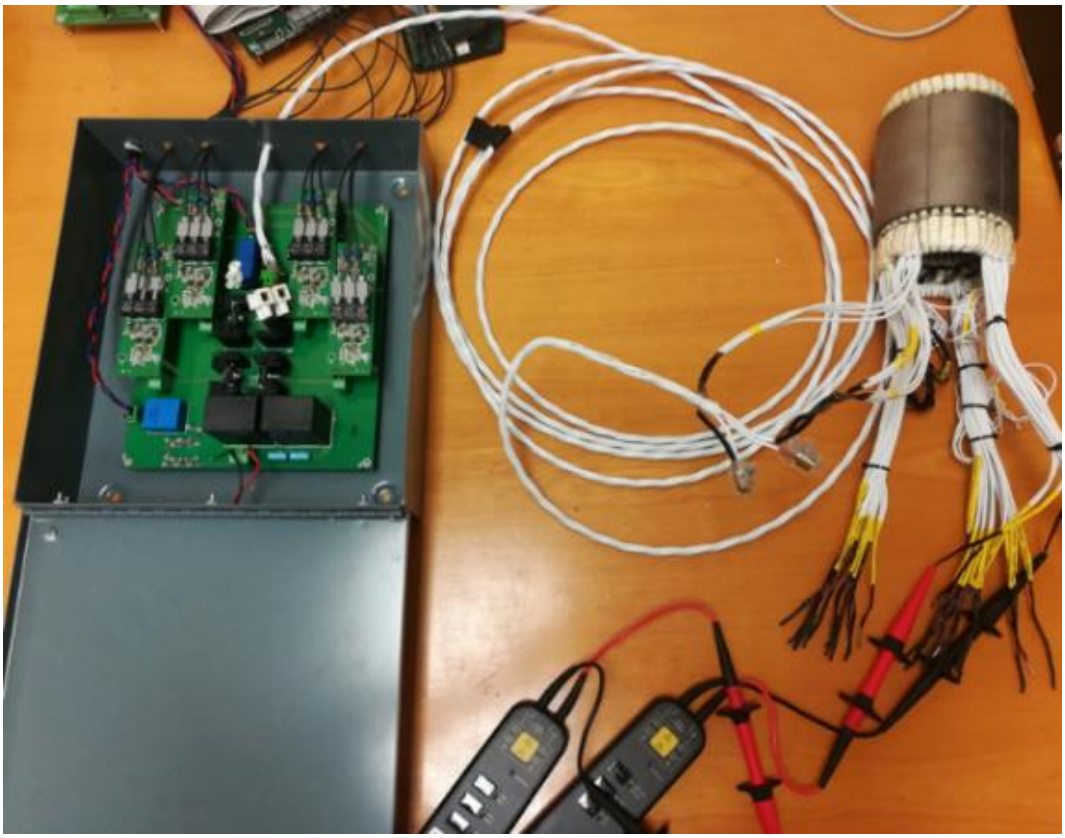

Fig. 70. SiC-based converter, connecting cable and electrical motor with accessible interturn terminals.

Since preliminary investigations have shown that duty cycle and switching frequency do not impact the phenomena under investigation, a bipolar supply at 30*kHz* and 50% duty cycle is used for the whole test campaign. On the other hand, *dV/dt* and voltage levels affect both overshoot and voltage distribution, so the validation exercise will focus on such aspects.

4.1.6.2 MODEL VALIDATION

The experimental measurements for model validation have been carried out at reduced DC link voltage values, in order to keep the current below the limit of the SiC MOSFETs. In particular, tests up to 150 V were possible without overcoming the 11A rating of the WBG devices. In this paper, the results at 100 V and 150 V with bipolar supply are considered. Although the tests are performed at reduced voltage, the rise times of the converter output voltage is only 33 ns at 100 V and 29 ns at 150 V, so that, in the time scale of one transient, the waveforms appear as nearly stepped ones, making the overvoltage and the uneven voltage distribution rather quantifiable. Fig. 71 and 72 show the line to line voltages at 100 V and 150 V, respectively. An excellent match can be

observed, especially considering the peak voltage which is the main quantity for designing an insulation system and for estimating PDIVs.

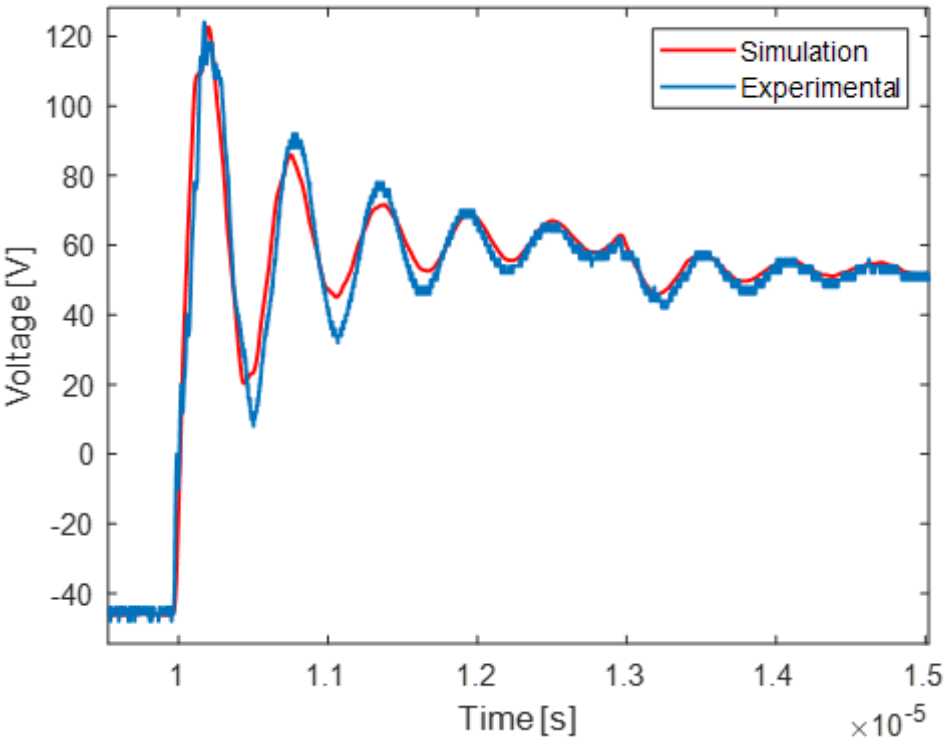

Fig. 71. Line to line DM voltage at motor terminals at 100 V.

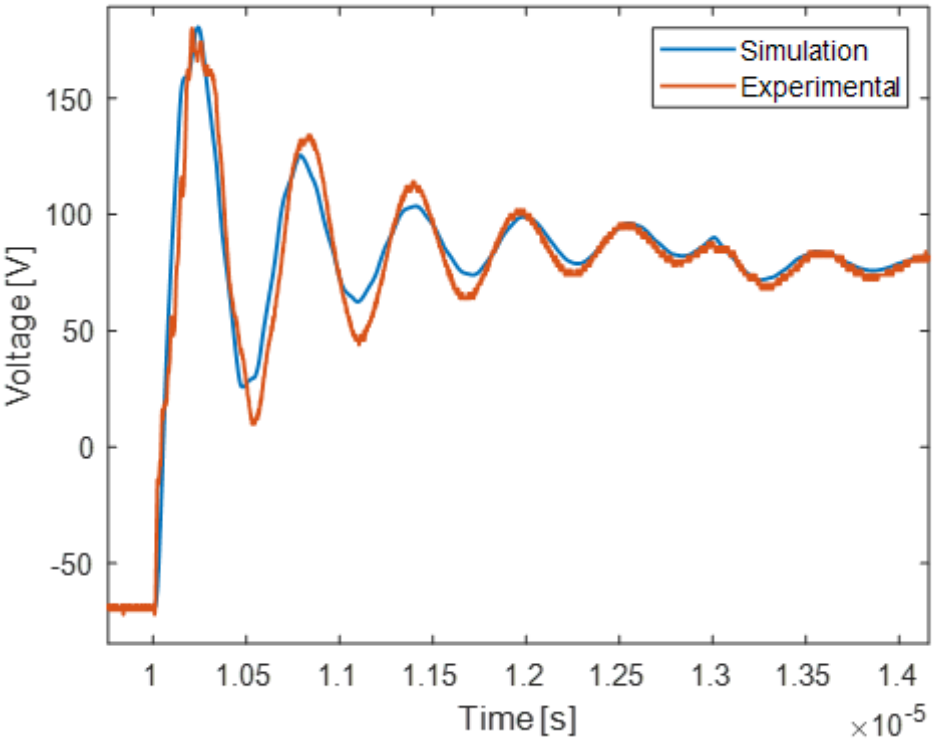

Fig. 72. Line to line DM voltage at motor terminals at 150 V.

The corresponding node voltages are shown in fig. 73-76. In particular, fig. 73 and 74 report the comparison between simulation and experimental node voltages for the 2nd and 6th turns, respectively, when the DC link voltage is set at 100 V. Fig. 75 and 76 show the same comparison at 150 V. Also in this case the match is very good, with a negligible error on the 2nd turn (<2%) and a maximum error of ≈5% on the 6th turn recorded at 150 V. On the other hand, a small discrepancy can be noticed after the first instants of the pulse on both the line-to-line voltage at the machine terminals and the node voltages. This is due to having adopted an approach which neglects the variation of the equivalent parameters with the frequency during the transient. For the same reason there is a little overestimation of the steady-state values due to a slight overestimation of the lumped parameters modelling the last turns. However, the most significant quantities are just the peak voltages at the machine terminals and at its first coil turns, whose values are accurately predicted by the developed comprehensive model.

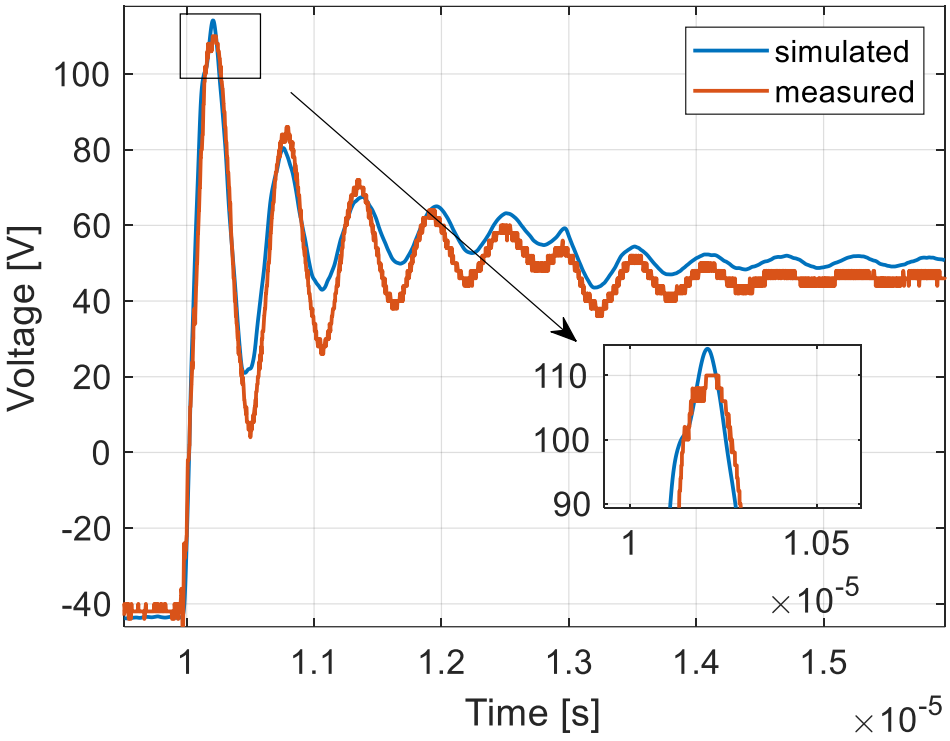

Fig. 73. 2nd turn voltages with 100 V supply.

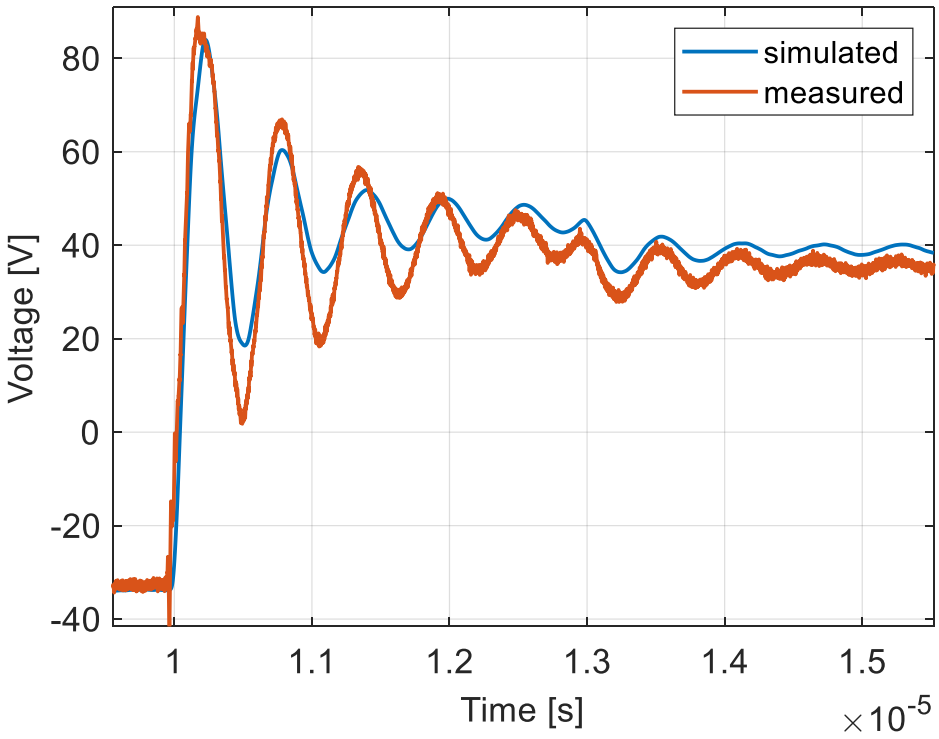

Fig. 74. 6th turn voltages with 100 V supply.

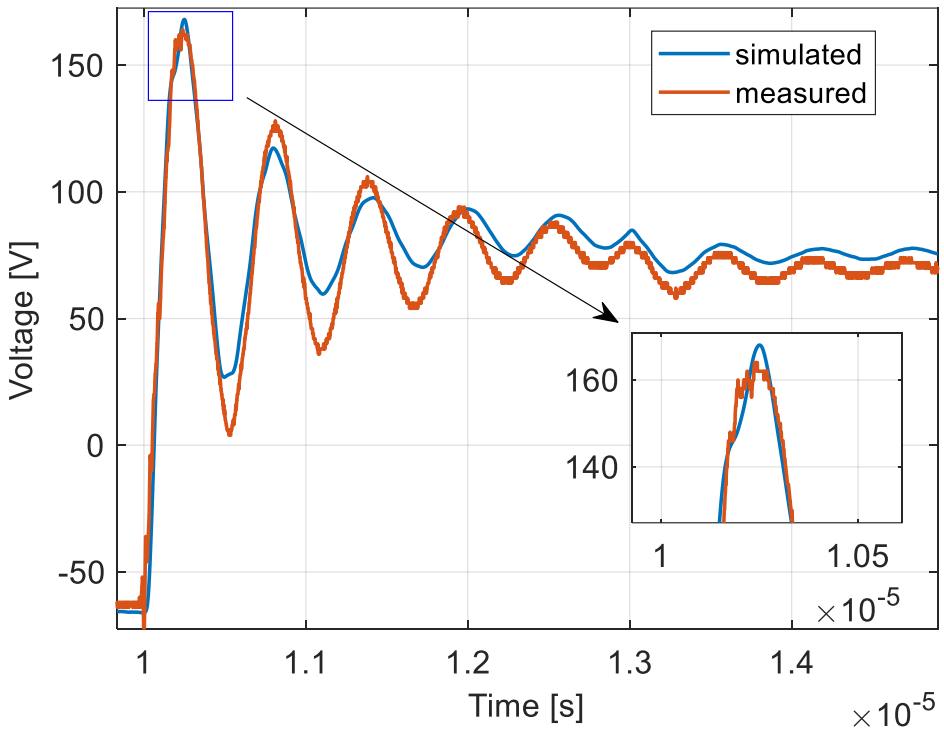

Fig. 75. 2nd turn voltages with 150 V supply.

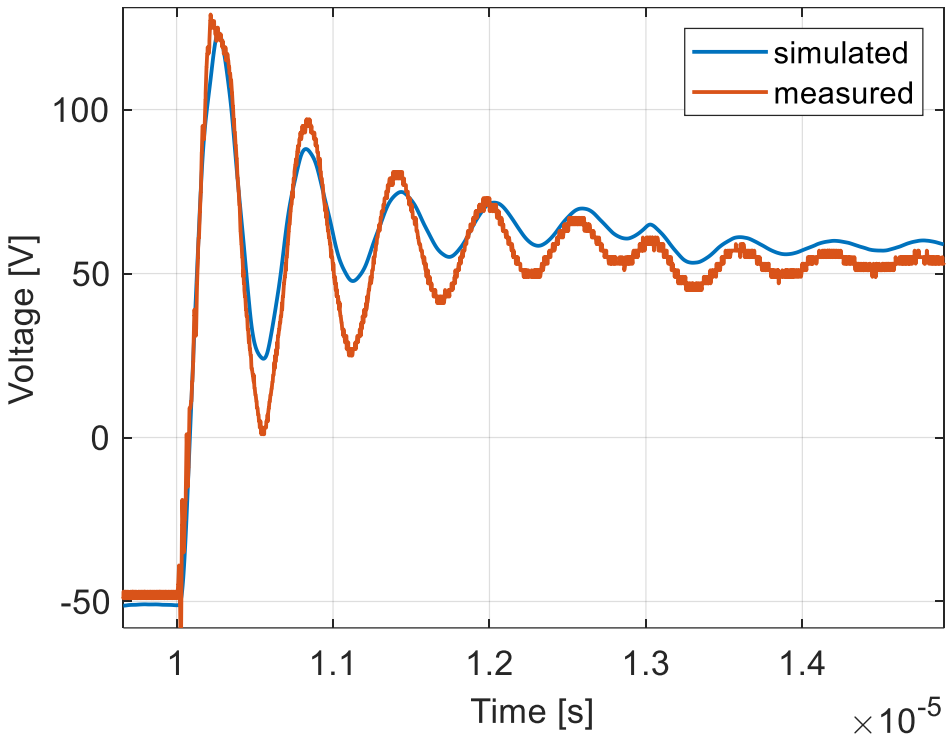

Fig. 76. 6th turn voltages with 150 V supply.

4.1.7 CONCLUSIONS

Section 4.1 has dealt with a modelling approach for the comprehensive analysis of voltage stress in electrical drives fed with a short rise time VSIs. In particular, the overvoltage at the machine terminals and the voltage distribution within windings were estimated simultaneously via such a comprehensive tool, which was implemented by merging the converter-cable-machine model with the winding voltage distribution one. The two models and their initial separate development were described in detail, highlighting assumptions, approaches, preliminary results and limitations. A case study was considered to investigate the model validity and accuracy. Experimental results were performed on a complete system comprising a SiC converter, a connecting cable and a machine stator, proving the simulation model accuracy in terms of peak voltages of both the line-to-line terminal voltage and the turn voltage distribution across the first turns, which are the most relevant quantities for the sake of this study as well as for the investigations of partial discharges.

While the model was developed and validated for classical random windings with round wires, the approach can be generalised and applied to electrical machines with HWs,

which represent the main case study of this thesis. The relevant studies, developments and results will be described in the next section.

4.2 INVESTIGATION OF VOLTAGE DISTRIBUTION WITHIN HWS FED BY WBG DEVICES

This section is focused on the study of the voltage distribution within hairpin conductors for traction applications. The main differences with the previous analysis are the following:

- In traction application the inverter is close to the motor, thus the overvoltage at machine terminals is lower compared to other applications and represents a minor issue. On the other hand, the small filtering action provided by the cable is really low, resulting in a shorter rise time waveform at the machine terminals. In addition, as shown in the previous section, predicting the voltage distribution is more difficult and needs a more detailed model. For this reason, the following analysis is focused on the internal voltage stress within the windings, rather than the voltage appearing at the machine terminals.
- The exact location of each hairpin conductor is known, making possible both developing a specific winding HF model and finding winding configurations which decrease the peak voltages.

4.2.1 PREVIOUS STUDIES AND MOTIVATION

Some studies have been done in order to reach a better understanding of voltage distribution/internal voltage stress in HWs [95]-[98]. The general approach is quite similar to the one illustrated in section 4.1 and it is typically based on the finite element (FE) extraction of the impedances, and on the simulation of the voltage waveforms in the equivalent HF circuit of the winding (or a portion of it). A particular focus has been given to the influence of the voltage input parameters (amplitude, rise time or *dv/dt*) through some sensitivity analyses [95], [96], and to some possible special connections aimed at reducing the maximum voltage amplitude between adjacent layers [95], [98]. However, more investigations are needed, such as:

1) the influence of winding geometric parameters;
2) the study of the phenomenon in short pitched windings;

3) the study on how to reduce the voltage stress in machines featuring standard and simpler connections, which are more likely to be adopted in a context of large scale and/or lower cost production.

This section is focused on the third point, whereas the first two aspects will be investigated in future researches. Considering the above, the main aims are to present a voltage distribution analysis on a complete HF model of a three-phase winding with standard connections and to investigate the best possible solutions to series connect the different winding paths. The considered machine connections are kept as uniform as possible in order to simplify the realization of the winding, thus no jumps of more than one layer are considered. The main motivation under this assumption is that special connections are not always feasible and they tend to increase the manufacturing complexity, thus some simpler and lower cost alternatives should be also investigated. The main results are then adopted to draw some simple but important guidelines for the realization of HWs with a reduced voltage stress.

4.2.2 CASE STUDY

The considered machine is a dual three-phase PM-assisted synchronous reluctance machine with six conductors per slot and ISDW like the one considered in chapter 3. The only difference is that, for this study, all conductors are hypothesized as identical (no asymmetric configuration). Each phase consists of 4 paths whose terminals can be series or parallel connected. The winding main data are summarized in Table X. For the sake of the voltage distribution study, only one of the two three-phase windings can be considered and the rotor influence can be neglected.

Table X. WINDING PARAMETERS FOR HW VOLTAGE DISTRIBUTION ANALYSIS

Winding topology	ISDW
Slots	96
Slots per pole per phase	2
Slot Conductors	6
Conductor dimensions [mm]	2.8 x 1.8
Phase Paths	4

4.2.2.1 FE MODEL

A 2D FE model is built for the extraction of all the winding impedances, thus a proper mesh and characterization of all the materials is needed. A picture of it can be observed in fig. 77.

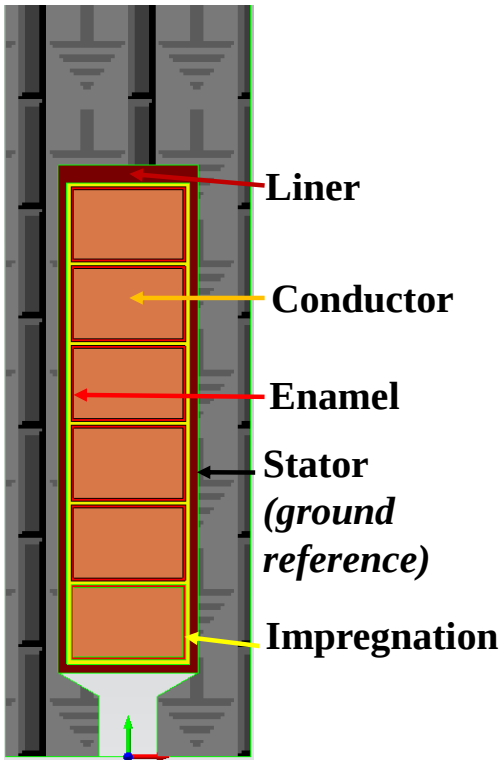

Fig. 77. 2D FE Model of one slot.

The adopted software is Simcenter ElecNet for the capacitances determination and Simcenter MagNet for resistances and inductances. The evaluation of the parameters, which is briefly recalled below, is carried out as illustrated in section 4.1.4, with the exception of the capacitances, which are evaluated as in [95]-[98]. However, all the approaches are valid:

- The capacitances are computed though electrostatic simulations, since they are frequency independent.
- The resistances and inductances can be computed through transient or time harmonic simulations. In this analysis, transient simulations are performed to achieve a better accuracy. The saturation is considered low, which should correspond to the worst case scenario in terms of voltage stress. In fact, the consequently higher inductance should trigger voltage oscillations also at lower frequencies.

- The frequency dependent parameters are evaluated at a fixed frequency f_r, which is chosen according to the input waveform rise time t_r as for the voltage stress analysis in section 4.1.

4.2.2.2 CIRCUIT MODEL

The HF equivalent circuit consists of series and parallel connections of multiple *RLC* impedances. Fig. 78 provides an example of the HF model of a 2-layer slot. R_i and L_i are basically the HF resistances and inductances of the conductor belonging to the i^{th} layer. C_{12} is the capacitance between the two considered adjacent layers, while C_{i0} are the conductor to ground capacitances. The slot walls are considered at the ground potential. The single slot models are identical for a specific machine and should then be connected, according to the number of slots, paths and conductor transposition, in order to realize the HF total impedance of each phase.

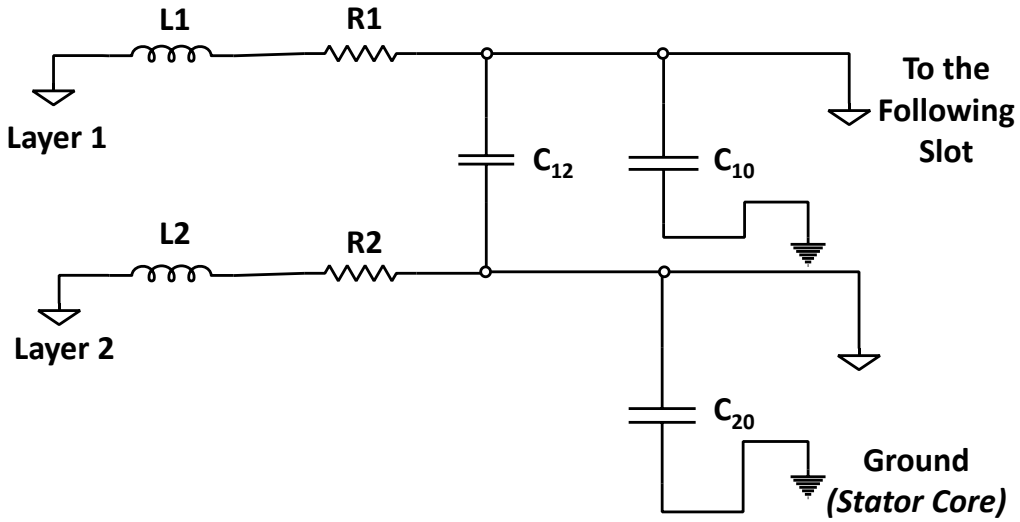

Fig. 78. HF slot model of a 2-layer winding.

4.2.2.3 WINDING CONNECTIONS

Before running the simulations, it is necessary to connect the slot winding models according to the winding diagram. This section illustrates the adopted connections for the realization of each phase path. Fig. 79 shows the winding diagram of one phase. There are four paths:

- Paths 1 (red) and 2 (green) start form the 1st layer of slots 1 and 2 respectively, while they end in the 6th layer of slots 86 and 85 respectively. They are wounded clockwise.

- Paths 3 (yellow) and 4 (blue) start from the 6th layer of slots 1 and 2 respectively, while they end in the 1st layer of slot 14 and 13 respectively. They are wounded counterclockwise.
- Each path has the same identical connection topology. There are one short and one long connection at each revolution in order to equally fill all the slots per pole per phase. The connections with the dotted lines, which refer to the welding side, are such that the coil pitch is equal the pole pitch. The solid lines are referred to the insertion side and can have different lengths when it is necessary to change slot per pole from even to uneven indexes or vice versa. However, they are kept as uniform as possible. Hence, only jumps of a single layer have been adopted. Each connection is characterized by a change of layer, and for each revolution two layers are filled. The starting slots have been chosen such that the terminals are kept near to each other.

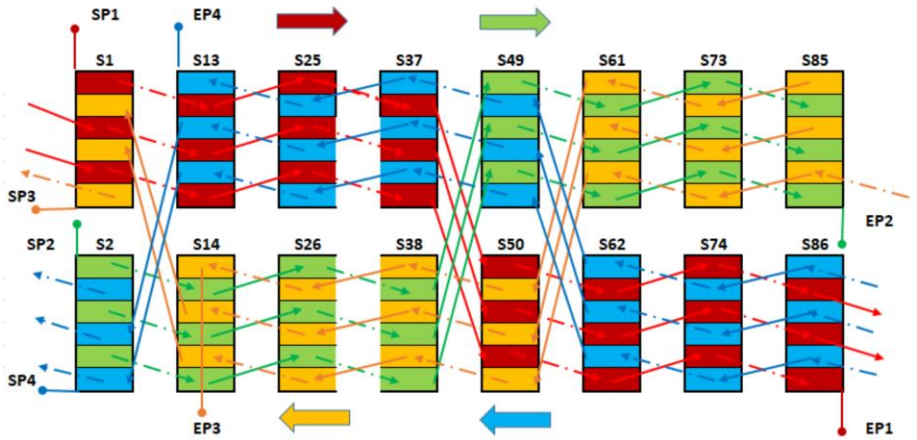

Fig. 79. Winding diagram of one phase, including all the paths. The even index slots are on the top, while the others on the bottom. Slots belonging to the same pole are on the same column.

To summarize, all the paths start from slots 1 and 2. The clockwise paths start from the 1st layer, while the counter-clockwise paths from the 6th. Depending on how the starting (SP_i) and ending (EP_i) terminals are connected, different phase layouts can be achieved. It has to be considered that the connection topology of each path and the terminal connection must be identical for every phase. This results in the winding diagram of the other phases being equal to that of fig. 79, with the exception of a different slot index, which can be obtained shifting the actual slot index with the correct phase shift.

4.2.3 Simulation Results

As stated in section 4.2, the main aim is to investigate the different series connections which can be obtained from the connection of the paths' terminals. To achieve that, path 1 is kept fixed as the starting one, while the connection order of all the other paths is varied. The simulated transition considers a SVPWM inverter going from a zero state to an active state, thus the HF total impedance will consist in the series connection of one phase with the parallel of the remaining two, as it has been done for the previous analysis of section 4.1. A remarkable difference is that here all the phases are modelled. The single phase will be the most stressed, since it will experience a total voltage drop of $\approx 2/3 V_{dc}$ (if no considerable overshoot occurs), where V_{dc} is the DC bus voltage. This analysis will consider the aforementioned transition when the phase shown in fig. 79 (A1) is the series connected one (from 000 to 100). The simulations are run with a square wave voltage input of 500V and a rise time of ≈33ns, corresponding to a frequency of ≈10MHz used for the estimation of the HF impedances in the FE-based software. The most representative slots to analyze are those where the start and end terminals of the four paths are located. These slots are the 1st, 2nd, 13th, 14th, 85th and 86th. Once a simulation is run, it is possible to extrapolate the voltage waveforms between adjacent layers belonging to each slots. Fig. 78 provides an example of the voltage between two layers.

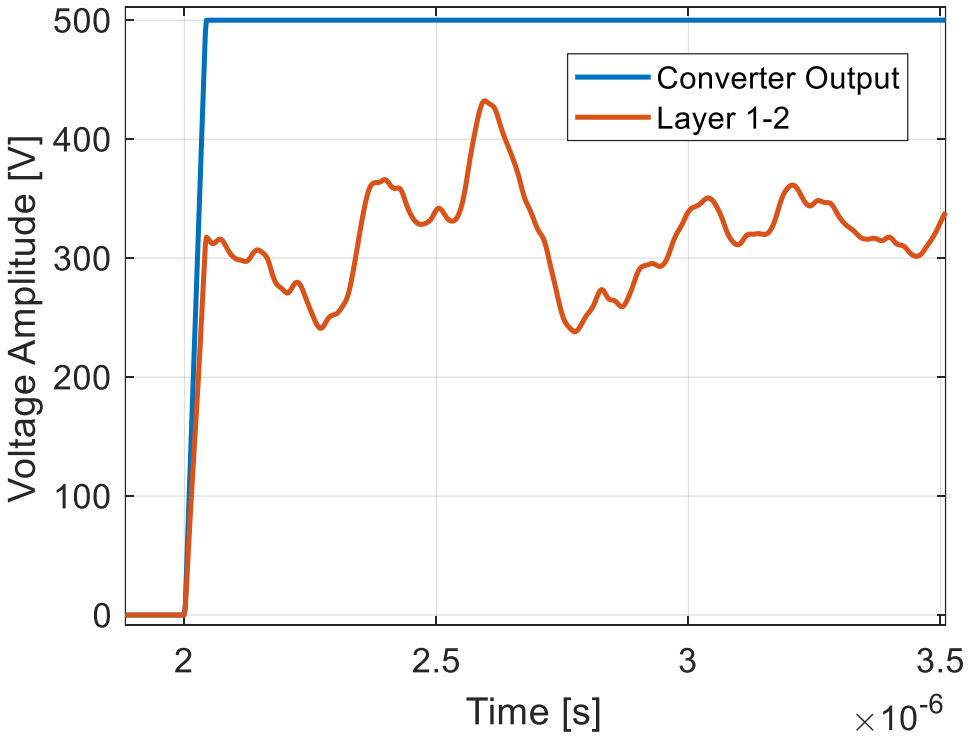

Fig. 80. Example of voltage waveform between the first two layers of a slot.

The most relevant value during each transition is the peak voltage which corresponds to the maximum voltage stress between the adjacent layers. Therefore, this value is selected for plotting fig. 81-86. This will provide an indication of the best connection paths' configurations C1xxx, where the indexes "1xxx" represent the path series connection order. Each figure from fig. 81 to fig. 86 illustrates the layer-to-layer peak voltage, during a switching transient, for each adjacent layers in a representative slot (S_i), and for all the analyzed C_{1xxx} configurations.

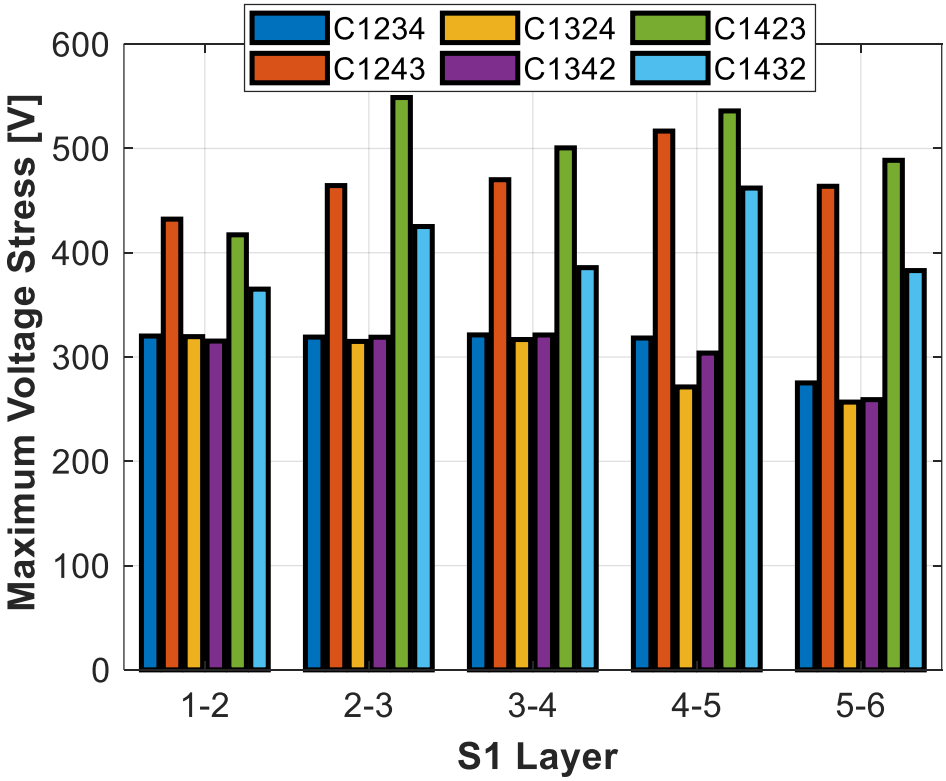

Fig. 81. Slot 1 maximum voltage stress as a function of layer.

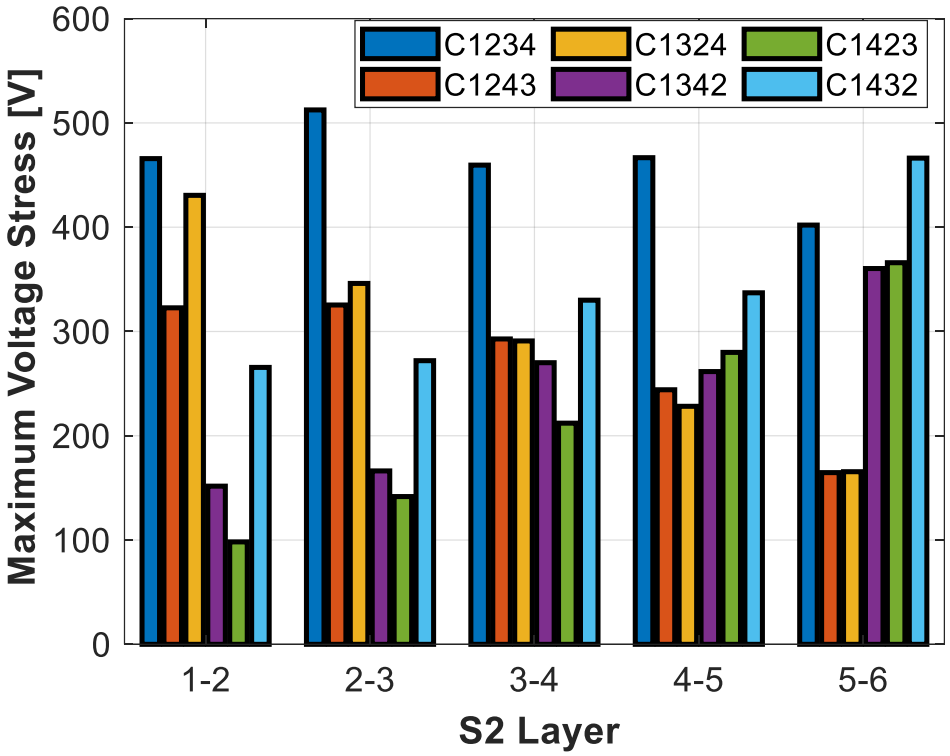

Fig. 82. Slot 2 maximum voltage stress as a function of layer.

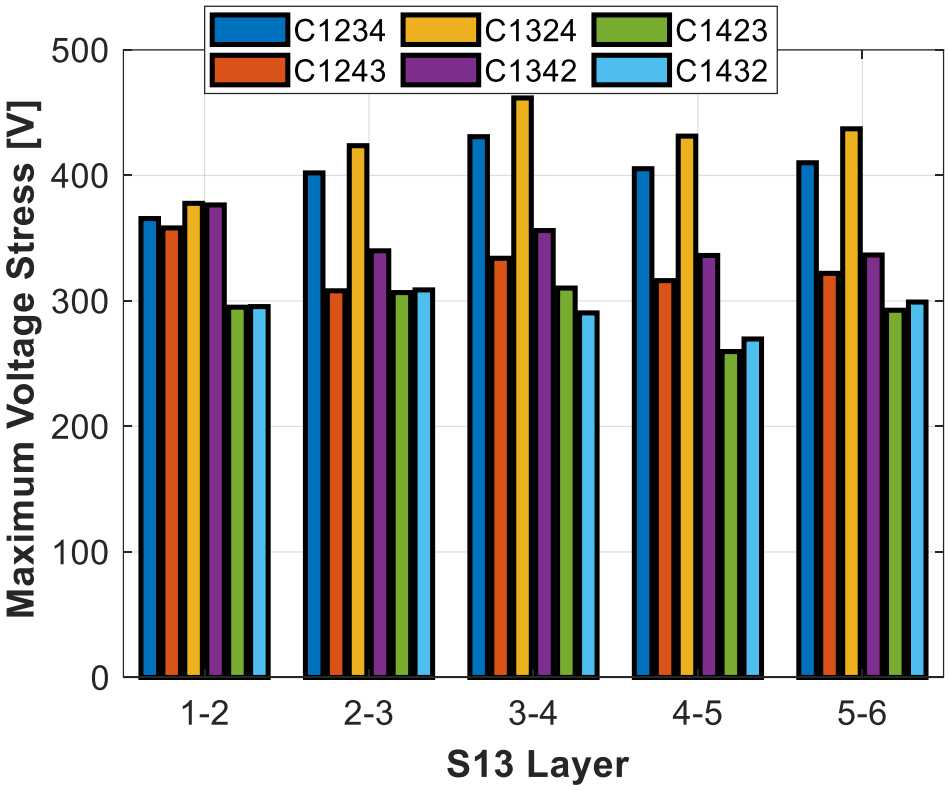

Fig. 83. Slot 13 maximum voltage stress as a function of layer.

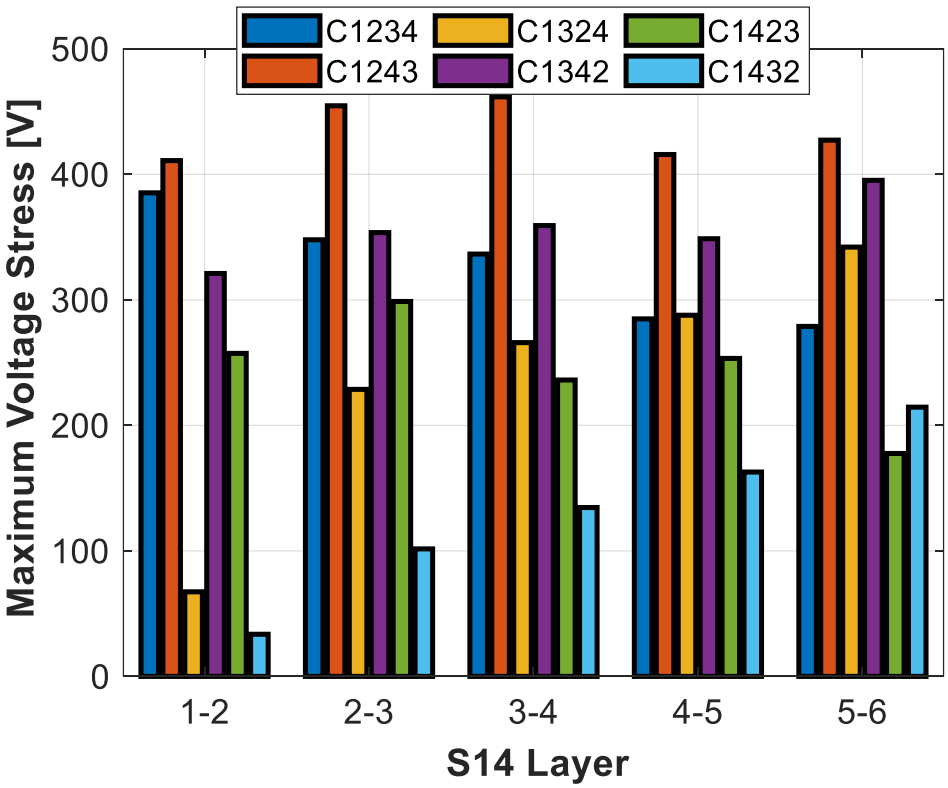

Fig. 84. Slot 14 maximum voltage stress as a function of layer.

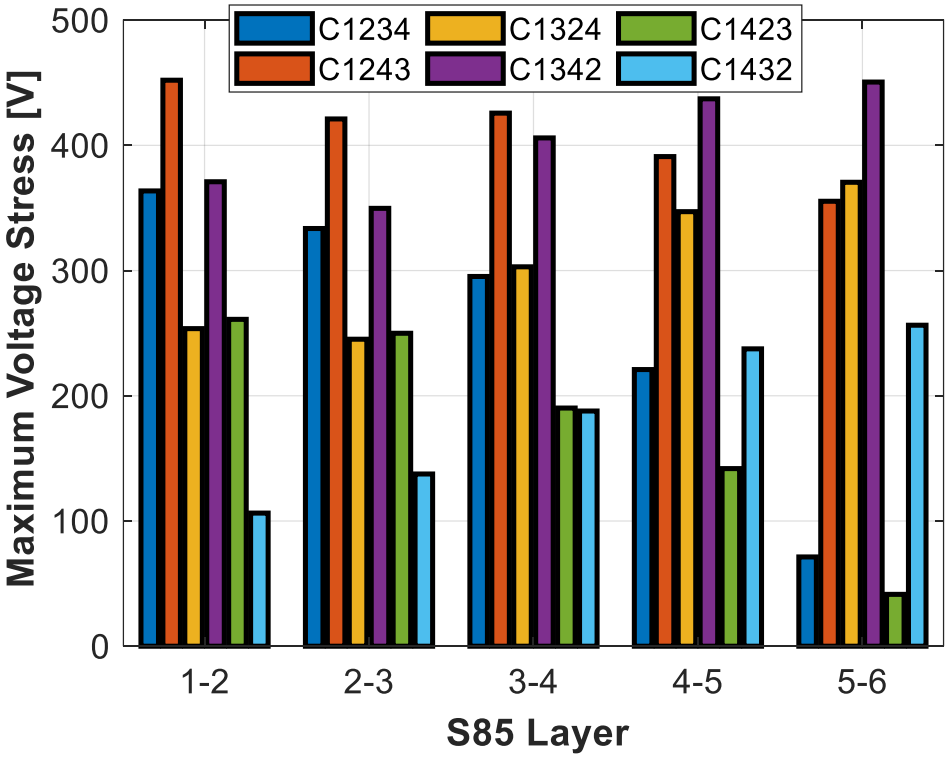

Fig. 85. Slot 85 maximum voltage stress as a function of layer.

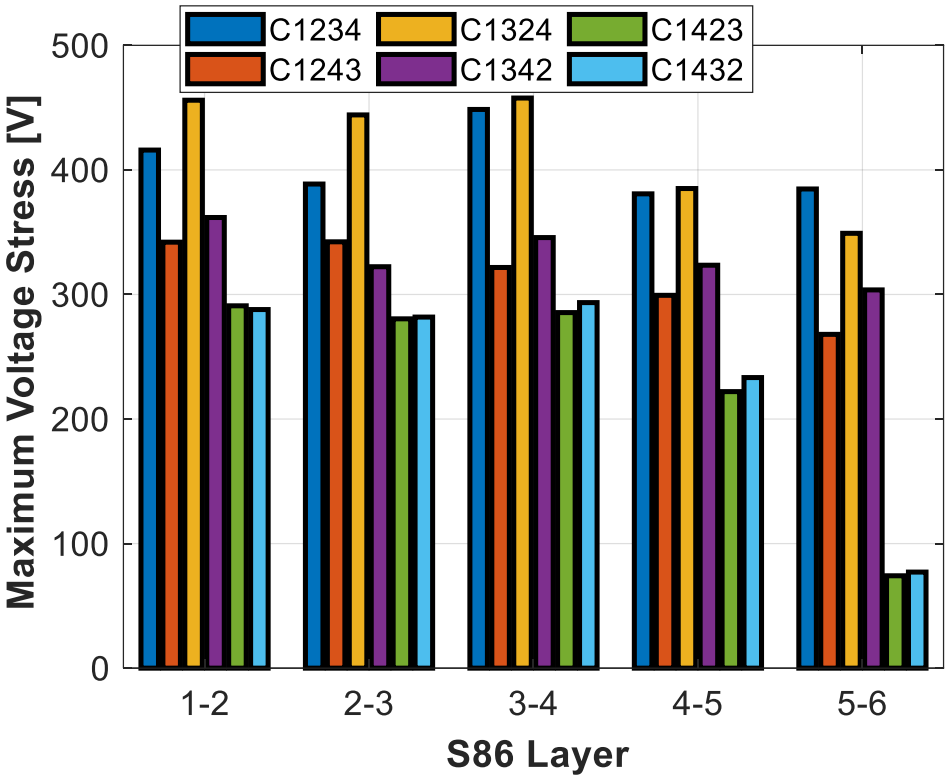

Fig. 86. Slot 86 maximum voltage stress as a function of layer.

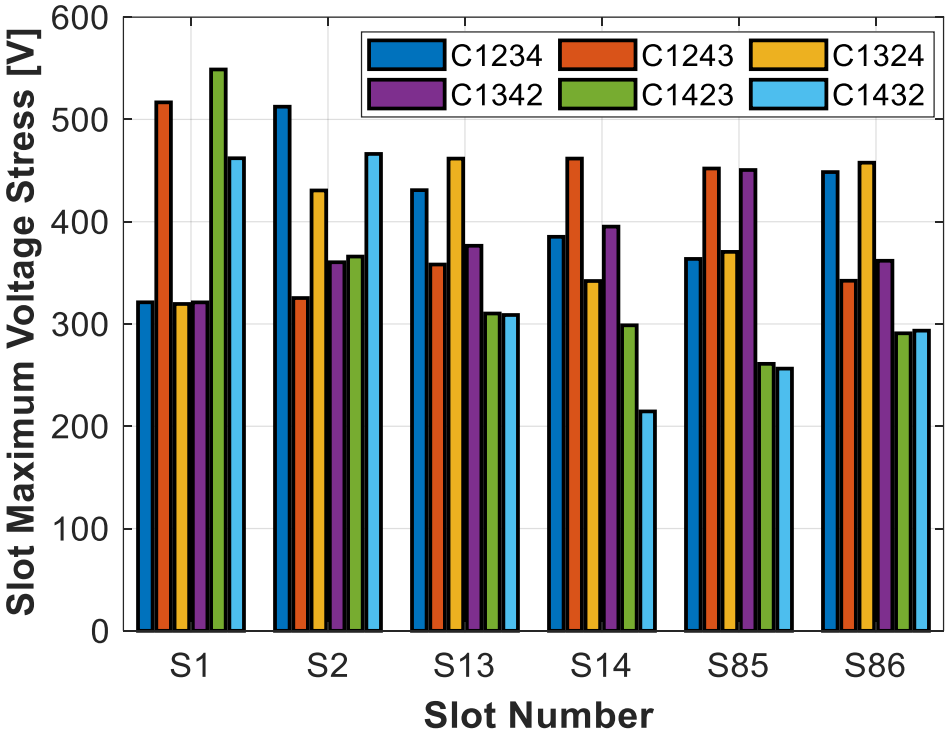

Fig. 87. Maximum value of slot peak voltage stress for all the configurations.

Fig. 87 shows a summary of the highest values of the maximum voltage stress occurring in each slot for each configuration, regardless of the layer where it occurs. This figure can provide a compact indication of the best configurations. From fig. 87 it can be observed

that there are two optimal configurations, i.e. C1342 (purple) and C1432 (light blue). They both always achieve a slot maximum voltage stress around 450V in two of the considered slots, i.e. S85 for C1342 and S1 for C1432. When the objective was to reduce only the highest value of the peak voltage stress, the path 1-3-4-2 would be the best one, as it can achieve a slightly lower value than the path 1-4-3-2. However, this second configuration can also provide a considerably lower average value of the peak voltage stress (in addition to a comparable maximum value), which is obtained in only two slots. In fact, C1432 has voltage stress values always below 300V for S14, S85 and S86, and a maximum value around 300 V for S13, which make it the most interesting choice. On the other hand, C1342 features values always above 300V, for every layer of all of the slots. A common characteristic of both configurations is that they have path 2 at the end of the series connection. It has to be noticed that the ending path has the same starting layer and wiring direction of the starting path, with which there are no slots in common. The other two paths, wounded in the opposite direction (counterclockwise), occupy the middle positions of the series connection. Therefore, some simple general rules can be derived as follow.

- Starting and ending paths should not share the same slots. In fact, paths which are far in the series connection exhibit a higher voltage difference, but the electrical stress between them cannot occur when there are no common slots.
- When the aim is also to contain the average peak voltage stress, the second path (in the connection order) should be the one which shares the highest number of slots with the starting path. Paths with many slots in common should always be kept as near as possible in the series connection, in order to reduce the voltage difference between them.
- When the winding is an ISDW with the same connection rules illustrated in section II.D, the series connections which satisfy the previous two points belong to one of these two categories: CW-CCW-CCW-CW or CCW-CW-CW-CCW, where CW stands for clockwise and CCW stands for counterclockwise. In order to minimize also the average peak voltage stress, the consecutive paths should start in different slots (this second rule is not satisfied by C1342).

Failing to meet these simple rules could result in voltage stresses, potentially exceeding the DC bus voltage amplitude. Another consideration can be added, regarding the adoption of a different winding rather than a traditional three-phase one. The maximum voltage stress between different layers is mainly determined by the inverter output

waveform, the machine high frequency parameters and the relative position of the different winding paths and sub paths of a specific phase, therefore it is expected to be quite independent form the total number of phases. The main advantage of having the possibility to adopt more than three-phases is instead the higher degree of freedom at the design stage and the possibility to adopt a lower number of different hairpins, thanks to the reduction of q. In fact, a higher number of q requires a shorter or longer connection each time the slot per pole per phase is changed in the winding connection procedure.

4.2.4 CONCLUSIONS

In section 4.2 the uneven voltage distribution and the ensuing voltage stress, triggered by a low rise time waveform feeding HWs, was investigated. The winding diagram of the adopted ISDW model was first described, and several ways to series connect the various paths of one machine phase were then illustrated. The voltage stresses between the winding layers were analyzed through the equivalent HF circuit model for all the possible configurations. Some basic rules to reduce both the maximum and the average of the peak voltage stresses between the layers were underlined. The main conclusion relates to a simple guideline consisting of keeping distant the paths with no slots in common, while paths with several slots in common should be kept as near as possible in the series connection.

4.3 VOLTAGE STRESS ANALYSIS FOR HWS FEATURING A CUSTOM SHORT PITCHED WINDING

As highlighted in section 4.2.1, no studies are available about the voltage stress within short pitched HWs. Hence, the aim of the section is to provide a first analysis on this topic, starting from a specific case study.

4.3.1 CASE STUDY

The machine under analysis is again a double three phase machine having 96 slots and 6 conductors per slot, however there are some differences with respect to the previously analyzed model:

- The machine is short pitched (SP) and features different conductor dimensions, which are illustrated in table XI. An asymmetric configuration has been adopted,

but there is only one thicker conductor in the slot bottom and then 5 remaining thinner conductors.

- A customized winding scheme has been adopted. It respects all the rules illustrated in [20], [21] and provides a balanced winding, however the connection paths are realized in a different way, as it can be seen in fig. 88, where a portion of the scheme is illustrated. Two parallel paths per phase are adopted. An important aspect to notice is that there are 2/3 of the slots which are shared between two different phases. These two phases are each time belonging to the two different three phase sets.

Table XI. WINDING PARAMETERS FOR SHORT-PITCHED HW

Winding topology	SP
Slots	96
Slot Conductors	6
Conductor dimensions [mm]	2.8 x 4 (1) 2.8 x 2 (5)
Phase Paths	2

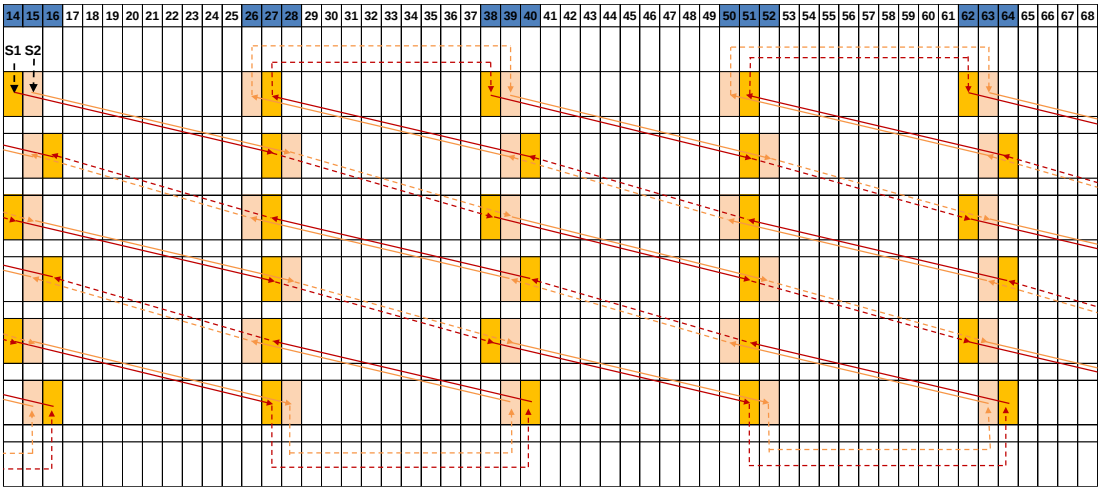

Fig. 88. Portion of 96-slot SP HW diagram. Phase A1 is displayed.

4.3.1.1 FE Model

The realization of the FE model can be done as previously illustrated and with the same hypothesis of section 4.2.2.1. 2D transient magnetic simulations can be done to estimate the inductances and resistances, while electrostatic simulations can be done to estimate the capacitances. A picture of it is shown in fig. 89.

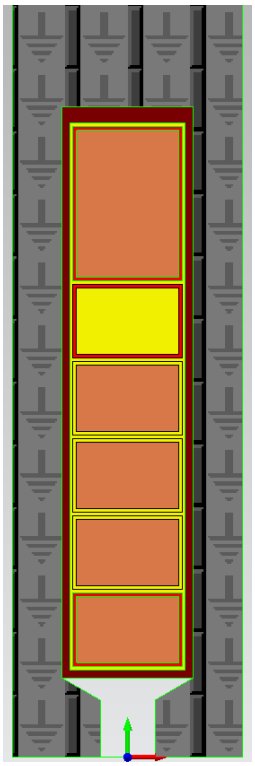

Fig. 89. FE 2D slot model for SP HW machine.

4.3.1.2 UPDATED CIRCUIT MODEL

The adopted HF circuit model is illustrated in fig. 90. The new model is rather similar to that of fig. 78, however an additional parallel resistance (R_p) has been added to take into account the iron losses effect on the machine impedance. It is well known that the estimating the iron losses through FE simulations is not an easy task and can be subjected to relatively high errors due to the different behaviour of the ferromagnetic materials with respect to the data sheet and due to the harmonic content triggered by non perfectly sinusoidal supplies. However, trying to take into account them with feasible values from FE simulations can still be helpful. On the other hand, if machine impedance data are available, R_p can be estimated with a higher accuracy, especially when approaching the MHz, where the damping effect is important. For the following study, R_p has been estimated with the help of an impedance measurement. The procedure is straightforward and as follows:

1) The main HF parameters are firstly estimated with a FE simulation. R_p is only hypothesized.
2) The impedance of the HF model is compared with the measured one.
3) R_p tends to limit the amplitude of first resonance point as highlighted in fig. 90. If the damping effect is not accurate, the value can be changed until there is a sufficiently good match.

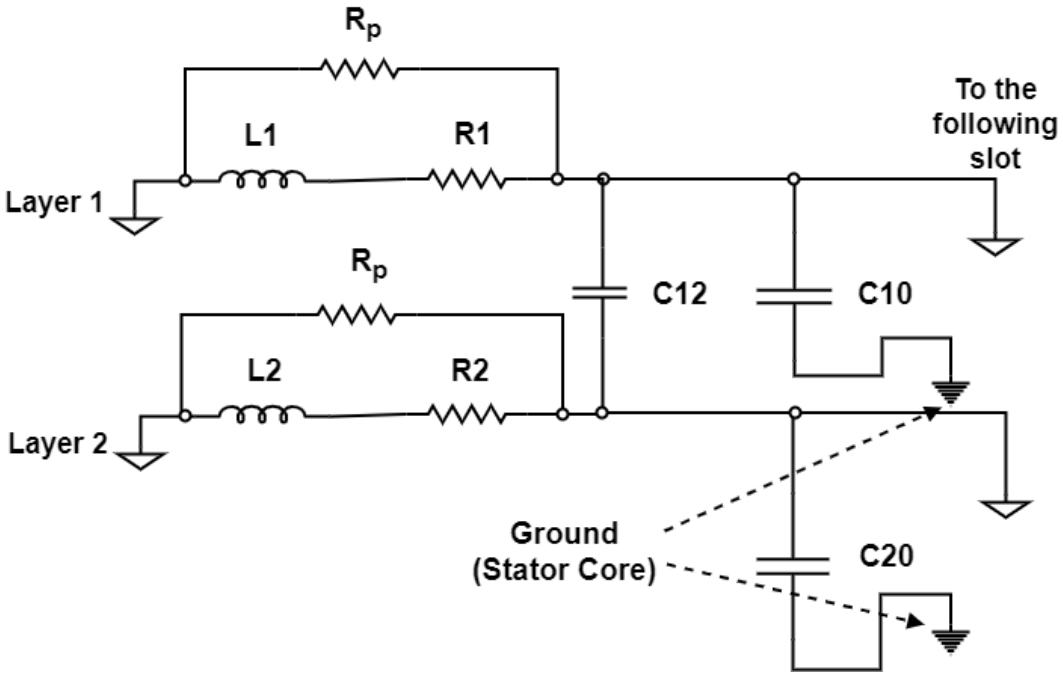

Fig. 90. Updated HF slot model.

It has to be considered that this procedure can be extended also for the other equivalent circuit parameters in order to tune the HF model. In particular it can be useful also for the inductance value, whose value is highly dependent on the effective relative permeability of the ferromagnetic material.

4.3.2 SIMULATIONS

The simulation have been run accordingly to section 4.2.3. The main difference is that, for this analysis, two feeding converters are needed, one for each three phase set, and their output waveform are also delayed in time, as in fig. 92. The main simulations parameters are the following: the rise time is equal to 100 ns and the DC bus voltage is 700 V.

The simulated transition will again take into consideration the passage from a zero state, to an active state of SVPWM for the considered phase, which is A1. The same transition is considered for the second set (from 000 to 001, C2 is the series connected phase), which put the system in the worst case scenario in terms of maximum voltage stress between different layers for the considered machine.

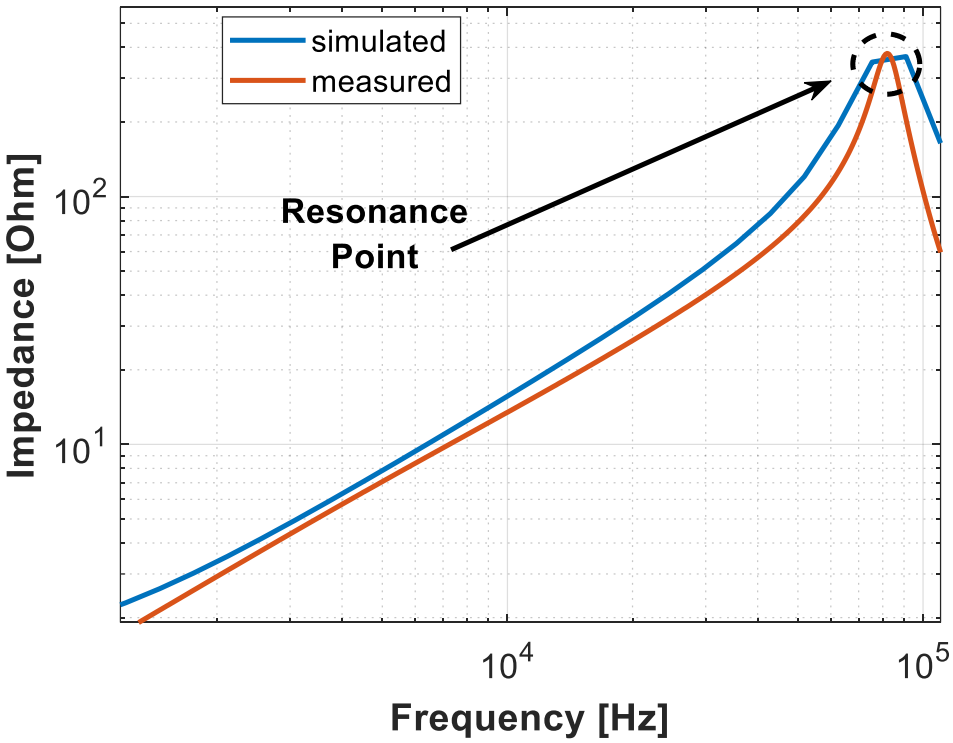

Fig. 91. Machine Impedance when 2 phases are put in series.

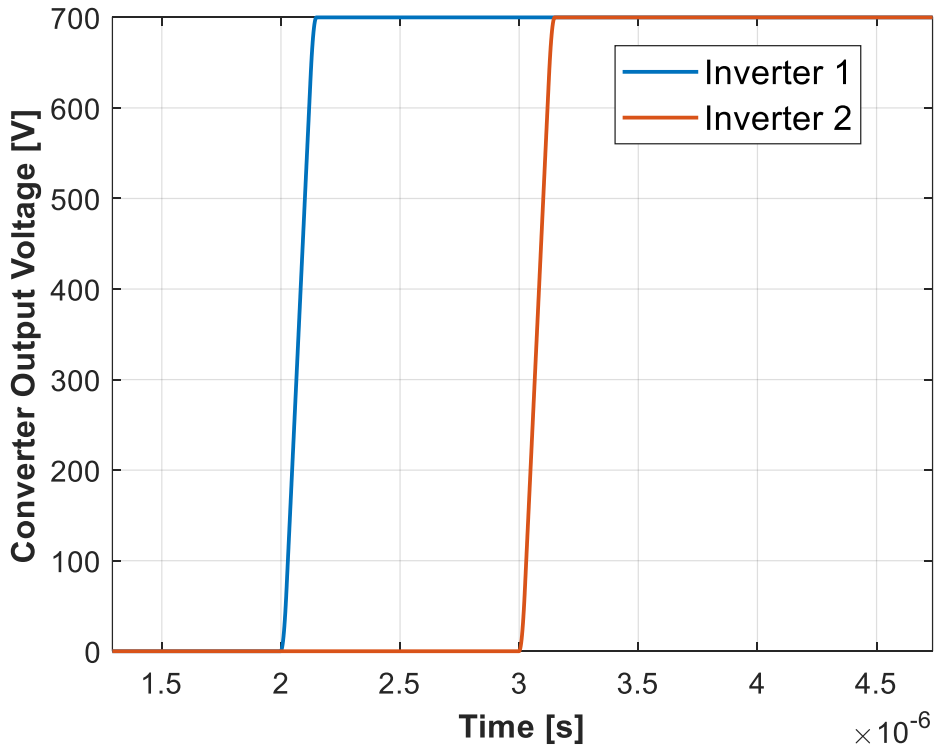

Fig. 92. Output waveforms from the converters feeding the DT winding.

The main results are illustrated in fig. 93, where the maximum voltage stress for each slot of phase A1 is shown.

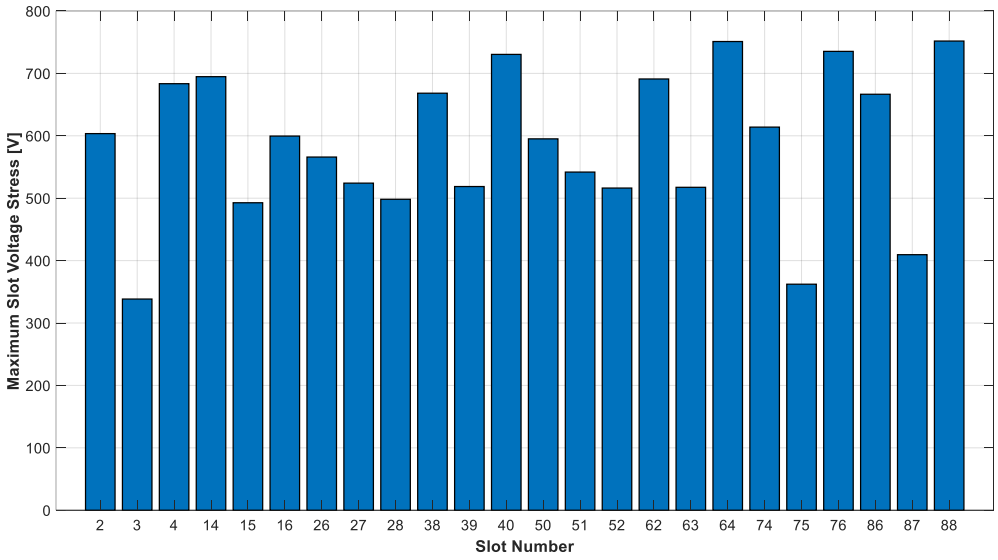

Fig. 93. Maximum slot voltage stress for the SP HW machine when both the three phase sets experiments a transition from a zero state, to an active state of SVPWM. All the slots of phase A1 are considered.

As it can be noticed, the voltage stress is really high in some slots and it is comparable to the DC bus voltage value. More precisely, all the slots with the higher maximum voltage stress values are slots where two phases are present. In fact, phase A1 and B2 share all the slots with index 2+k*12 (k = 0, 1, …, 7), while phase A1 and A2 share all the slots with index 4+k*12 (k = 0, 1, …, 7). Slots with only phase A1 have instead on average much lower values. For this reason, if adopting a SP winding can provide some advantages in terms of reduced spatial harmonic content and reduced end winding length, it is also clear that a higher attention should be paid in the selection of proper insulating material, since the maximum voltage stress will be considerably higher compared to a full pitch counterpart.

4.3.3 CONCLUSIONS

Sections 4.3 focused on the extension of the findings of section 4.2. A voltage stress analysis within SP HWs fed by short rise time converters was performed. The adopted procedure is quite similar to the one adopted in section 4.2. The main difference was represented by the adoption of an improved HF model, which could also consider the effect of the iron losses. The results have shown that the slots where two different phases are present, feature much higher peak voltages compared to the remaining ones. Hence, if the main aim was to increase the winding insulation reliability, adopting a FP winding would be a preferable solution. On the other hand, if the adoption of a SP winding was

necessary for other reasons, a higher quality or thicker insulation materials should be chosen. Other possible options are represented by the adoption of multi-level inverters or passive filters at the cost of slightly higher losses [93]. However, these solutions are not investigated in this thesis as this goes beyond the scope of this work.

4.4 Final Considerations on Chapter 4

This chapter focused on some challenging aspects related to the reliability of electrical machines and drives. Much effort was spent on the modelling and analyses of the voltage stress sources both for random and hairpin conductor windings. It was shown that the possibility to trigger dangerous overvoltage is strictly related to the applied voltage rise time which affects the HF waveform harmonic content. For this reason, accurate HF models need to be adopted. A crucial aspect is that designing an electrical drive with the only aim to increase the overall "main" electromagnetic performance parameters can lead to undesired circumstances and to a higher chance of premature failure. Long cables, short rise times or non-optimal winding schemes can seriously increase the voltage stress. Hence, reliability should be considered as a primary objective from the beginning of the machine design process.

5. CONCLUSIONS

This chapter provides a general conclusion, as well as further observations relative to the main achievements and novelties of this project are discussed.

5.1 GENERAL CONCLUSIONS

This work addressed several methodologies relative to increasing the power density and reliability of rotating electrical machines for traction applications.

Chapter 1 has provided an introduction on the entire work, illustrating the whole structure and the main objectives. For all the remaining chapters, a similar approach has been adopted. The first part dealt with an overview on the involved topics through a literature review and analysis on the possible developments. Then more detailed analyses by means of analytical approaches and simulations were presented. In particular, Chapter 2 focused mainly on the theoretical analysis of HWs. The analytical methods for AC losses estimation already presented in literature were implemented and used to investigate the adoption of different materials than copper, such as aluminium. The accuracy of such methodology was also discussed, as well as the main sources of errors. Then a specific analytical approach was developed for the evaluation of AC losses in the so called segmented HW, where classical analytical approaches can lead to a significant prediction error. The specific formulation was validated both through FE simulations and experimental measurements, the latter performed on portions of machine stator (i.e. motorettes). In addition, some important guidelines were provided for the practical realization of balanced segmented HWs, illustrating the main advantages and bottlenecks of such technology.

The focus of Chapter 3 was on the analysis of multi-three-phase HW machines as a means to increase torque and power density. The study started from some specific requirements in terms of torque-speed characteristics. After having evaluated the feasibility of such configuration, the main characteristics of the resulting machine were estimated, showing great potentials in terms of torque and power density improvements. Then, the adopted winding was also optimized in order to limit the total machine Joule losses. In the final part of Chapter 3, an analysis of the AC losses in the end windings was carried out, as well as the mapping of the machine characteristics through the FP method was reported for the sake of completeness.

Chapter 4 concludes the work with a major focus on the reliability, through the analysis of the electrical stress within machine windings. The main sources and conditions of high voltage stress are evaluated for both random and HW configurations, when the electrical drives are equipped with short-rise time WBG devices. A comprehensive cable-converter-motor was proposed and experimental results on random windings were performed for validation purposes. Possible solutions to mitigate the peak voltages were finally proposed.

5.2 CONTRIBUTIONS TO RESEARCH

The major contributions of this work from a technical and academic point of view are the following:

1) The investigation on the possibility to adopt aluminium or its alloys for HWs, as opposed to copper. In the range of 0 – 1 kHz, a properly optimized copper winding can provide better performances compared to higher resistivity materials. However, at higher frequencies, the above observation is questionable.
2) The evaluation of the accuracy of the "classical" analytical formulation for AC loss prediction. For a first stage analysis, the analytical formulation can provide good results, with the main source of error being provided by the rotor influence. In fact, the rotor can cause a high saturation in IPM or PM-assisted synchronous reluctance machines, while on the other hand the PMs can provide additional magnetic field harmonics. Saturation plays an important role in flattening (thus reducing) the total winding Joule losses due to the limitation of the flux density value and, consequently, of the proximity losses. The additional magnetic field harmonics provided by the PMs can instead increase the Joule losses. These effects tend to have a counter-balancing action, thus the analytical formulation error results to be acceptable. The outcomes of the research regarding the first two points have been published in two conference papers [104], [107].
3) The development and validation of a specific analytical formulation for segmented HWs. The "classical" formulation illustrated in [32] cannot be adopted for the estimation of AC losses in segmented HWs. The proposed approach is a compact one too and shows also a clear link between the winding parameters and the AC/DC loss ratio for each winding layer, as the "classical" approach does for a standard configuration.

4) The guidelines for the practical realization of HWs featuring some segmented conductors: both the choice of geometrical parameters and the realization of proper winding connections are illustrated. The proposed guidelines show the importance of properly selecting the sub-conductor dimensions when such configuration is adopted. In addition, it is suggested not to use more than two sub conductors for each equivalent conductor. From a connection point, the proposed methodology allows the realization of balanced windings with a limited number of additional welding spots.

5) The possibility to increase both torque and power density with the adoption of multi-three-phase HWs. The starting requirements have been easily met with such configuration and the winding realization with all the transpositions can proceed as for three-phase windings. The lower number of slots per pole per phase and needed phase parallel paths can also result in simpler winding transpositions. In addition, with a properly optimized winding, the AC losses can be contained in the range 0 – 1 kHz, allowing the machine to operate in steady state conditions at full load for the majority of the frequency range. The outcomes of this research have been published in a conference paper [102].

6) The analysis of the end winding losses for HWs. AC losses cannot be neglected in the end winding of hairpin conductors, however their impact is much lower with respect to the active part. If the conductor dimensions have already been optimized to reduce the active length K_{rk}, the losses in the end winding can be estimated as purely DC for a wide frequency range with a small error (< 10%). For the considered case study, this assumption has started to be less acceptable approaching 1 kHz. An important finding is that, also in the end winding, the layer number has some impact for the value of K_{rk}, showing the importance of border effects. Saturation of the active part has also some impact. Higher saturations tend to limit the losses also in the end winding, however the impact is quite limited in absolute values. The outcomes of this research have been published in a conference paper [106].

7) The modelling and analysis of the voltage stress sources within machine windings. A specific methodology has been illustrated and validated. However, it has been shown that a high attention needs to be paid for the evaluation of all the parameters. The rise time has proved to be the most influencing parameter. Short rise times can trigger high voltage overshoot and highly uneven voltage

distributions within the windings. For electric drives fed by WBG devices, the adoption of short cables is mandatory and the use of passive filters or multi-level converter should be considered in some cases. The outcomes of this research have been published in two conference papers [101][103] and two journal papers [99][100].

8) The guidelines for the reduction of the voltage stress with HWs through proper path connections. The voltage stress can be seriously mitigated in HWs only by paying attentions to the possible winding diagram connections. Among the possible options, series connections in which paths with no common slots are kept distant, and paths with the higher number of common slots are kept close to each other should be preferred. Short pitch windings should instead be avoided when possible. If they can provide benefits in terms of spatial harmonic reduction, their adoption determines much higher inter-layer peak voltages, resulting in the need of thicker or more expensive insulation materials. The outcomes of this research have been published in a conference paper [105].

6. REFERENCES

[1] IEA (2021), *Net Zero by 2050*, IEA, Paris https://www.iea.org/reports/net-zero-by-2050

[2] J. Benzaquen, J. He and B. Mirafzal, "Toward more electric powertrains in aircraft: Technical challenges and advancements," in CES Transactions on Electrical Machines and Systems, vol. 5, no. 3, pp. 177-193, Sept. 2021, doi: 10.30941/CESTEMS.2021.00022.

[3] E. Sayed et al., "Review of Electric Machines in More-/Hybrid-/Turbo-Electric Aircraft," in IEEE Transactions on Transportation Electrification, vol. 7, no. 4, pp. 2976-3005, Dec. 2021, doi: 10.1109/TTE.2021.3089605.

[4] I. Husain et al., "Electric Drive Technology Trends, Challenges, and Opportunities for Future Electric Vehicles," in Proceedings of the IEEE, vol. 109, no. 6, pp. 1039-1059, June 2021, doi: 10.1109/JPROC.2020.3046112.

[5] K. Bhadane et al., "A Comprising Study on Modernization of Electric Vehicle Subsystems, Challenges, Opportunities and strategies for its Further Development," 2021 4th Biennial International Conference on Nascent Technologies in Engineering (ICNTE), 2021, pp. 1-9, doi: 10.1109/ICNTE51185.2021.9487757.

[6] M. Popescu, J. Goss, D. A. Staton, D. Hawkins, Y. C. Chong and A. Boglietti, "Electrical Vehicles—Practical Solutions for Power Traction Motor Systems," in IEEE Transactions on Industry Applications, vol. 54, no. 3, pp. 2751-2762, May-June 2018, doi: 10.1109/TIA.2018.2792459.

[7] R. T. M. Smokers, M. Verbeek and S. van Zyl, "EVs and post 2020 CO2 targets for passenger cars," 2013 World Electric Vehicle Symposium and Exhibition (EVS27), Barcelona, 2013, pp. 1-11, doi: 10.1109/EVS.2013.6915006.

[8] Y. Zhao, D. Li, T. Pei and R. Qu, "Overview of the rectangular wire windings AC electrical machine," in CES Transactions on Electrical Machines and Systems, vol. 3, no. 2, pp. 160-169, June 2019, doi: 10.30941/CESTEMS.2019.00022.

[9] S. Nuzzo, D. Barater, C. Gerada and P. Vai, "Hairpin Windings: An Opportunity for Next-Generation E-Motors in Transportation," in IEEE Industrial Electronics Magazine, doi: 10.1109/MIE.2021.3106571.

[10] A. Reinap, M. Andersson, F. J. Márquez-Fernández, P. Abrahamsson and M. Alaküla, "Performance Estimation of a Traction Machine with Direct Cooled Hairpin Winding," 2019 IEEE Transportation Electrification Conference and Expo (ITEC), Detroit, MI, USA, 2019, pp. 1-6, doi: 10.1109/ITEC.2019.8790545.

[11] F. Momen, K. Rahman and Y. Son, "Electrical Propulsion System Design of Chevrolet Bolt Battery Electric Vehicle," in IEEE Transactions on Industry Applications, vol. 55, no. 1, pp. 376-384, Jan.-Feb. 2019, doi: 10.1109/TIA.2018.2868280.

[12] F. Zhang et al., "A Thermal Modeling Approach and Experimental Validation for an Oil Spray-Cooled Hairpin Winding Machine," in IEEE Transactions on Transportation Electrification, vol. 7, no. 4, pp. 2914-2926, Dec. 2021, doi: 10.1109/TTE.2021.3067601.

[13] C. Du-Bar, A. Mann, O. Wallmark and M. Werke, "Comparison of Performance and Manufacturing Aspects of an Insert Winding and a Hairpin Winding for an Automotive Machine Application," 2018 8th International Electric Drives Production Conference (EDPC), Schweinfurt, Germany, 2018, pp. 1-8.

[14] A. Arzillo et al., "Challenges and Future opportunities of Hairpin Technologies," 2020 IEEE 29th International Symposium on Industrial Electronics (ISIE), 2020, pp. 277-282, doi: 10.1109/ISIE45063.2020.9152417.

[15] F. Wirth, T. Kirgör, J. Hofmann and J. Fleischer, "FE-Based Simulation of Hairpin Shaping Processes for Traction Drives," 2018 8th International Electric Drives Production Conference (EDPC), 2018, pp. 1-5, doi: 10.1109/EDPC.2018.8658278.

[16] A. Riedel et al., "Challenges of the Hairpin Technology for Production Techniques," 2018 21st International Conference on Electrical Machines and Systems (ICEMS), 2018, pp. 2471-2476, doi: 10.23919/ICEMS.2018.8549105.

[17] T. Glaessel et al., "Process Reliable Laser Welding of Hairpin Windings for Automotive Traction Drives," 2019 International Conference on Engineering, Science, and Industrial Applications (ICESI), 2019, pp. 1-6, doi: 10.1109/ICESI.2019.8863004.

[18] T. Glaessel, J. Seefried and J. Franke, "Challenges in the manufacturing of hairpin windings and application opportunities of infrared lasers for the contacting process," 2017 7th International Electric Drives Production Conference (EDPC), 2017, pp. 1-7, doi: 10.1109/EDPC.2017.8328150.

[19] A. Mayr et al., "Evaluation of Machine Learning for Quality Monitoring of Laser Welding Using the Example of the Contacting of Hairpin Windings," 2018 8th International Electric Drives Production Conference (EDPC), 2018, pp. 1-7, doi: 10.1109/EDPC.2018.8658346.

[20] T. Zou et al., "A Comprehensive Design Guideline of Hairpin Windings for High Power Density Electric Vehicle Traction Motors," in IEEE Transactions on Transportation Electrification, doi: 10.1109/TTE.2022.3149786.

[21] G. Berardi, N. Bianchi, "Design guideline of an AC hairpin winding", 2018 XIII International Conference on Electrical Machines (ICEM), pp. 2444-2450, 3.-6. Sept. 2018.

[22] N. Bianchi and G. Berardi, "Analytical Approach to Design Hairpin Windings in High Performance Electric Vehicle Motors," 2018 IEEE Energy Conversion Congress and Exposition (ECCE), 2018, pp. 4398-4405, doi: 10.1109/ECCE.2018.8558383.

[23] S. Zhu, K. Paciura and R. Barden, "Design Approach of Hairpin Winding Motor with High Parallel Path Numbers," 2021 IEEE Energy Conversion Congress and Exposition (ECCE), 2021, pp. 4534-4538, doi: 10.1109/ECCE47101.2021.9595449.

[24] M. England, B. Dotz and B. Ponick, "Evaluation of Winding Symmetry and Circulating Currents of Hairpin Windings," 2021 IEEE International Electric Machines & Drives Conference (IEMDC), 2021, pp. 1-8, doi: 10.1109/IEMDC47953.2021.9449604.

[25] E. Preci et al., "Segmented Hairpin Topology for Reduced Losses at High Frequency Operations," in IEEE Transactions on Transportation Electrification, doi: 10.1109/TTE.2021.3103821.

[26] A. Arzillo et al., "An Analytical Approach for the Design of Innovative Hairpin Winding Layouts," 2020 International Conference on Electrical Machines (ICEM), Gothenburg, 2020, pp. 1534-1539, doi: 10.1109/ICEM49940.2020.9270927.

[27] M. S. Islam, I. Husain, A. Ahmed and A. Sathyan, "Asymmetric Bar Winding for High-Speed Traction Electric Machines," in IEEE Transactions on Transportation Electrification, vol. 6, no. 1, pp. 3-15, March 2020.

[28] X. Fan, D. Li, R. Qu, C. Wang and J. Li, "Hybrid Rectangular Bar Wave Windings to Minimize Winding Losses of Permanent Magnet Machines for EV/HEVs over a Driving Cycle.," 2018 IEEE International Magnetics Conference (INTERMAG), Singapore, 2018, pp. 1-2, doi: 10.1109/INTMAG.2018.8508038.

[29] C. Du-Bar and O. Wallmark, "Eddy Current Losses in a Hairpin Winding for an Automotive Application," 2018 XIII International Conference on Electrical Machines (ICEM), Alexandroupoli, 2018, pp. 710-716, doi: 10.1109/ICELMACH.2018.8507265.

[30] P. S. Ghahfarokhi, A. Podgornovs, A. J. Marques Cardoso, A. Kallaste, A. Belahcen and T. Vaimann, "Hairpin Windings Manufacturing, Design, and AC Losses Analysis Approaches for Electric Vehicle Motors," 2021 11th International Electric Drives Production Conference (EDPC), 2021, pp. 1-7, doi: 10.1109/EDPC53547.2021.9684208.

[31] Optimisation of Hairpin Winding in Electric Traction Motor Applications

[32] J. Pyrhonen, J. Tapani, and V. Hrabovcova, “Influence of Skin Effect on Resistance” in Design of Rotating Electrical Machines. Chichester, U.K.: Wiley, 2008, pp. 256-261.

[33] Richter, R. Electrical Machines: General Calculation Elements. DC Machines (Elektrische Maschinen: Allgemeine Berechnungselemente. Die Gleichstrommaschinen), Vol. I, 3rd edn, Birkhauser Verlag, Basle and Stuttgart, 1967, pp. 239-241.

[34] A. Acquaviva, M. Diana, B. Raghuraman, L. Petersson and S. Nategh, "Sustainability Aspects of Electrical Machines For E-Mobility Applications Part II: Aluminium Hairpin vs. Copper Hairpin," IECON 2021 – 47th Annual Conference of the IEEE Industrial Electronics Society, 2021, pp. 1-6, doi:10.1109/IECON48115.2021.9589649.

[35] F. Scuiller, J. Charpentier and E. Semail, "Multi-star multi-phase winding for a high power naval propulsion machine with low ripple torques and high fault tolerant ability," 2010 IEEE Vehicle Power and Propulsion.

[36] F. Scuiller, E. Semail, J. -. Charpentier and P. Letellier, "Multi-criteria-based design approach of multi-phase permanent magnet low-speed synchronous machines," in *IET Electric Power Applications*, vol. 3, no. 2, pp. 102-110, March 2009.

[37] C. Bassi, A. Tessarolo, R. Menis and G. Sulligoi, "Analysis of different system design solutions for a high-power ship propulsion synchronous motor drive with multiple PWM converters," Electrical Systems for Aircraft, Railway and Ship Propulsion, Bologna, 2010, pp. 1-6.

[38] A. Tessarolo, G. Zocco and C. Tonello, "Design and testing of a 45-MW 100-Hz quadruple-star synchronous motor for a Liquefied Natural Gas turbo-compressor drive," SPEEDAM 2010, Pisa, 2010, pp. 1754-1761.

[39] F. Barrero and M. J. Duran, "Recent Advances in the Design, Modeling, and Control of Multiphase Machines—Part I," in IEEE Transactions on Industrial Electronics, vol. 63, no. 1, pp. 449-458, Jan. 2016.

[40] E. Levi, "Multiphase Electric Machines for Variable-Speed Applications," in *IEEE Transactions on Industrial Electronics*, vol. 55, no. 5, pp. 1893-1909, May 2008.

[41] X. Wang *et al.*, "Torque Ripple Reduction in Sectored Multi Three-Phase Machines Based on PWM Carrier Phase Shift," in *IEEE Transactions on Industrial Electronics*, vol. 67, no. 6, pp. 4315-4325, June 2020.

[42] Investigation of Phase Angle Displacements in Six-Phase PMSM with Concentrated Windings for Reduced MMF Harmonics," 2018 21st International Conference on Electrical Machines and Systems (ICEMS), Jeju, 2018, pp. 308-313.

[43] Y. Demir and M. Aydin, "A Novel Dual Three-Phase Permanent Magnet Synchronous Motor With Asymmetric Stator Winding," in IEEE Transactions on Magnetics, vol. 52, no. 7, pp. 1-5, July 2016, Art no.

[44] Q. Chen, D. Liang, S. Jia and X. Wan, "Analysis of Multi-Phase and Multi-Layer Factional-Slot Concentrated-Winding on PM Eddy Current Loss Considering Axial Segmentation and Load Operation," in *IEEE Transactions on Magnetics*, vol. 54, no. 11, pp. 1-6, Nov. 2018, Art no. 8107506, doi: 10.1109/TMAG.2018.2841874.

[45] H. Dhulipati, E. Ghosh, S. Mukundan, P. Korta, J. Tjong and N. C. Kar, "Advanced Design Optimization Technique for Torque Profile Improvement in Six-Phase PMSM Using Supervised Machine Learning for Direct-Drive EV," in IEEE Transactions on Energy Conversion, vol. 34, no. 4, pp. 2041-2051, Dec. 2019.

[46] X. Deng, B. Mecrow, H. Wu and R. Martin, "Design and Development of Low Torque Ripple Variable-Speed Drive System With Six-Phase Switched Reluctance Motors," in IEEE Transactions on Energy Conversion, vol. 33, no. 1, pp. 420-429, March 2018.

[47] M. Farshadnia, M. A. Masood Cheema, A. Pouramin, R. Dutta and J. E. Fletcher, "Design of Optimal Winding Configurations for Symmetrical Multiphase Concentrated-Wound Surface-Mount PMSMs to Achieve Maximum Torque Density Under Current Harmonic Injection," in *IEEE Transactions on Industrial Electronics*, vol. 65, no. 2, pp. 1751-1761, Feb. 2018.

[48] L. Parsa, "On advantages of multi-phase machines," *31st Annual Conference of IEEE Industrial Electronics Society, 2005. IECON 2005.*, Raleigh, NC, 2005, pp. 6 pp.-.

[49] M. Barcaro, N. Bianchi and F. Magnussen, "Six-Phase Supply Feasibility Using a PM Fractional-Slot Dual Winding Machine," in *IEEE Transactions on Industry Applications*, vol. 47, no. 5, pp. 2042-2050, Sept.-Oct. 2011.

[50] F. Scuiller, "Predicting the Space Harmonics Generated by Symmetrical Multi-Phase Windings," 2019 IEEE International Electric Machines & Drives Conference (IEMDC), San Diego, CA, USA, 2019, pp. 1348-1355.

[51] E. Fornasiero, N. Bianchi and S. Bolognani, "Rotor losses in fractional-slot three-phase and five-phase PM machines," *The XIX International Conference on Electrical Machines - ICEM 2010*, Rome, 2010, pp. 1-5.

[52] M. Diana, R. Ruffo and P. Guglielmi, "Low torque ripple tooth coil windings multi-3-phase machines: design considerations and validation," in IET Electric Power Applications, vol. 14, no. 2, pp. 262-273, 2 2020.

[53] Y. Burkhardt, A. Spagnolo, P. Lucas, M. Zavesky and P. Brockerhoff, "Design and analysis of a highly integrated 9-phase drivetrain for EV applications," *2014 International Conference on Electrical Machines (ICEM)*, Berlin, 2014, pp. 450-456.

[54] B. Hannon, P. Sergeant and L. Dupré, "Time- and Spatial-Harmonic Content in Synchronous Electrical Machines," in IEEE Transactions on Magnetics, vol. 53, no. 3, pp. 1-11, March 2017, Art no. 8101011.

[55] G. Feng, C. Lai, M. Kelly and N. C. Kar, "Dual Three-Phase PMSM Torque Modeling and Maximum Torque per Peak Current Control Through Optimized Harmonic Current Injection," in IEEE Transactions on Industrial Electronics, vol. 66, no. 5, pp. 3356-3368, May 2019, doi: 10.1109/TIE.2018.2854550.

[56] Y. Hu, Z. Q. Zhu and M. Odavic, "Torque Capability Enhancement of Dual Three-Phase PMSM Drive With Fifth and Seventh Current Harmonics Injection," in IEEE Transactions on Industry Applications, vol. 53, no. 5, pp. 4526-4535, Sept.-Oct. 2017, doi: 10.1109/TIA.2017.2707330.

[57] W. Wang, J. Zhang, M. Cheng and S. Li, "Fault-Tolerant Control of Dual Three-Phase Permanent-Magnet Synchronous Machine Drives Under Open-Phase Faults," in IEEE Transactions on Power Electronics, vol. 32, no. 3, pp. 2052-2063, March 2017.

[58] G. Feng, C. Lai, W. Li, J. Tjong and N. C. Kar, "Open-Phase Fault Modeling and Optimized Fault-Tolerant Control of Dual Three-Phase Permanent Magnet Synchronous Machines," in IEEE Transactions on Power Electronics, vol. 34, no. 11, pp. 11116-11127, Nov. 2019.

[59] J. Karttunen, S. Kallio, P. Peltoniemi, P. Silventoinen and O. Pyrhönen, "Decoupled Vector Control Scheme for Dual Three-Phase Permanent Magnet Synchronous Machines," in IEEE Transactions on Industrial Electronics, vol. 61, no. 5, pp. 2185-2196, May 2014.

[60] C. Zhou, G. Yang and J. Su, "PWM Strategy With Minimum Harmonic Distortion for Dual Three-Phase Permanent-Magnet Synchronous Motor Drives

Operating in the Overmodulation Region," in IEEE Transactions on Power Electronics, vol. 31, no. 2, pp. 1367-1380, Feb. 2016.

[61] IEC 60317-0-2 Specifications for particular types of winding wires - Part 0-2: General requirements - Enamelled rectangular copper wireIECwebstore, 10 2013, [online] Available: https://www.webstore.iec.ch/publication/1347.

[62] Hu Jianhui, Zou Jibin and Liang Weiyan, "Finite element calculation of the saturation DQ-axes inductance for a direct drive PM synchronous motor considering cross-magnetization," The Fifth International Conference on Power Electronics and Drive Systems, 2003. PEDS 2003., 2003, pp. 677-681 Vol.1, doi: 10.1109/PEDS.2003.1282958.

[63] D. Shuto, Y. Takahashi and K. Fujiwara, "Frozen Permeability Method for Magnetic Field Analysis of Permanent Magnet Motors Considering Hysteretic Property," in IEEE Transactions on Magnetics, vol. 55, no. 6, pp. 1-4, June 2019, Art no. 8201304, doi: 10.1109/TMAG.2019.2896956.

[64] S. Moros, J. Kempkes and S. Tenner, "Numerical Calculation of End-Coil'S Leakage Inductance for Concentrated and Hairpin Windings," 2019 IEEE International Electric Machines & Drives Conference (IEMDC), 2019, pp. 1144-1150, doi: 10.1109/IEMDC.2019.8785365.

[65] M. Silberberger, D. P. Morisco, H. Rapp and A. Möckel, "Calculation of end-winding leakage inductance for hairpin winding high power density traction machines using the PEEC method," 2021 IEEE International Electric Machines & Drives Conference (IEMDC), 2021, pp. 1-7, doi: 10.1109/IEMDC47953.2021.9449550.

[66] C. Liu et al., "Experimental Investigation on Oil Spray Cooling With Hairpin Windings," in IEEE Transactions on Industrial Electronics, vol. 67, no. 9, pp. 7343-7353, Sept. 2020, doi: 10.1109/TIE.2019.2942563.

[67] M. Aoyama and J. Deng, "Visualization and quantitative evaluation of eddy current loss in bar-wound type permanent magnet synchronous motor for mild-hybrid vehicles," in CES Transactions on Electrical Machines and Systems, vol. 3, no. 3, pp. 269-278, Sept. 2019, doi: 10.30941/CESTEMS.2019.00035.

[68] H. Sano, T. Aasanuma, H. Katagiri, M. Miwa, K. Semba and T. Yamada, "Loss calculation of bar-wound high-power-density PMSMs with massively parallel processing," 2017 IEEE International Electric Machines and Drives Conference (IEMDC), 2017, pp. 1-6, doi: 10.1109/IEMDC.2017.8002252.

[69] N. K. Bajjuri and A. K. Jain, "Equivalent 3-Level PWM: An Improved Technique to Reduce Torque Ripple in DI-WRIM analyzed as DI-OWIM," in IEEE Transactions on Industrial Electronics, doi: 10.1109/TIE.2020.2972440.

[70] IEC 60071-2. (1996). Insulation co-ordination, Part 2: Application guide.

[71] Greenwood, A. (1991). Electrical transients in power systems. New York, NY: John Wiley.

[72] Chowdhuri, P. (2004). Electromagnetic transients in power systems (2nd ed.). New York, NY: Research Studies Press - John Wiley.

[73] M. J. Melfi, “Low-Voltage PWM inverter-fed motor insulation issues”, IEEE Transactions on Industry Applications, vol. 42, no. 1, pp. 128-133, 2006.

[74] J. L. Guardado and K. J. Cornick, “The effect of coil parameters on the distribution of steep-fronted surges in machine windings,” IEEE Transactions on Energy Conversion, vol. 7, no. 3, pp. 552-559, 1992.

[75] S. R. Chalise, S. Grzybowski, and C. D. Taylor, “Accelerated electrical degradation of machine winding insulation,” ed, 2009, pp. 1-6.

[76] Tilea and C. Munteanu, "Motor cable electric parameter effects on the overvoltage phenomenon in inverter driven motors," 2013 8TH INTERNATIONAL SYMPOSIUM ON ADVANCED TOPICS IN ELECTRICAL ENGINEERING (ATEE), Bucharest, 2013, pp. 1-6.

[77] F. Moreira, T. A. Lipo, G. Venkataramanan, S. Bernet, "High-frequency modeling for cable and induction motor over-voltage studies in long cable drives", IEEE Trans. Ind. Appl., vol. 38, no. 5, pp. 1297-1306, Sep./Oct. 2002.

[78] L. Wang, C. Ngai-Man Ho, F. Canales and J. Jatskevich, "High-Frequency Modeling of the Long-Cable-Fed Induction Motor Drive System Using TLM Approach for Predicting Overvoltage Transients," in IEEE Transactions on Power Electronics, vol. 25, no. 10, pp. 2653-2664, Oct. 2010.

[79] L. Arnedo and K. Venkatesan, "Pspice simulation for conducted EMI and overvoltage investigations in a PWM induction motor drive system," 2002 IEEE Workshop on Computers in Power Electronics, 2002. Proceedings., Mayaguez, Puerto Rico, USA, 2002, pp. 132-137.

[80] S. De Caro et al., "Motor Overvoltage Mitigation on SiC MOSFET Drives Exploiting an Open-End Winding Configuration," in IEEE Transactions on Power Electronics, vol. 34, no. 11, pp. 11128-11138, Nov. 2019.

[81] C. Petrarca, A. Maffucci, V. Tucci, and M. Vitelli, “Analysis of the voltage distribution in a motor stator winding subjected to steep-fronted surge voltages by means of a multiconductor lossy transmission line model,” IEEE Trans. Energy Convers., vol. 19, no. 1, pp. 7–17, Mar. 2004.

[82] A. Krings, G. Paulsson, F. Sahlén and B. Holmgren, "Experimental investigation of the voltage distribution in form wound windings of large AC machines due to fast transients," 2016 XXII International Conference on Electrical Machines (ICEM), Lausanne, 2016, pp. 1700-1706.

[83] Y. Xie, J. Zhang, F. Leonardi, A. R. Munoz, M. W. Degner and F. Liang, "Voltage Stress Modeling and Measurement for Random-Wound Windings Driven by Inverters," 2019 IEEE International Electric Machines & Drives Conference (IEMDC), San Diego, CA, USA, 2019, pp. 1917-1924.

[84] H. A. Toliyat, G. Suresh and A. Abur, "Estimation of voltage distribution on the inverter fed random wound induction motor windings supplied through feeder cable," in IEEE Transactions on Energy Conversion, vol. 14, no. 4, pp. 976-981, Dec. 1999.

[85] Y. Xie, J. Zhang, F. Leonardi, A. R. Munoz, F. Liang and M. W. Degner, "Modeling and Verification of Electrical Stress in Inverter-Driven Electric Machine Windings," 2018 IEEE Energy Conversion Congress and Exposition (ECCE), Portland, OR, 2018, pp. 5742-5749.

[86] M. T. Wright, S. J. Yang, and K. McLeay, “General theory of fast fronted interturn voltage distribution in electrical machine windings,” in Proc. Inst. Electr. Eng., 1983, pp. 257–264.

[87] G. Suresh, H. A. Toliyat, D. A. Rendusara and P. N. Enjeti, "Predicting the transient effects of PWM voltage waveform on the stator windings of random wound induction motors," in IEEE Transactions on Power Electronics, vol. 14, no. 1, pp. 23-30, Jan. 1999.

[88] V. Mihaila, S. Duchesne and D. Roger, "A simulation method to predict the turn-to-turn voltage spikes in a PWM fed motor winding," in IEEE Transactions on Dielectrics and Electrical Insulation, vol. 18, no. 5, pp. 1609-1615, October 2011.

[89] P. Bidan, T. Lebey, G. Montseny, C. Neacsu, and J. Saint-Michel, “Transient voltage distribution in inverter fed motor windings: Experimental study and modeling,” IEEE Trans. Power Electron., vol. 16, no. 1, pp. 92–100, Jan. 2001.

[90] J. M. MartÍnez-Tarifa, H. AmarÍs-Duarte and J. Sanz-Feito, "Frequency-Domain Model for Calculation of Voltage Distribution Through Random Wound Coils and Its Interaction With Stray Capacitances," in IEEE Transactions on Energy Conversion, vol. 23, no. 3, pp. 742-751, Sept. 2008.

[91] M. Lukic, P. Giangrande, A. Hebala, S. Nuzzo and M. Galea, "Review, Challenges, and Future Developments of Electric Taxiing Systems," in IEEE Transactions on Transportation Electrification, vol. 5, no. 4, pp. 1441-1457, Dec. 2019.

[92] P. Giangrande, V. Madonna, S. Nuzzo and M. Galea, "Moving Toward a Reliability-Oriented Design Approach of Low-Voltage Electrical Machines by Including Insulation Thermal Aging Considerations," in IEEE Transactions on Transportation Electrification, vol. 6, no. 1, pp. 16-27, March 2020, doi: 10.1109/TTE.2020.2971191.

[93] M. Pastura, S. Nuzzo, M. Kohler and D. Barater, "Dv/Dt Filtering Techniques for Electric Drives: Review and Challenges," IECON 2019 - 45th Annual Conference of the IEEE Industrial Electronics Society, Lisbon, Portugal, 2019, pp. 7088-7093.

[94] G. Skibinski, D. Leggate and R. Kerkman, "Cable characteristics and their influence on motor over-voltages," Proceedings of APEC 97 - Applied Power Electronics Conference, Atlanta, GA, USA, 1997, pp. 114-121 vol.1.

[95] G. Berardi, S. Nategh and N. Bianchi, "Inter-turn Voltage in Hairpin Winding of Traction Motors Fed by High-Switching Frequency Inverters," 2020 International Conference on Electrical Machines (ICEM), 2020, pp. 909-915, doi: 10.1109/ICEM49940.2020.9270727.

[96] E. Preci et al., "Modelling of Voltage Distribution within Hairpin Windings," IECON 2021 – 47th Annual Conference of the IEEE Industrial Electronics Society, 2021, pp. 1-6, doi: 10.1109/IECON48115.2021.9589507.

[97] B. Kelly, J. Zhang and L. Chen, "Bar-Wound Machine Voltage Stress: a Method for 2D FE Modeling and Testing," 2021 IEEE Applied Power Electronics Conference and Exposition (APEC), 2021, pp. 1688-1693, doi: 10.1109/APEC42165.2021.9487103.

[98] X. Ju et al., "Voltage Stress Calculation and Measurement for Hairpin Winding of EV Traction Machines Driven by SiC MOSFET," in IEEE Transactions on Industrial Electronics, doi: 10.1109/TIE.2021.3116577.

[99] M. Pastura et al., "Partial Discharges in Electrical Machines for the More Electric Aircraft—Part I: A Comprehensive Modeling Tool for the Characterization of Electric Drives Based on Fast Switching Semiconductors," in IEEE Access, vol. 9, pp. 27109-27121, 2021, doi: 10.1109/ACCESS.2021.3058083.

[100] A. Rumi, L. Lusuardi, A. Cavallini, M. Pastura, D. Barater and S. Nuzzo, "Partial Discharges in Electrical Machines for the More Electrical Aircraft. Part III: Preventing Partial Discharges," in IEEE Access, vol. 9, pp. 30113-30123, 2021, doi: 10.1109/ACCESS.2021.3058090.

[101] A. Rumi, J. G. Marinelli, M. Pastura, D. Barater and A. Cavallini, "Insights into the Definition of Converter Surge Rise Time and its Influence on Turn/Turn Electrical Stress," 2021 IEEE Workshop on Electrical Machines Design, Control and Diagnosis (WEMDCD), 2021, pp. 272-276, doi: 10.1109/WEMDCD51469.2021.9425648.

[102] M. Pastura, D. Barater, S. Nuzzo and G. Franceschini, "Multi Three-Phase Hairpin Windings for High-Speed Electrical Machine: Possible Implementations," 2021 IEEE Workshop on Electrical Machines Design, Control and Diagnosis (WEMDCD), 2021, pp. 113-118, doi: 10.1109/WEMDCD51469.2021.9425640.

[103] M. Pastura, S. Nuzzo, G. Franceschini, G. Sala and D. Barater, "Sensitivity Analysis on the Voltage Distribution within Windings of Electrical Machines fed by Wide Band Gap Converters," 2020 International Conference on Electrical Machines (ICEM), 2020, pp. 1594-1600, doi: 10.1109/ICEM49940.2020.9270958.

[104] M. Pastura, D. Barater, S. Nuzzo and G. Franceschini, "Investigation of Resistivity Impact on AC Losses in Hairpin Conductors," IECON 2021 – 47th Annual Conference of the IEEE Industrial Electronics Society, 2021, pp. 1-6, doi: 10.1109/IECON48115.2021.9589047.

[105] M. Pastura, S. Nuzzo, D. Barater and G. Franceschini, "Analysis of Voltage Distribution and Connections within a High-Frequency Hairpin Winding Model," 2022 International Conference on Electrical Machines (ICEM), 2022, pp. 1642-1647, doi: 10.1109/ICEM51905.2022.9910681.

[106] M. Pastura, R. Notari, S. Nuzzo, D. Barater and G. Franceschini, "On the AC Losses in the End Conductors of Hairpin Windings," 2022 International Conference on Electrical Machines (ICEM), 2022, pp. 1150-1155, doi: 10.1109/ICEM51905.2022.9910862.

[107] R. Notari, M. Pastura, S. Nuzzo, D. Barater, G. Franceschini and C. Gerada, "AC losses reduction in Hairpin Windings produced via Additive Manufacturing," 2022 International Conference on Electrical Machines (ICEM), 2022, pp. 1144-1149, doi: 10.1109/ICEM51905.2022.9910620.